NTNU – Trondheim
Norwegian University of
Science and Technology

The Influence of Alternating Current on the Polarization Behavior of Stainless Steels

Catalina H. Musinoi Hagen

Declaration

I declare that the work described in this Masters' thesis has been performed independently and in accordance with the rules and regulations for examination at the Norwegian University of Science and Technology (NTNU).

Catalina H. Musinoi Hagen

Trondheim, June 12th 2013

Abstract

In later years direct electrical heating (DEH) based on the use of alternating current (AC) has replaced traditional chemical based methods for hydrate formation control in subsea flow lines. The problem with the AC-method is the increased risk of corrosion. A number of publications have been presented on the effect of AC on carbon steel since the early 1900s and there is a general understanding that higher alternating currents lead to higher risk of AC corrosion. However the mechanism is still not completely understood and besides - little is known about the AC-induced corrosion on stainless steels.

The purpose of this study is to provide accurate and thorough understanding of the mechanism and severity of applied AC on steels in general and stainless steels in particular. The cathodic polarization behavior of 316L stainless steel has been studied and compared with the polarization behavior of X65 carbon steel, at the direct current (DC) potentials -800 mV and -1050 mV (SCE) for a range of applied AC current densities - from 0 to 1000 A/m^2 . An investigation of the passivity of stainless steels with and without AC was carried out on 25Cr under open circuit conditions and under anodic bias. A total of 55 experiments were performed in 3.5 wt% sodium chloride (NaCl) for this study. The experiments were conducted at 25 ^{o}C with a stagnant working electrode and lasted 96 hours at the most. The current responses were recorded. Weight losses were measured. Surface morphologies were studied both visually, with Scanning Electron Microscopy (SEM) and Energy-dispersive spectroscopy (EDS).

Cathodic current densities for 316L were found to increase with one order of magnitude at -800 mV and two orders of magnitude at -1050 mV when AC was increased from 0 to 1000 A/m^2. The highest cathodic current density, $3.35*10^{-3}$ A/cm^2, was found for 316L at -1050 mV and 1000 A/m^2 AC. The highest corrosion rate (CR) for 316L - 0.113 mm/y - was measured at -800 mV and 1000 A/m^{2}AC. Cathodic current densities for X65 were found to be of same magnitude at -800 mV, but increased with one order of magnitude at -1050 mV when AC was increased from 0 to700 A/m^2. The highest cathodic current density for X65 was 2.18 $*10^{-3}$ A/cm^2 at -1050 mV and 700 A/m^2 AC. The highest CR for X65, 0.205 mm/y and 0.236 mm/y, were measured when 500 A/m^2 AC was applied at -800 mV and -1050 mV respectively. When AC densities higher than 100 A/m^2 were applied on 25Cr, hydrogen evolution was found to control the corrosion kinetics and the passive region disappeared.

The results indicate a significant acceleration of cathodic kinetics with applied AC. Weight loss measurements indicate also an increase in the corrosion rate with applied AC. However, the cathodic reaction rates were much higher than the anodic reaction rates at the applied DC potentials. The results implicate that the presence of AC decreases the effectiveness of cathodic protection systems. A possible model for the AC mechanism has been proposed.

Sammendrag (NO)

Det siste tiår er det blitt mer og mer utbredt å ta i bruk elektrisk oppvarming – *direct electrical heating* (DEH) for å unngå hydratutfelling og voksdannelse i subsea rør med hydrokarbonblandinger. Det er imidlertid identifisert en risiko for økt korrosjon med AC-strøm til stede, som DEH-systemet bygger på. En rekke publikasjoner som tar for seg effekten av AC på karbonstål er blitt publisert siden tidlig 1900-tall og det hersker en generell forståelse for at høyere nivåer av vekselstrøm medfører høyere risiko for AC-korrosjon. Men mekanismene er fortsatt ikke forstått og dessuten - lite er kjent om AC-indusert korrosjon på rustfritt stål.

Hovedanliggendet til denne studien er å bidra til økt innsikt i den AC-induserte korrosjonsmekanismen på stål generelt og rustfritt stål spesielt. De katodiske polarisasjonsegenskapene til 316L rustfritt stål er blitt studert ved potensialene -800 mV og -1050 mV (SCE) og sammenlignet med de katodiske polarisasjonsegenskapene til X65 karbonstål ved samme potensial, for en rekke påtrykte AC strømtettheter fra 0 til 1000 A/m^2. En undersøkelse av passiviteten til rustfritt stål med og uten påtrykt AC ble utført på 25Cr ved åpen krets forhold og under anodisk bias. Totalt ble 55 eksperimenter utført i 3,5 vekt% natriumklorid (NaCl) i forbindelse med denne studien. Forsøkene ble utført ved 25 ^{o}C med stagnant arbeidselektrode og varte i 96 timer på det meste. Strømresponsen ble overvåket. Vekttap ble målt. Prøvene ble undersøkt for korrosjonsskader både visuelt, i elektronmikroskop (SEM) og ved energidispersiv røntgenspektroskopi (EDS).

De katodiske strømtetthetene på 316L ble funnet å øke med én størrelsesorden ved -800 mV og to størrelsesordener ved -1050 mV når AC ble økt fra 0 til 1000 A/m^2. Den høyeste katodiske strømtettheten, 3,35*10^{-3} A/cm^2 ble funnet på 316L ved -1050 mV and 1000 A/m^2 AC. Den høyeste korrosjonshastigheten til 316L – 0,113 mm/y – ble målt ved -800 mV og 1000 A/m^{2}AC. De katodiske strømtetthetene på X65 ble funnet å være av samme størrelsesorden ved -800 mV og å øke med én størrelsesorden ved -1050 mV når AC ble økt fra 0 til 700 A/m^2. Den høyeste katodiske strømtettheten på X65, 2,18 *10^{-2} A/cm^2 ble funnet ved -1050 mV og 700 A/m^2 AC. De høyeste korrosjonshastighetene til X65 – 0,205 mm/y og 0,236 mm/y – ble målt ved henholdsvis -800 mV og -1050 mV og 500 A/m^2 AC. Når AC strømtettheter høyere enn 100 A/m^2 ble påtrykt på 25Cr, ble korrosjonskinetikken funnet å kontrolleres av hydrogenutvikling. Samtidig forsvant det passive området.

Resultatene viser en betydelig akselerasjon av den katodiske kinetikken med påtrykt AC. Vekttapsmålinger indikerer også en økning i korrosjonshastigheten med økning i påtrykt AC. De katodiske reaksjonshastighetene er imidlertid mye høyere enn de anodiske ved DC-potensialene testet. Resultatene impliserer at den påtrykte AC reduserer den beskyttende effekten ved katodisk beskyttelse. Strømbehovet øker med økt AC tetthet. En mulig modell for AC-mekanismen er foreslått.

Preface

This thesis finalizes the Master's degree at the Department of Materials Science and Engineering at the Norwegian University of Science and Technology (NTNU) in Trondheim, Norway. The study was carried out in cooperation with NEXANS NORWAY AS. The thesis is a continuation of the work related to the course TMT4500, *Materials Technology, Specialization Project,* from December 2012.

The author would like to thank:
Supervisor **Kemal Nisancioglu** (K2, NTNU), staff engineer **Kjell Røkke** (K2, NTNU) and co-supervisor **Magnus Hurlen Larsen** (Nexans, Halden) for guidance and helpful assistance throughout the project.

In addition the author would also like to thank her husband **Audun Hoem Musinoi Hagen** for patience, love and good food throughout these years at NTNU.

The years at NTNU have been hard and at times frustrating but above all inspiring, funny and magic! Countless coffee brakes and words of wisdom shared during parties, lunches or in the offices of Faculty staff – contributed in this respect to the magic. Thank you all!

Catalina H. Musinoi Hagen

Contents

List of Figures

List of Tables

Glossary

	Abbreviations
AC	Alternating current
AV	Alternating voltage
CR	Corrosion rates
CS	Carbon steel
CE	Counter electrode
CP	Cathodic protection
DC	Direct current
DEH	Direct electrical heating
EDS	Energy Dispersive X-ray Spectroscopy
FESEM	Field emission scanning electron microscopy
GDOES	Glow discharge optical emission spectroscopy
MEG	Monoethylene glycol
RT	Room temperature
RMS	Root mean square
SCE	Standard calomel electrode
SDSS	Super duplex stainless steel
SMSS	Supermartensitic stainless steel
SG	Standard grade
SS	Stainless steel
WE	Working electrode
XPS	X-ray photo electron spectroscopy

	Parameters	
Symbol	**Description**	**SI unit**
E_{OC}	Open circuit potential	[V]
E_{corr}	Corrosion potential	[V]
i_{AC}	Alternating current density	[A/m^2]
i_{DC}	Direct current density	[A/m^2]
i_{corr}	Corrosion current density	[A/m^2]
i_{lim}	Limiting current density	[A/m^2]

1 Introduction

The role of alternating current (AC) in corrosion of steels has been debated since early 1900s as AC has been found to cause corrosion on buried metallic structures due to AC interference from high-voltage transmission lines. A number of reports have investigated the mechanism of AC induced corrosion on carbon steel due to such AC stray currents.

This thesis will however focus on the AC corrosion of stainless steel as a result of the AC being applied directly to steel. Applying AC directly to steel has the recent years developed as an attractive method - called direct electrical heating (DEH) - for hydrate and wax control for multiphase flows either by itself or as part of other hydrate control method. Unfortunately it has been generally recognized that pipelines can suffer corrosion despite satisfying the conventional cathodic protection (CP) criteria and material losses have been documented above $\approx$ 70 A/m^2 AC despite high DC protection currents [1], see Figure 1. The principle behind the CP system is to set up a galvanic current to protect the structure by sacrificing a less noble material, i.e. sacrificial anodes, or by supplying the current with a rectifier. To prevent corrosion a protection criteria is designed which mandates a protection potential of - 800 – 1050 mV [2] V relative to the saturated calomel electrode (SCE)/seawater reference electrode. However, due to the AC corrosion risk is has therefore been required to develop new CP criteria that can appropriately assess the AC corrosion risk. To accomplish that, the AC corrosion mechanism should first be understood.
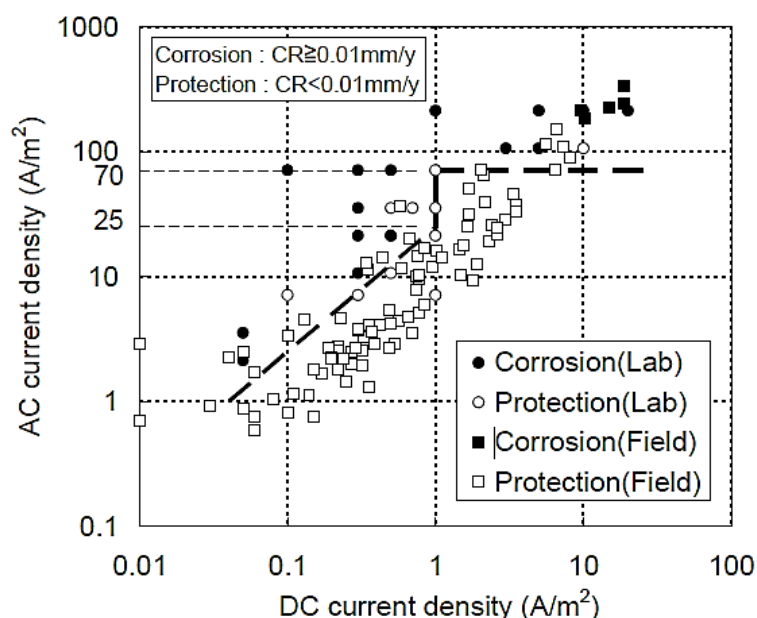
Figure 1: The effect of DC and AC current densities on the corrosion rate of carbon steel, when testing at 50Hz AC. Material losses have been documented above $\approx$ 70 A/m2 AC despite high DC protection currents [1].

This chapter will provide in-depth information about how AC is used in the direct electrical heating system and outline the scope of the study and the methodology it is grounded on, as well as the overriding and underlying objectives of the study. The thesis outline can be found in the last section of the chapter.

1.1 Background

With oil and gas in scarce supply, the offshore industry has been forced to operate in deeper water and more aggressive, demanding subsea environments. Offshore oil and gas installations typically have multiple wells tied back through subsea pipelines to a single platform. The untreated well flow composed of a mixture of oil, gas and water, holds an elevated temperature when leaving the wellhead. During long facility shut downs or under other unplanned maintenance events, temperature in pipes decreases heavily and if not kept above the hydrate equilibrium temperature (HET) hydrates will form impeding the flow and the consequences may be a blocking of the well stream transport.

For years the chosen method for conservation of fluid flow was to inject chemicals (MEG) inhibiting the hydrate formation by lowering the formation temperature. In later years direct electrical heating has started to replace MEG, as it provides an environmental friendly solution. Especially for deep-water fields electrical heating of pipelines is attractive for achieving reliable operation of transport pipelines. The temperature drop for these pipe lines, requires DEH on a continuous basis.

The DEH method is based on the fact that an alternating current will generate resistive heat in a metallic conductor. Such heating of the steel pipe requires AC current to be transferred down to the seabed through a wire and to be transferred to the steel pipe by use of a designated system of anodes, see Figure 2.
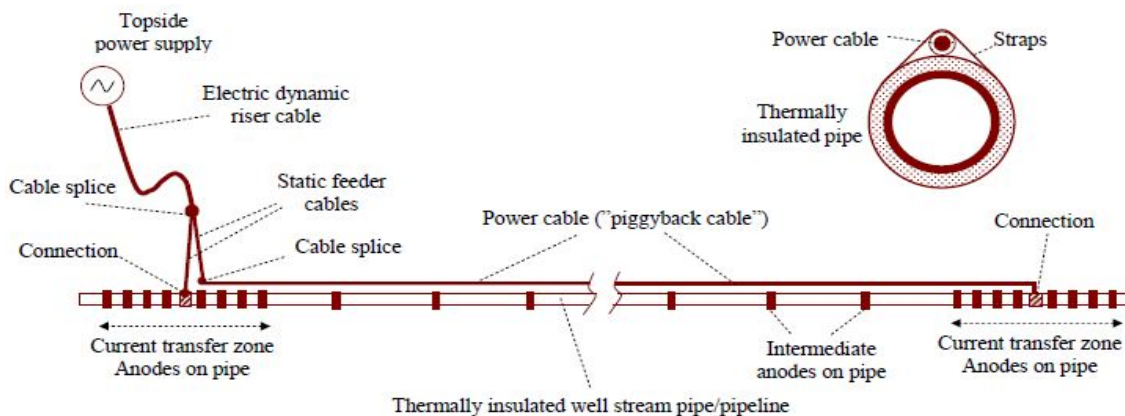
Figure 2: Illustrative graphics provided by SINTEF describing the concept of DEH. The pipeline is heated by an AC current entering the pipe and generating heat due to metallic resistivity.

The AC is collected at the other end of the line through another transfer zone of anodes. The heating system is thus galvanically connected to the surrounding sea water through sacrificial anodes, and the sea water acts as an electric conductor in parallel with the pipe. Electric current will therefore be transferred from the anodes and any eventual defect in the thermal insulation, to the sea. The smaller the defects are the higher will the AC current densities be especially near the transfer zones where AC current is entering and leaving. The number of anodes in the transfer zones must therefore be high enough both to overcome the oxidation

currents at local defects where AC is converted to DC - thus contributing to increased corrosion rates **and** to minimize the AC current densities on the anodes - thus avoiding corrosion of the anodes.

1.2   Scope and methodology

The scope of this study is to provide accurate and thorough understanding of the mechanism and severity of applied AC on stainless steels.

The methodology chosen for this task is to investigate the behavior of these metals under cathodic and anodic polarization, when increasing AC densities are applied. Results from cathodic potentiostatic polarization tests performed on 316L stainless steel are to be compared with similar on X65 carbon steel. Anodic polarization tests will be performed on 25Cr super duplex stainless steel for an investigation of the passivity of stainless steels with and without AC. In addition the report investigates the changes in stainless steels' susceptibility to localized corrosion and passivation with and without AC with a scanning electron microscope (SEM) and by energy-dispersive spectroscopy (EDS).

This report limits its analysis to experiments performed with a stagnant working electrode in 3.5 wt% sodium chloride (NaCl) over a maximal immersion time of 96 hours per sample. The AC signal delivered by a VariAC was applied as sinus waves at 50 Hz monitored and tuned manually by multimeters. The effectiveness of the AC/DC filters used in the circuit was not checked but assumed to be negligible according to previous reports [3, 4].

1.3   Objectives

The DEH technology is currently in use on several oilfields: Skuld, Huldra, Åsgard B, Kristin, Norne and on Tyrihans from 2007 onwards – all fields belonging to Statoil. Now BP has installed DEH on the Skarv field in the North Sea and plans to use the method on the Shah "Deniz stage 2" project in the Caspian Sea.

The objective of this thesis is to provide knowledge about the corrosion mechanisms under the influence of AC – knowledge that can be used in minimizing the risk for AC-induced corrosion. Investigating the corrosion mechanism on stainless steel under the influence of AC may provide an insight into the mechanism of AC corrosion.

Previous studies have investigated the risk of AC corrosion mainly for carbon steel and it has been shown that there is a correlation between the magnitude of AC current density on the exposed steel and the risk of AC corrosion. A clear decrease in the corrosion potential and increased corrosion rates have also been reported for carbon steel when the applied AC has been increased. In addition, studies have also shown altered electrochemical behavior for sacrificial anodes. British Petroleum (BP) has decided to operate at 100 A/m^2 AC in order to minimize the risk for AC-induced corrosion. Statoil has operated at 250 A/m^2 AC. The threshold value where the AC current density is seen to pose an unacceptable risk of corrosion

is still debated. Corrosion prevention is of huge importance in order to prolong the life of pipelines and prevent leakage of oil and gas to the sea. Understanding the thermodynamics and kinetics of steel when AC is applied, is hence important both from an economical point of view but also on an environmental level.

1.4   Thesis outline

This thesis consists of seven chapters plus references and appendices.

Chapter 1   presents the background, objectives, scope and methodology of the thesis.

Chapter 2   provides a literature review on the process of steel corrosion

Chapter 3 describes the composition of the solutions and materials used, sample size and shape, sample preparation and testing procedure

Chapter 4   presents test results

Chapter 5   presents detailed discussion of these results

Chapter 6   presents the conclusions of the study

Chapter 7   sketches a the path for further work

2   Literature review

A considerable amount of literature exists on the AC corrosion mechanism and different theories have been proposed to explain the subject. A thorough literature review is therefore seen as necessary in order to encompass the different aspects. In the following chapter important theories will be outlined considering the DC corrosion reaction and mechanism, followed by a literature review on studies regarding the AC mechanism. To begin with the equivalent circuit representing the corrosion reaction will be presented.

2.1   The equivalent circuit

Any electrochemical cell can be represented in terms of an equivalent electrical circuit that comprises a combination of resistances, capacitances or inductances. The electrode surface, if not inert, will interact with the charges coming near it and charge transfer will occur at the interface. When steady state is achieved meaning a steady state current results in a steady state potential drop across the interface, the resistance corresponding to this charge transfer process will be the sum of the charge transfer resistance, denoted as R_{CT} in the literature and the mass transfer resistance R_M. In sum, these two resistances give what is called the faradaic polarization resistance, R_P. The interface between the electrode surface and the solution will behave as a capacitor, where the two layers of charge that will build up are referred to as the double layer. The double layer capacitance is denoted C_{Dl}. In addition also a resistance regarding the electrolyte will be present, R_S - the ohmic electrolyte resistance.

The current response in an electrochemical system is thus dependent on the characteristics of the system under study[5], see Figure 3 for the equivalent circuit representing the abovementioned system.
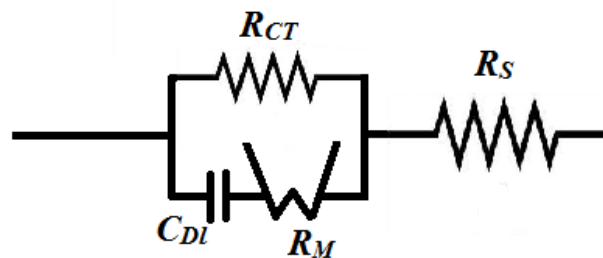
Figure 3: The circuit of an electrode that interacts electrochemically with the species coming close to the surface and with the electrolytic solution, but posing a resistance against charge transfer due to diffusion of reacting species. Figure adapted from literature.

According to this model the current in an electrochemical cell is in general seen to be equal to contributions from both faradaic processes and also due to the charging of the double layer:

$$i = i_f + i_c$$

(1)

The current response related to the double layer charging is given by:

$$i_C = -C_{dl} * \frac{dV}{dt} = 2\pi f \Delta V C_{dl} \sin(2\pi ft) \qquad (2)$$

Where:

C_{dl} = double layer capacitance [F/cm^2]

f = frequency [Hz]

ΔV = input signal [V]

The current density response due to faradaic processes is given by:

$$i_f = nFk_a \exp(b_a V) - nFk_c \exp(-b_c V) \qquad (3)$$

Where:

k = heterogeneous rate constant [m/s]

n = number of electrons involved in the electrode reaction

F = Faraday constant, 96485 [C/mol]

2.2   The DC-corrosion mechanism

For electrochemical systems where the anodic and cathodic reactions represent forward and backward reaction rates of the same reaction, a zero current can be obtained under the condition of reaction equilibrium. The potential at which the currents contributed by the anodic and the cathodic reactions give a zero current, is termed *the equilibrium potential*. This is a thermodynamically value.

Such equilibrium potentials can for corrosion reactions be analyzed by the use of Pourbaix diagrams. The diagram maps on a pH-potential plot areas where different corrosion products of a metal are thermodynamically stable. In other words, from a Pourbaix diagram it can be determined whether a corrosion process is favored or not by studying the metal's stability in means of equilibrium potentials and pH.

However, corrosion processes are a sum of several different reactions that happen on the same metal. Then, the zero current condition arises through a balancing of different reactions and equilibrium is not achieved because the net rate for each reaction is not equal to zero. The potential at which the current for multiple electrochemical reactions is zero, is termed the *mixed potential*, or in case for metal dissolution, *the corrosion potential, E_{corr}* [5].

2.2.1   Uniform corrosion

The corrosion process consists of an anodic and a cathodic reaction. The anodic dissolution of iron in aqueous solution has been the subject of extensive study. Although a number of mechanisms have been proposed, it is generally agreed that the initial stages of oxidation proceed through an adsorbed FeOH$_{ADS}$ intermediate, followed by a second electron transfer to produce a surface of Fe(II)-species [6]. Assuming that OH$^-$ is the active adsorption species in the anodic reaction, the following element reactions (4), (5), (6), (7) are possible[7]:

$$\text{Fe} + \text{OH}^- = \text{FeOH}_{\text{ADS}} + \text{e}^- \tag{4}$$
$$\text{Fe(OH)}_{\text{ADS}} = \text{Fe(OH}^+) + \text{e}^- \tag{5}$$
$$\text{Fe(OH}^+) = \text{Fe}^{2+} + \text{OH}^- \tag{6}$$
$$\text{Fe(OH)}_{\text{ADS}} + \text{OH}^- = \text{Fe(OH)}_{2 +} \text{e}^- \tag{7}$$

When corrosion happens in Cl^- dominated solutions, OH^-- ions and Cl^- - ions will compete over the free active sites such that $Fe(OH)^+$ is more likely to transform into a ferrous-chloro species rather than precipitate as $Fe(OH)_2$. Under anaerobic conditions the ferrous hydroxide $Fe(OH)_2$ may in addition be oxidized by the protons of water to form the thermodynamically more stable magnetite and produce molecular hydrogen, a process described[8] by the Schikorr reaction :

$$3\,\text{Fe(OH)}_2 = \text{Fe}_3\text{O}_4 + \text{H}_2 + 2\,\text{H}_2\text{O} \tag{8}$$
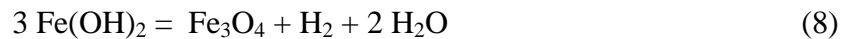
In alkaline solutions Fe_3O_4 is thus expected to exist. If corrosion happens in an aerated solution containing Cl^- ions, (9) and (10) are possible at sufficient anodic potentials:

$$2\text{OH}^- = \tfrac{1}{2}\,\text{O}_2 + \text{H}_2\text{O} + 2\text{e}^- \tag{9}$$
$$2\text{Cl}^- = \text{Cl}_2\,(\text{g}) + 2\text{e}^- \tag{10}$$

The reduction reactions that pick up electrons from these oxidation reactions are given by eq. (11), (12) and (13), where (11) is just the reverse of (9):

$$\tfrac{1}{2}\,\text{O}_2 + \text{H}_2\text{O} + 2\text{e}^- = 2\text{OH}^- \tag{11}$$
$$2\text{H}_2\text{O} + 2\text{e}^- = 2\text{OH}^- + \text{H}_2\,(\text{g}) \tag{12}$$
$$2\text{H}^+ + 2\text{e}^- = \text{H}_2\,(\text{g}) \tag{13}$$
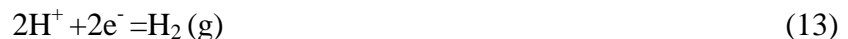
In neutral and alkaline environment the oxygen reduction eq. (11) will at an electrode surface cause the pH to reach 10 or 11, even when the pH in the bulk is 7. At the same time the oxygen is decreasing in concentration on a local level, where the diffusion rate of O_2 will limit the reaction rate. If the current is increased, the hydrogen evolution will take over as the dominating reaction.

The evolution of hydrogen is found to proceed through three steps [9]: (i) electrochemical reduction of water (in neutral or alkaline solution) or hydrogen ions (in acidic solution), (ii) electrochemical recombination of hydrogen atoms, and/or (iii) chemical desorption of hydrogen atoms. The overall equation is shown in eq. (12) for an alkaline medium while eq.(13) happens in acidic medium.

To investigate the kinetics of activation controlled corrosion reactions, the Butler-Volmer is commonly used to describe the influence of potential on the current density, eq.(14)

$$i = i_0 \left\{ \exp\left(\frac{(1-\alpha)nF}{RT} \eta_s \right) - \exp\left(-\frac{\alpha nF}{RT} \eta_s \right) \right\} \tag{14}$$

Where :

R = gas constant [J/Kmol]

T = temperature [K]

n = number of charges transferred ($\equiv$ valency)

F = Faraday constant [C/mol]

α = transfer coefficient

i_o = exchange current density [A/m^2]

η_s = the surface potential [V]

The surface overpotential η_s represents the departure from an equilibrium potential, such that at $\eta_s = 0$ the total current $I_T = 0$ and the cathodic current is equal to the anodic current. This means that at the corrosion potential (E_{corr}), the sum of the anodic and cathodic currents is equal to zero and $i_0 = i_a = -i_c$.

When studying a narrow range of potential near the zero current potential, a Taylor series expansion of the exponential terms in eq.(1) leads to the polarization resistance (R_P) :

$$i = \frac{i_0 * nF(E - E_{eq.})}{RT} \tag{15}$$

Where R_P is given by:

$$R_P = \frac{RT}{nFi_0(\alpha_a + \alpha_c)} \tag{16}$$

When studying the high overpotential region - very positive potentials and very negative potentials - a simplification of Butler-Volmer leads to the Tafel equations, where Tafel slopes are denoted b_a and b_c [V/dec.] :

$$\begin{aligned} i &= i_0 \exp(b_a \eta_s) \\ i &= -i_0 \exp(-b_c \eta_s) \end{aligned} \tag{17}$$

It is to be noted that the Butler-Volmer equation is based on the following assumptions:

a) the electrode reaction is controlled by electrical charge transfer.

b) the solution interface is homogeneous such that local equilibrium is present, i.e. current and potential distribution is uniform and hence corrosion is of uniform type.

2.2.2 Localized corrosion

In this chapter a review is presented of some essential subjects on the passivation progress, the properties of the passive films and the breakdown processes leading to further localized corrosion.

2.2.2.1 The passivation of metals

From literature two definitions of passivity have been identified [10] and the phenomenon of passivity is related to the formation of a condensed phase of continuous oxide layer on the metal surface which takes place during an exposure of the bare metal to an oxidizing environment.

1. A metal is passive if it substantially resists corrosion in a given environment resulting from marked anodic polarization.
2. A metal is passive if it substantially resists corrosion in a given environment despite a marked thermodynamic tendency to react.

Carbon steels passivate by the formation of iron oxides on the surface of metal, which thermodynamically is difficult or impossible at a pH below 8 but very easy between pH 10 and 12 [11]. At too high pH levels, the alkalization may actually lead to active corrosion at certain potentials, se the high pH-region depicted from pH>13 in Figure 4.
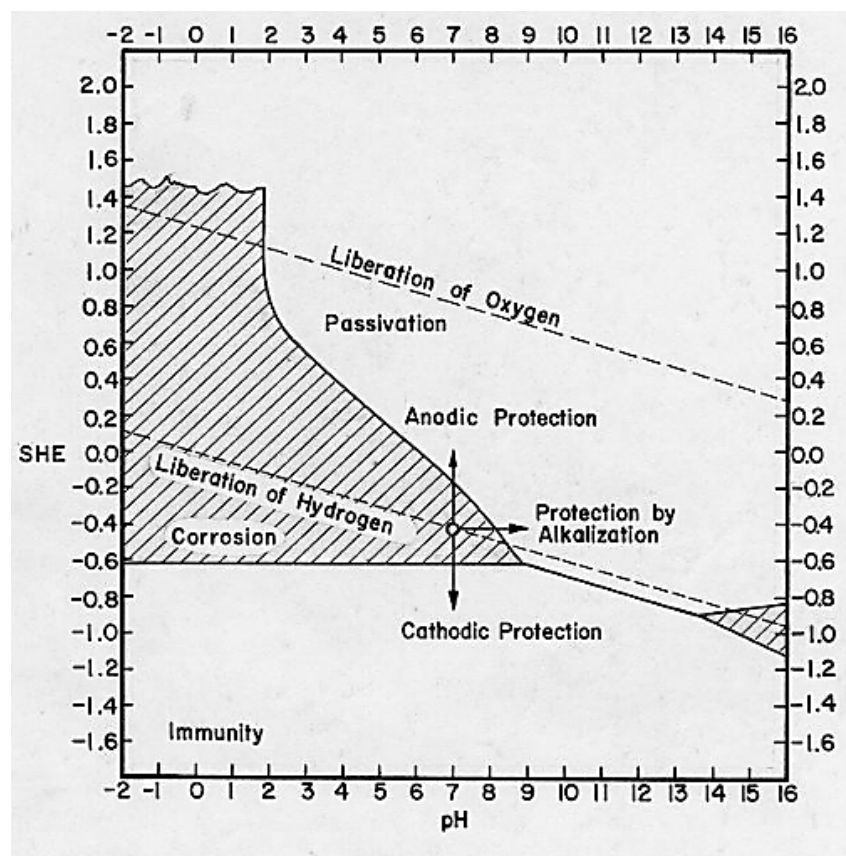
Figure 4: The Pourbaix diagram for iron at 25 °C where the active corrosion region of iron are indicated by the shaded areas. The passivation and immunity regions are also marked [12].

At high anodic potentials iron will passivate with a bilayer of Fe_3O_4 at its inner region covered by an outer layer of γ-Fe_2O_3 [13]. The passivity properties of oxides formed on carbon steel are inferior to those formed on stainless steels, as these oxides are among other not tightly bonded to the surface and will flake and fall off.

9

Numerous investigations have contributed to the present understanding on the passivation phenomenon of steels [10, 13-16] and it has been proposed that oxide films formed on stainless steels in neutral to alkaline solutions are composed of a chromium-rich inner region (3-4 atomic monolayers) close to the metallic substrate and an iron rich outer layer of iron oxides [17, 18]. The corrosion resistance of stainless steel is usually attributed to these tightly bonded films as they are seen to act as a barrier against aggressive diffusive ions and molecules.

Different growth models have been proposed to explain the growth of oxides on steels, but a review of such is seen to be outside the scope of this work.

2.2.2.2 The properties of passive films

Oxide films with controlled thickness can be grown during electrochemical oxidation of Fe. The thickness of passive films on steel is generally a few atomic layers thick and depends of the conditions the films are grown under. Different thicknesses will lead to different colors due to interference of light reflected at the oxide film/air and steel/oxide interfaces [19]. Not only colors but also corrosion properties of stainless steels are seen to depend directly on composition, structure and thickness of the passive films formed on their surfaces [13, 16, 17, 19-26].

From the literature it is found that passive films on stainless steels have several impeding properties against corrosion:

    a) increased thermodynamic stability [21, 27-29]
    b) decreased oxidation kinetics [9, 13, 17, 18, 20, 22, 30-32]

The thermodynamic stability the alloying elements provide when alloyed to steel, has been correlated to the content of chromium (Cr) and molybdenum (Mo). Especially Mo is indispensable for the improvement of pitting resistance. When added to austenitic and ferritic stainless steels at a concentration of a few percent, it was found to cause a significant shift in the breakdown (pitting) potential to more positive values [28, 29], while the addition of 5% Mo to 13, 18, and 25% Cr alloys were shown to produce over an order of magnitude decrease in the critical current density. The results were explained as a synergistic effect between Mo and Cr, where a higher addition of Cr lead to a substantial increase in pitting potentials when constant contents of Mo were present [29]. Cr is also seen to play a role in lowering the electronic conductivity, while Mo is seen to block the penetration of Cl^- [33].

A similar synergistic beneficial effect has also been found between Mo and nickel (Ni). A surface enrichment of a monolayer Ni on steel will increase the resistance by decreasing the kinetics for active dissolution [34]. In neutral solution, Ni is seen to buffer the local pH thus slowing down the acidification in the pit sites and hence hindering the pit propagation process [35]. The alloying elements Ni, Mo and Cr contribute to this passivation by either contributing in the film formation or stabilizing it. In alkaline media Fe is seen to be depleted,

Cr is oxidized and Ni is seen to be enriched. The passive film containing Fe-Cr is thus stabilized by the Ni enriched at the interface [36].

As can be seen from the Pourbaix diagram provided in Figure 5, a wide array of oxides may theoretically be formed on steel alloyed with chromium and molybdenum: Fe_2O_3, Cr_2O_3, $FeCr_2O_4$, Fe_3O_4 and FeO, MoO_2. In addition a variety of hydroxides may also be formed. The protective effect will thus differ with the specific type of layer and its chemical composition.
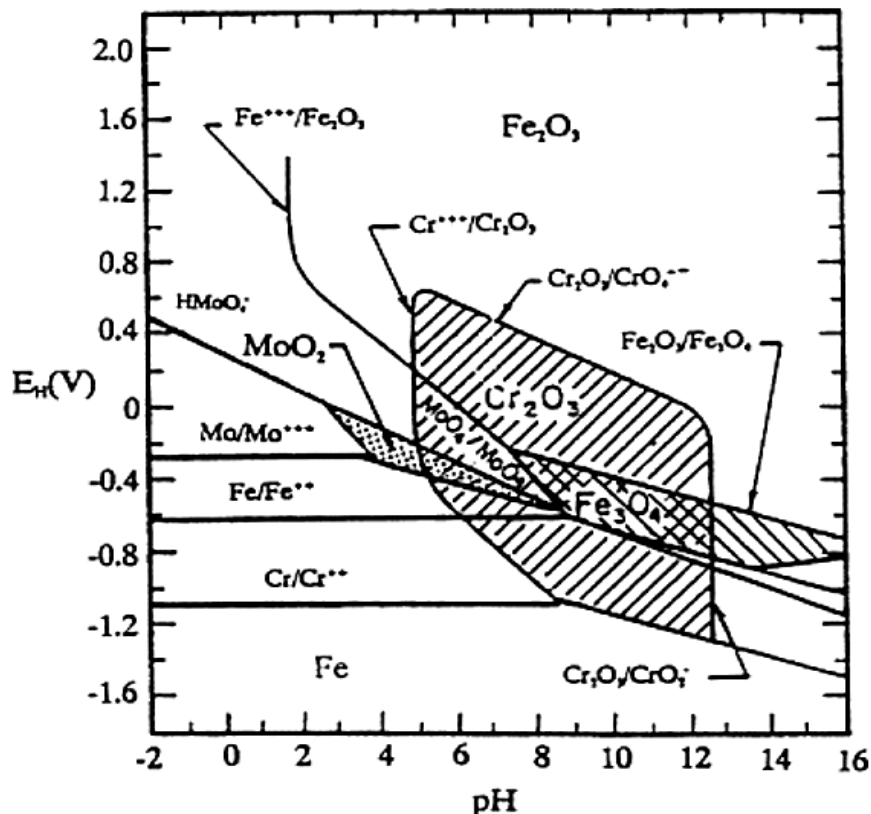
Figure 5: Superposition of Pourbaix diagrams for chromium, molybdenum and iron in water at 25 ^{o}C where the passive regions related to formation of oxides are indicated by the shaded areas [29].

The corrosion kinetics is controlled by the ionic and electric mobility through the passive layer. Ionic charge transport represents an important contribution to the electrochemical circuit and hence corrosion kinetics. The circuit consists of the flow of electrons in addition to the flow of ions through the electrolyte. Without current in form of moving ions through the liquid phase, it would not be possible to complete the circuit as ions moving around contribute to the overall current. With such films present, the mobility of ions from the metal surface to the electrolyte and vice versa is impeded and found to be proportional to the thickness of the formed oxide [17] for stainless steels.

Another contribution to the resistance of passive oxide films on stainless steels is explained in terms of the semiconductive properties of the films [13, 32], related to the alloying elements. In the case of passive carbon steel only the outer layer of γ-Fe_2O_3 grown at high anodic

potentials is seen to possess semiconducting, i.e. capacitive properties, while the Fe_3O_4 at its inner region is presumed to behave almost as a metallic conductor. Passive films formed on stainless steels have shown semiconducting properties related to both regions of the film: It has been proposed that the chromium-rich inner regions of oxides on stainless steel are of p-type character while the iron rich outer layers are of n-type [13].

It is been seen that the oxygen reduction reaction happens at different rates on bare and passivated surfaces, with the highest rate on the bare metal [37]. A limited access of O_2 to the metal surface suggest such that the electroreduction of O_2 requires the partial reduction of the oxides[38]. However the hydrogen reaction is contrary to this found to be enhanced [20]by the partially insulating film present, which will facilitate the transport of hydrogen under the effect of an electric field that builds up in the layer of film during polarization. The mobility is favored in the forward direction, i.e. degassing of oxidised iron will take place.

2.2.2.3 The breakdown of passive films

The mechanism of localized corrosion on stainless steel has been divided into three consecutive steps: initiation, metastable propagation and stable propagation of pits. The initiation step is caused by a local breakdown of the film.

Inhomogeneities preexisting on the electrode surface will in time lead to chemical and potential gradients, hence resulting in a local breakdown of the passive film. Such inhomogeneities can also develop [39] over an electrode surface due to an irregular chemical adsorption, selective dissolution and damages in the films caused by mechanical stresses. As well may non-uniformities in the environment – temperature gradients, turbulent flow and differential aeriation - cause a development of such inhomogeneous surface reactions. The breakdown of passive films at such susceptible sites on the metal surface is also dependent on other important features as the presence of aggressive ions, the potential exceeding a critical value and the induction time for the breakdown to occur.

When the mentioned factors are present, breakdown is in literature found to happen by several possible mechanisms [13]: either by a tunneling of aggressive anions towards the metal surface under a high electric field strength or by a breakdown initiated by an adsorption competition between hydroxyl ions and aggressive anions at the oxide-electrolyte surface. In addition also a mechanical breakdown of the film is possible.

It is believed that on stainless steels all forms for localized corrosion in chloride media are triggered by metastable pitting events, and deposits like rust from crevice corrosion is supposed to have a stabilizing effect on the pits. In sodium chloride (NaCl) solutions and in sea water pitting is found to have a strong correlation to crevice corrosion mechanisms [40]. In the presence of a layer of conventional rust as iron oxide, pitting has seen to increase in propagational speed. This is explained due to the low resistivity this rust layer is believed to have towards pits. The rust layer acts as a super-crevice. [41]. The initiation of pits in surface flaws, as well as the relation between pitting and crevice corrosion has been supported by several authors.

When pits are formed at these breakdown locations, the corrosion will proceed by several processes. One of the processes is the hydrolysis of metal ions, producing protons. In addition oxygen will be reduced and in time locally depleted. As oxygen levels will be high the electrode surface outside the pit, the formation of a concentration cell will transform the surface to a cathode and the pit into an anode. The pH inside the pit will now decrease due to hydrolysis of water, and a small fraction of the H$^+$ ions are found to be discharged in the pit, giving evolution of hydrogen gas by eq.(13). It is believed that the acidification within the crevices is accelerated by hydrolysis of chromic ions [42].

Meanwhile reaction rates will increase due to the migration of aggressive ions as Cl$^-$ into the pit due to requirements of electron neutrality. The pitting potential, being a measure of the steel's susceptibility to pitting, is in NaCl seen to decrease with the concentration of Cl$^-$ - ions [43].

On the surface outside the pit, the alkalization will proceed by the reduction of water, when mass transport limitations no longer allow reduction of oxygen. According to the Pourbaix diagram for iron, Figure 4, the alkalization may at high pH conditions result in the corrosion of carbon steel. Stainless steel will however be stabilized in the high pH-region by a monolayer thick enrichment of Ni on the surface, which thus will contribute in lowering the corrosion kinetics.

The limiting condition against an even more increased corrosion rate will be the formation of a salt layer at the bottom of the pit. The salt film will thus hinder the continuous anodic dissolution of the metal and corrosion rates slow down, see Figure 6. This is the *anodic limitation* of pitting. A *cathodic limitation* can also be reached when the formed hydrogen gas eventually leads to the formation of a gas carpet on the surface which leads to a high ohmic resistance.
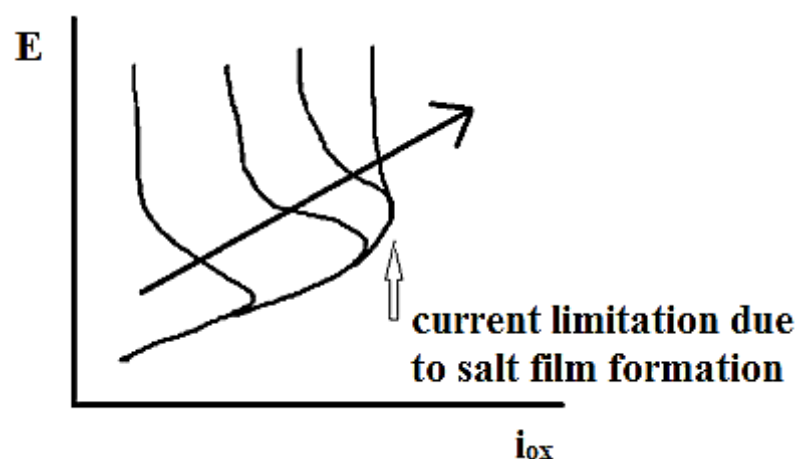
Figure 6: The anodic polarization curve for steel with an increase in [Cl$^-$] and a decrease in pH. Eventually there will be a current limitation due to a salt film formation. Figure adapted from [44]

It has been shown [13] that two types of pitting corrosion are possible configurationally: The etch-pitting which happens at low potentials in the active state and the polish-pitting which

happens when pit surfaces usually are covered with a salt layer at high potentials during the transpassive dissolution, see Figure 7.
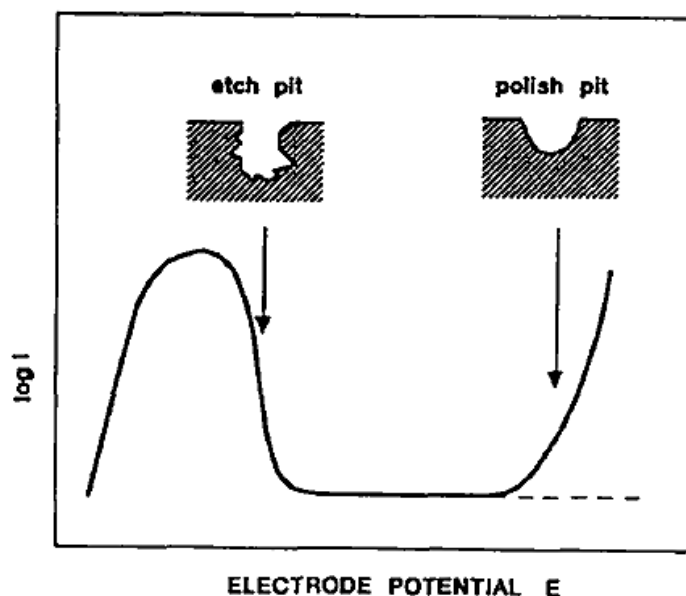
Figure 7: The two types of pitting identified to be the etch pitting at low potentials and the polish-pitting at high potentials where elctropolishing takes place on the pit surface [13].

These authors have shown that pitting on stainless steels starts from flaws in the oxide film and propagates by an ion transport mechanism. The pit initiation and growth are seen as stochastic, sporadic and random processes [45] where characteristic quantities as the pitting potential and the incubation time are observed to scatter. Carbon steels, which are not alloyed with neither Cr or Mo and will only form hydroxides or ferrous oxides, are seen to be less stable than stainless steels, but due to the process by which passive films brake down – they are also less prone to localized corrosion. Carbon steels corrode mainly uniformly in neutral saline solution, but pitting corrosion has also been observed especially when deposit layers are present on the steel surface [9]. As carbon steels are not alloyed with Ni either, alkalized corrosion may happen at high pH.

It is to be noted that localized corrosion on stainless steels may also come in the form of grain boundary corrosion which is related to the depletion of chromium around the grains. The depletion happens due to the formation of chromium-rich carbides around the grains usually at high temperature, $T>500\,^{o}C$. When exposed to an aggressive environment as seawater, the sensitization at high temperature will have its consequence: chrome is no longer available as a protection, hence grain boundaries are more prone to corrode [46].

2.3   The AC- corrosion mechanism

The effect of AC has been debated for many years and the literature cited below is clear on several points:

i.   AC increases corrosion rates on steels both with and without cathodic protection but the effects of AC on corrosion rates is only a small percentage of what would have been if a DC density of the same magnitude would be applied.

ii.   The AC effect on steels can however not be predicted by a simple AC+DC analysis

iii.   Corrosion potentials are affected and the same can be said about pitting potentials.

iv.   Morphology studies show that pitting increases with increased AC

v.   The effect of AC is dependent on material and electrolyte conditions.

In this chapter theories will be reviewed related to ***how*** AC affects the electrochemical properties of carbon steel and stainless steel and ***why*** this happens.

2.3.1 Open circuit behavior

Laboratory studies [47] showed that corrosion potentials for carbon steels decrease to more cathodic potentials when exposed to AC, but subsequently stabilize at less negative potentials depending of the electrochemical system - the specific material and electrolyte. The development was explained as due to an activation of the surface followed by a subsequent increase in polarization resistance due to pH-effects and the formation of an oxide layer [47].

From weight losses measured at the open circuit potential (E_{OC}), corrosion rates were seen to increase both when carbon steel and stainless steel were investigated at the Norwegian University of Science and Technology (NTNU) by Hagen (2012) [48], see Figure 8.
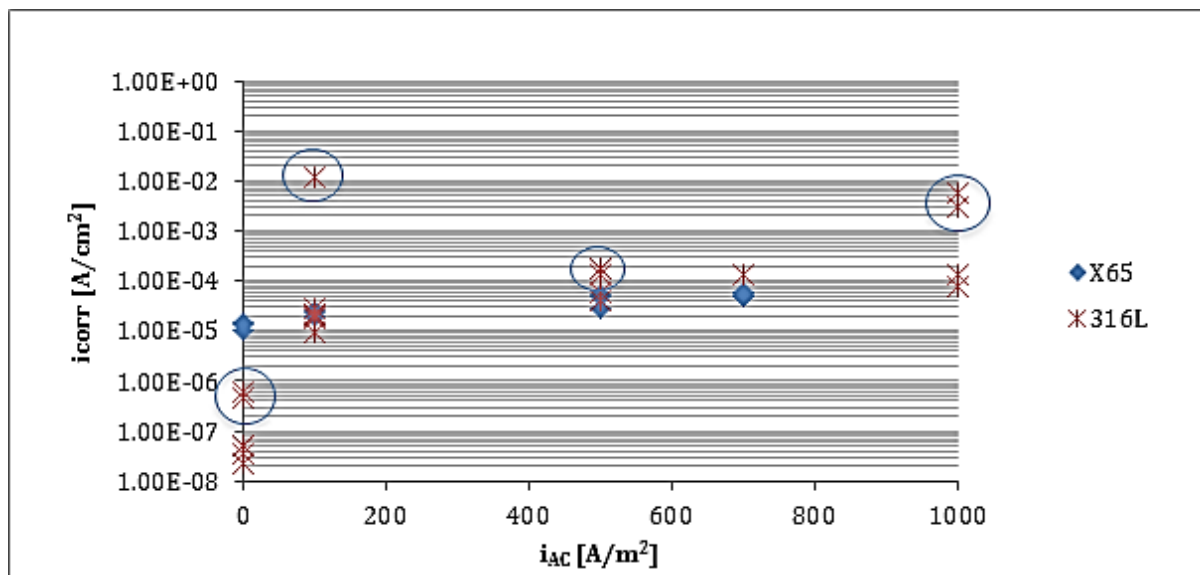
Figure 8: Corrosion current densities for X65 carbon steel and 316L stainless steel at the respective applied AC densities based on weight loss, polarization curves and LPR measurements. The latter results were for 316L discarded due to assumed incorrect values for Tafel slopes and are highlighted by blue circles in order to be identified [48].

AC was seen to destroy the passivity properties of stainless steel completely. It was however observed that corrosion rates stabilized from 500 A/m^2 AC.

2.3.2   Polarization behavior

When steel is polarized by a potentiostat either in the negative or positive direction, a sinusoidal AC signal present is seen to contribute to the resulting potential by superposition. The superposition is not symmetric some workers suggest [3, 49-51]. When the DC potential is low, the resulting voltage will be even lower when AC is applied, thus the AC induced corrosion rate increases with a decrease in the DC corrosion potential. The asymmetric current-potential response is in a theoretical work by Oldham [52] explained as a phenomenon related to the charging and discharging of the electrical double layer which provides a path to an applied AC current flow. For low AC amplitudes an amount of the AC will contribute to the electrochemical reaction generating a **constant** DC potential. For larger amplitudes however the magnitude of the DC potential produced was found to be proportional to the square of the applied AC and also to be dependent upon the rate constant and symmetry factor of the electrode reaction.

2.3.2.1   Frequency effects

In a recent theoretical work, Orazem [5] postulated that the background for asymmetrical response is the applied AC-frequency. At high frequencies the capacitive resistance of the double layer is seen to become so small that it acts like a wire letting all the current go through according to the equation:

$$Z_{Cdl} = \frac{1}{C_{dl} * \varpi} = \frac{1}{C_{dl} * 2\pi f} \tag{18}$$

Where:

Z_{Cdl} =double layer impedance

ϖ = angular frequency [rad/s]

However at low frequencies the current response of an electrochemical cell will be distorted when a large sinusoidal amplitude is applied, leading to a contribution of the AC applied potential to the faradaic reactions, given by:

$$i_f = i_{corr\ DC + AC} \tag{19}$$

The total current when a sinusoidal amplitude is applied at low frequencies was seen to be proportional with $\Delta V_{AC}{}^2$. As the mathematical calculations leading to the proportionality were based on Butler-Volmer, the proportionality will thus only be valid for activation controlled corrosion kinetics. The proportionality does hence not apply for stainless steels.

The importance of frequency is also established by others. By monitoring AC currents on a pipe steel as a function of number of cycles [53] Hosokawa found currents to peak when

frequency was set to 50 Hz. A later study [1] characterized this frequency to have the most severe effect on the AC corrosion risk.

2.3.2.2 Altered kinetics

The abovementioned results are consistent with voltammetric studies showing that processes related to H_2 and O_2 formation are accelerated when AC voltages of high amplitudes are applied. The formation of the gasses is reported to happen [54] at less negative and less positive potentials respectively. The phenomenon is explained as an increase in the time-average-constant k_f which according to Butler-Volmer shows an exponential dependence on the applied potential. When an AC perturbation is applied, the perturbation in DC potential leads to an acceleration factor, giving a new time-average-constant.

According to a theoretical study by Bosch and Bogaerts (1998) [49] the ratio of the anodic and cathodic Tafel slopes will determine the response of the electrochemical cell upon an applied AC, and thus the consequences for the resulting corrosion potential E_{corr}. It was derived that the variation of corrosion potential caused by AC is a function of the ratio of anodic Tafel slope to the cathodic Tafel slope. $(r = b_a/b_c)$. Both a positive and a negative shift is thus possible. It was shown that for $r < 1$ E_{corr} decreases, while it increases when $r > 1$. For $r = 1$ the corrosion potential is left unchanged. It is to be noted that the mathematic modeling of polarization curves leading to these results was done assuming that the Tafel slopes were not affected by the applied AC, something being confirmed in later mathematical models [51] and again disputed [3, 55] by results from experimental studies on carbon steel.

Hirschorn *et.al* [56] found that either the cathodic or the anodic reactions were accelerated by large AC amplitudes at a frequency of 50 Hz. Thus an asymmetric response will arise in the electrochemical cell, see Figure 9 for curves modeled mathematically from experimental results where *Ecorr* was found to make a negative shift when AC was applied.
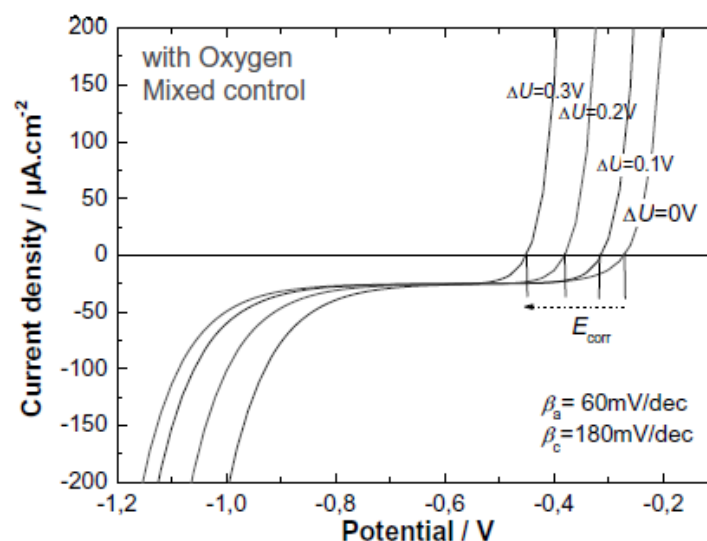
Figure 9: Polarization curves for carbon steel in the presence of AC perturbation calculated with contribution of oxygen diffusion at 50 Hz [56].

The debate has particularly focused on whether it is the cathodic reactions or the anodic that experience a change in overpotential with applied AC. The overpotential reduction was found [55] higher for cathodic processes than for the anodic see Figure 10, and it was proposed that AC may cause a variation in the double layer's chemical composition with a consequent change of the equilibrium potential and the growth of corrosion product films on the surface.

Solution	AC (A/m^2)	β_a (mV/dec)	β_c (mV/dec)	i_{corr} or i_0 (mA/m^2)	E_{corr} or E_{eq} $(mV\ SCE)$
Galvanised steel					
35 g/L NaCl	0	16	152	16	−1082
	30	46	124	26	−1200
	100	45	134	30	−1200
	300	49	132	60	−1212
	500	49	129	70	−1213
	1000	51	118	62	−1214
Carbon steel					
35 g/L NaCl	0	66	167	11	−780
	30	85	177	140	−812
	100	50	169	65	−790
	300	50	132	160	−818
	500	45	132	120	−818
	1000	164	137	280	−843

Figure 10: Parameters extracted from polarization curves recorded for different AC densities, under oxygen free conditions at room temperature (RT) [55].

The effect of AC on the anodic and cathodic overpotentials was studied in soil simulating solution and seawater[3]. From the results it was concluded that both anodic and cathodic overpotentials may decrease. Figure 11 shows how anodic polarization curves are affected by changes in the oxygen reduction reaction and the hydrogen evolution. Figure 12 shows the effect of AC on anodic overpotentials.
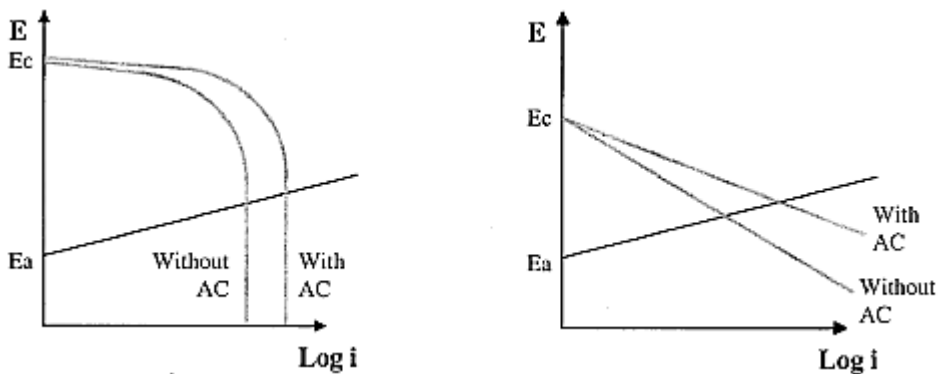
Figure 11: Schematic effect of AC current on cathodic overpotential: a) effect on oxygen reduction; b) effect on hydrogen evolution[3].
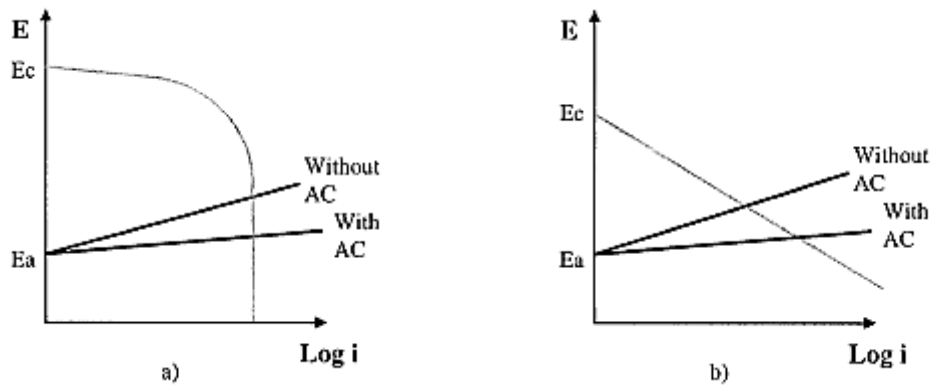
Figure 12: Schematic effect of AC current on anodic overpotential: a) cathodic process is oxygen reduction; b) cathodic process is hydrogen evolution [3].

Similar variations of cathodic and anodic Tafel slopes for carbon steel with AC current density have also been reported by Xu *et.al.* (2012) [57] where an enhanced hydrogen reaction was especially documented at high AC current densities. The increase in kinetics for the hydrogen reaction with increase in applied AC current density, was also reported in a master thesis by Stamnes [58] at NTNU however without an explanation to the phenomenon. Hagen (NTNU, 2012) [48]found cathodic Tafel slopes to decrease on carbon steel with increasing AC densities.

2.3.2.3   Current behavior under cathodic protection

When samples of 16Mn steel pipe were potentiostatically polarized in a laboratory study by Xu et.al [59], it could be seen that anodic currents developed at -850 mV/SCE when AC was applied and currents increased with increased AC density. At -1000 mV/SCE the opposite trend was observed: the current response showed a negative shift during the first half hour before currents again stabilized on less negative values, see Figure 13. The three regions depicted from the plot are (i) CP-1 region: from 0 to 1000 s, CP is applied on the steel; (ii) CP + AC region: from 1000 to 2000 s, various AC current densities are applied while CP is maintained; (iii) CP-II region: from 2000 to 3600 s, AC is stopped, but CP is maintained.
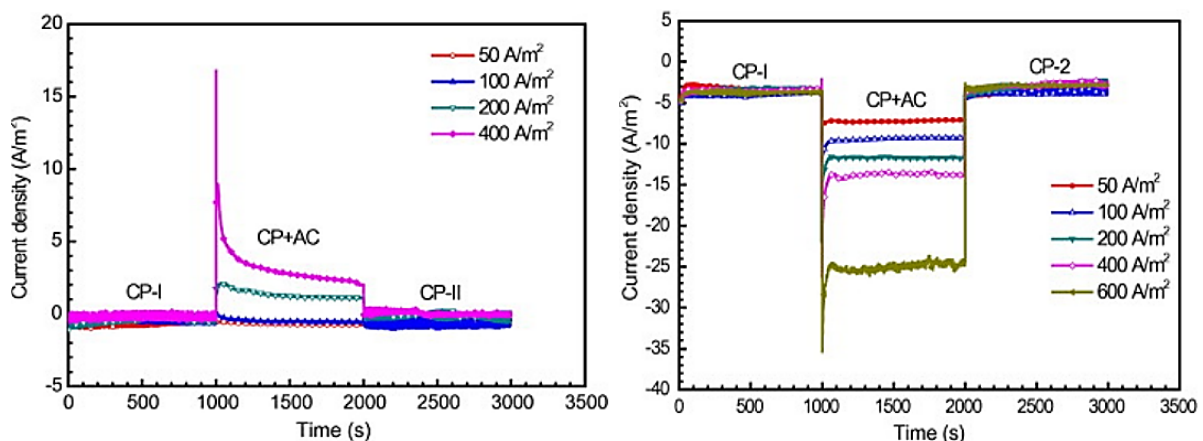
Figure 13: Current densities recorded on a 16Mn pipe steel with various i_{AC} under cathodic protection (CP) at left) -850 mV/SCE and right) −1000 mV/SCE applied potentiostatically. Figure from [59].

Cathodic current densities calculated from the current response recorded by Stamnes at -800 mV and -1050 mV (SCE) [58] depict as can be seen in Figure 14 that current demand under

cathodic protection increases with increased AC. Protection currents for cathodic protection are related to cathodic currents by $\left| I_{red} \right| = I_{ox} = I_p$.
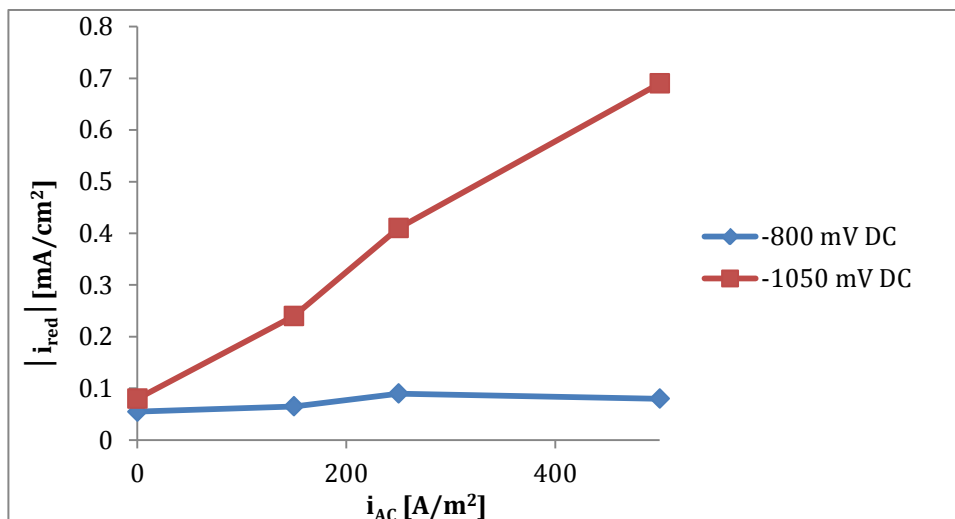
Figure 14: Cathodic current densities,$\left| i_{red} \right|$, for X65 carbon steel when increasing AC densities are applied during potentiostatic polarization in 3.5 wt.% NaCl. Plot adapted from results by Stamnes [58].

2.3.2.4 Passivity alteration

Stainless steels have not been subjected to studies as thorough as carbon steels and little literature is available, but there have been reported changes on the passivation current of stainless steels with superimposed AC from as early as the 1960s. From experiments on a stainless steel named(IH18B9T (according to the Polish nomenclature at the time) Juchniewicz [60] reported that the passivation potential in sulphuric acid decreased when AC was superimposed hence AC was seen to influence the current required for the potential to exceed the Flade potential. The author performed similar tests on platinum [61]showing that the main changes in corrosion parameters probably are caused by changes in capacitance and de-passivation of the metal during the negative half-cycle of AC resulting in increased corrosion rates. Recent studies on the electro dissolution of platinum under potentiodynamic and galvanodynamic conditions in combination with applied alternating current have shown that the maximum amount of dissolved platinum occurs at the frequencies close to 50Hz[62].

Voltammetric investigations have shown that the electrode processes at the platinum anode are irreversible, and that a decrease in dissolution rate, which was observed at high frequencies of the AC current, was attributed to a decrease in the rate of platinum oxidation with increased frequency.

From tests on AISI 304 changes in the corrosion potential with applied alternating voltage (AV) when recording polarization curves have also been reported [63]. The recordings were taken 10 minutes after samples were immersed. The behavior under AV was found to depend on the ratio of the anodic Tafel slope compared to the cathodic. The corrosion potential was seen to make a negative shift if the anodic Tafel slope was smaller than the cathodic Tafel slope, while the shift was positive if the anodic Tafel slope was greater than the cathodic Tafel slope. As can be seen from Figure 15 the potentials shifted in the positive direction.
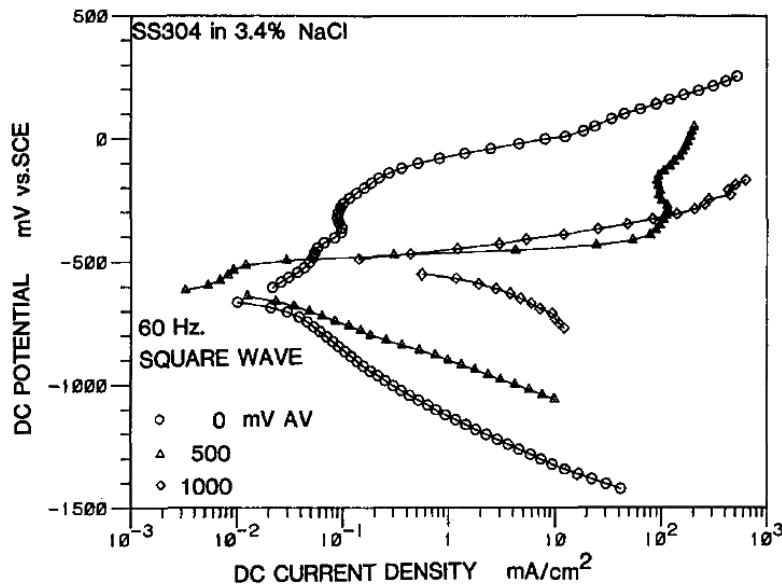
Figure 15: Polarization curves on 304 stainless steel in 3.5 wt% NaCl purged with nitrogen at applied AC voltages of 60 Hz [63]. In this study the corrosion potentials shifted to more positive potentials.

In a laboratory study by Statoil [64] on supermartensitic stainless steel (SMSS) and carbon steel both of unknown type, it was pointed that not only do cathodic Tafel slopes decrease with increased AC voltage, the oxygen reduction reaction was seen to disappear completely from the curves. While the former was observed for both carbon steel and SMSS, the latter was only found to be true for the SMSS. It was proposed that the evolution of hydrogen either makes a shift to more positive values for E^{rev} or that en increased exchange current density caused the increase in current density – the result being a shift from a passive behavior to a more active corrosion behavior when applying AC. The samples were prior to the potentiodynamic polarization tests conditioned with AC during 60 minutes at 500 rpm. During that time the corrosion potential shifted from approximately -610 to -875 mV for carbon steel and from -164 to -545 mV (SCE) for SMSS.
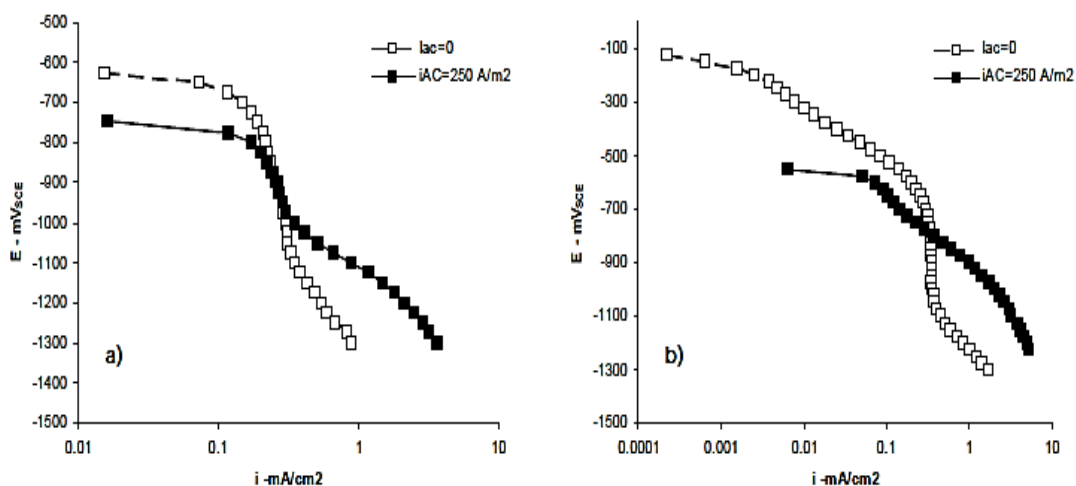
Figure 16: Effects on cathodic polarization curves caused by an applied AC current density of 250 A/m² when curves were recorded at 500 rpm in 3.5 wt% NaCl on a) carbon steel b) SMSS [64].

When recording polarization curves on austenitic stainless steel of AISI 316L, the same trend was observed by Hagen [48] regarding an increased exchange current density for the

hydrogen reaction. Also a transition from the corrosion reaction being determined by oxygen reduction to hydrogen evolution was seen for increased AC densities. The oxygen reaction disappeared entirely from polarization curves. Even at potentials as high as -600 mV (SCE) hydrogen evolution was the predominant cathodic reaction, as can be seen in Figure 17.
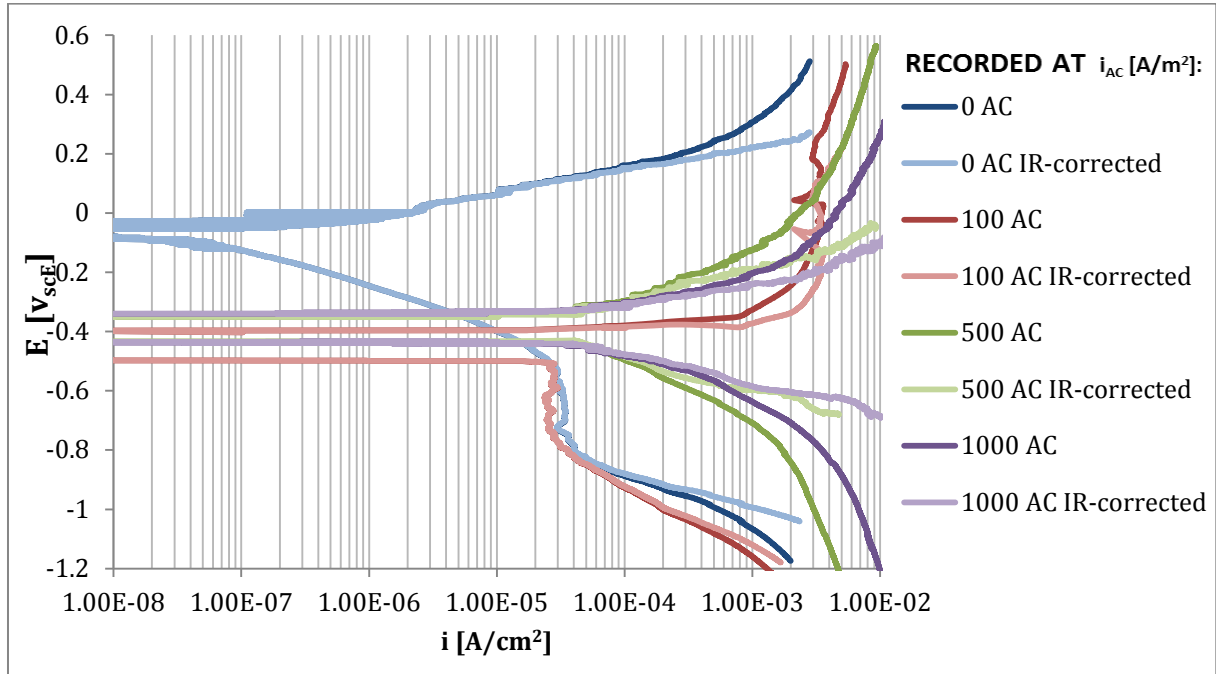
Figure 17: Polarization curves recorded for AC densities from 0 to 1000 A/m2 on stagnant electrodes of AISI 316L type of steel immersed in 3.5 wt% NaCl for 72 hours at a sweep rate of 0.167 mV/sec [48].

A comparison of the linear polarization resistance (R_P) on 316L stainless steel relative to X65 carbon steel during the same project showed that R_P for stainless steel decreased dramatically with applied AC, taking the same values as for carbon steel from 500 A/m^2 AC, see Figure 18.
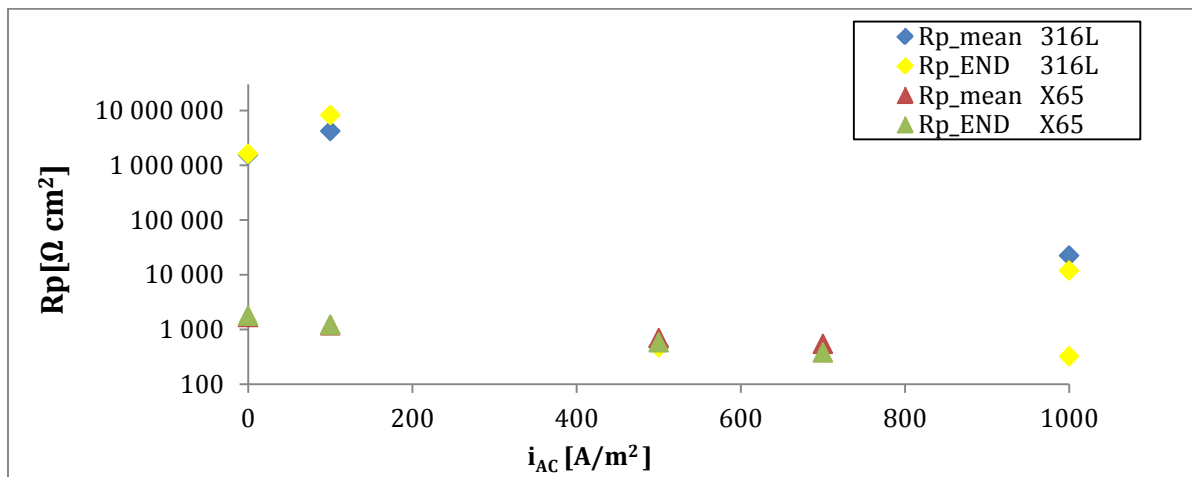
Figure 18: Mean and final values for polarization resistance for 316L and X65 as a function of applied AC current density for experiments in 3.5 wt% NaCl [48].

At 100 A/m^2 AC the polarization resistance is similar or higher to the value measured in the absence of AC, but an individual plot over R_P as a function of time at this AC current density

revealed that half of the time the experiment lasted, the resistance was as low as for carbon steel, see Figure 19.
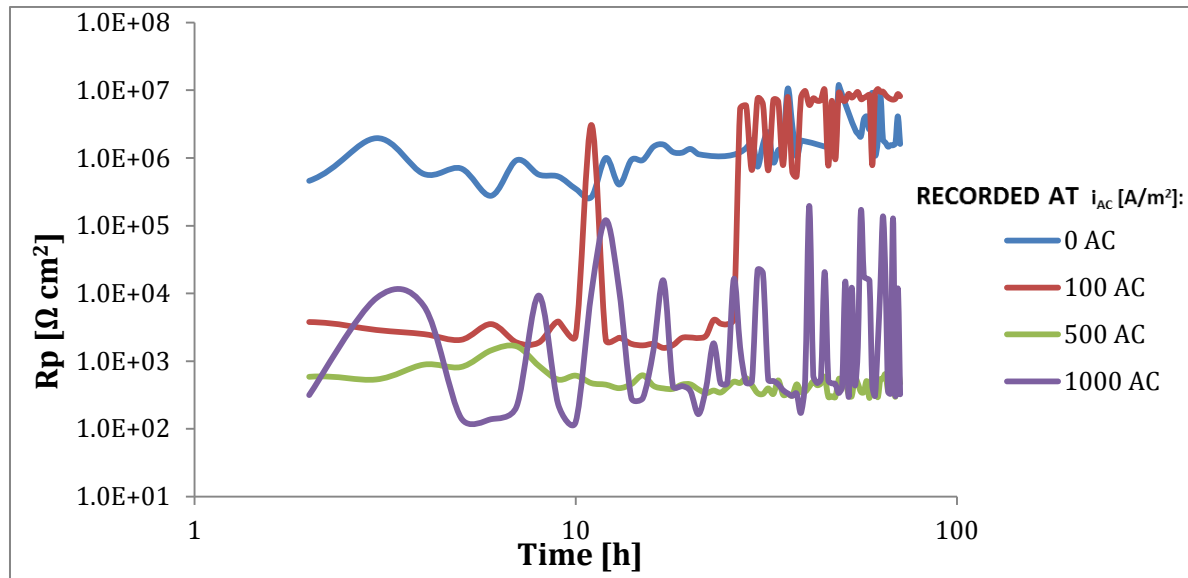
Figure 19: Polarization resistance as a function of time for 316L, when samples have been tested for 72 hours in 3.5 wt% NaCl [48].

The decrease in R_P with increased AC current density was related to a localized breakdown of the passive oxide film on 316L resulting in oxidation rates as high as for X65 due to the high cathode-to-anode geometry evolving on the surface with the pitting.

As can be seen from Figure 20, corrosion potentials measured under open circuit conditions dropped instantaneously after AC was applied, a shift which was not reversed. Also polarization curves showed the same negative potential shift with AC.
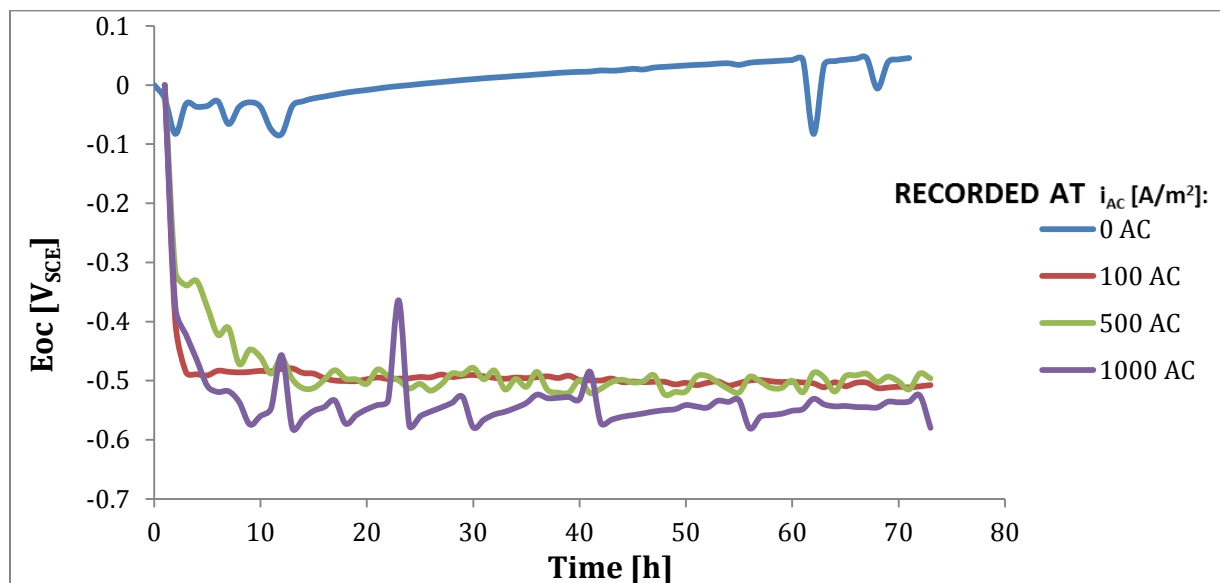
Figure 20: Corrosion potential as a function of time for 316L, when samples were tested for 72 hours in 3.5 wt% NaCl.

2.3.3   Corrosion rates

Corrosion rates have been found to depend on the frequency of the AC signal. When carbon steel was tested by Pagano *et.al* [47] in seawater at open circuit conditions, it was found that corrosion rates decreased when frequencies where increased, see Figure 21.
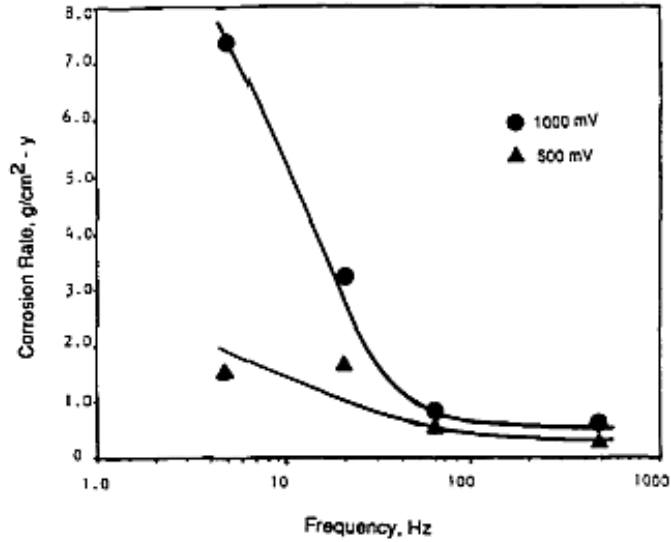
Figure 21: The relationship between corrosion rates of carbon steel and frequency of the applied AC peak voltage amplitudes at 500 mV and 1000 mV, measured at RT in oxygen free seawater[47].

Under cathodic protection the corrosion of steel is seen to decrease [59], but the effect becomes less apparently in the presence of AC as can be seen from Figure 22.
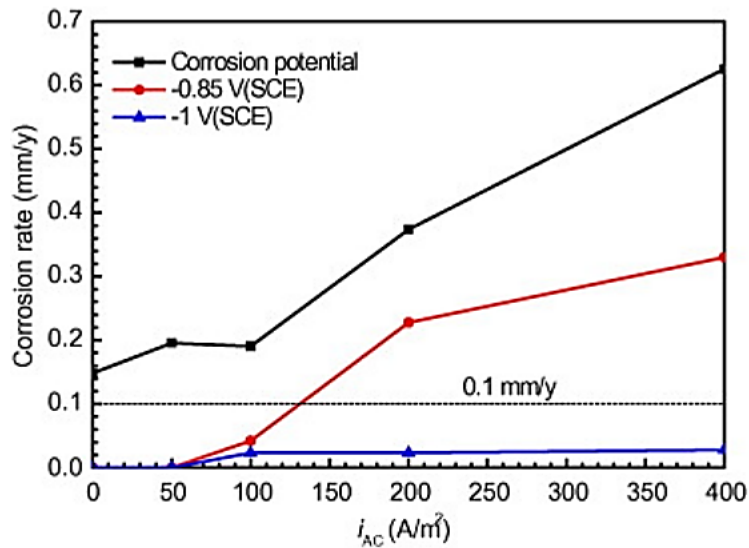
Figure 22: Corrosion rates determined by weight loss measurements for steel coupons under various i_{AC} and CP potentials after 48 hours of immersion in the simulated soil solution [57].

The increased corrosion rates on carbon steel at low frequencies have been explained due to an alkalization effect [65, 66] destabilizing the oxide layers. The alkalization is explained to arise from influence of either the anodic or cathodic DC current along with AC sources which electrochemically reduces water into OH^-, see eq. (11) and eq.(12).

Other studies [4] proposed that non-protective porous layers of ferrous oxides formed during a dominating cathodic half cycle by the sinusoidal AC signal were detrimental for the corrosion rates, while again others found that only when CP potentials are sufficiently negative, the steel will be under a complete protection[57, 66].

The results are however in contradiction to work by Nielsen [65] pointing out that increasing the CP would not necessary enhance the protection of the steel, due to the fact that at higher CP potentials pH will increase leading to an even faster destabilization process of the passive oxides and hydroxide layers on the steel.

Experiments performed by Stamnes [58] concluded that in particular the combination of high cathodic currents and high AC potentials would lead to increased corrosion currents, see Figure 23 for results for carbon steel samples tested at E_{OC} in addition to tests at different cathodic potentials.
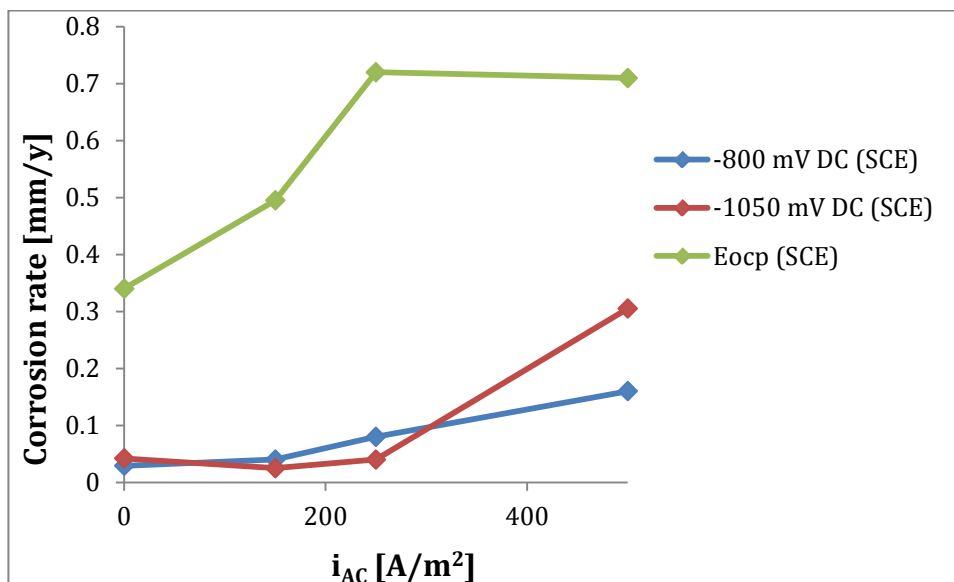
Figure 23: Corrosion rates for X65 carbon steel as calculated from weight losses measured at increasing AC densities are applied. Results from experiments under cathodic potentiostatic polarization are plotted along with results from experiments at E_{OC}. Plot adapted from results by Stamnes [58].

It is important to note that weight loss measurements are in general reported to result in higher corrosion rates than those determined by electrochemical methods, when AC densities of increasing magnitude are applied.

2.3.4 Surface morphology

Carbon steels have under visual inspections shown no signs of corrosion products under CP conditions in the absence of AC. However red rust products have been seen to evolve with increased AC current densities applied, even though under CP condition [66]. It was found

that corrosion products formed in one place but spread out over the entire surface, such that at high AC densities, 90% of the surfaces were covered.

At low AC current densities carbon steels have been found to degrade uniformly, while pitting corrosion occurred extensively on the steel surface at high AC current densities, a process enhanced in the presence of chloride ions [67].

These results are in contradiction to studies [4] that documented pitting at all AC current densities applied on carbon steels tested at open circuit potential. Pits were reported to propagate after an initial induction period where the severity of pitting was seen to increase as a function of the applied AC density. Stainless steels were found by Hagen [48] to corrode by a localized corrosion mechanism with applied AC current density and pits were mainly found at corners and edges.

2.4   Discussion

Several models and experimental studies on the AC corrosion of steels have been presented in the last chapter. Some general lines can be drawn from the literature presented:

- Stainless steels are prone to localized corrosion. The passive film layer may be destabilized by Cl⁻ at microstructural weak sites on the surface of the steel.
- The polarization resistance of stainless steels was found to decrease dramatically when AC was applied. At the same time corrosion potentials have been seen to make negative shifts. The potentials recovered to less negative values but never to the initial values. Negative shifts of smaller magnitude have also been reported for carbon steel.
- Hydrogen evolution is seen to be a key reaction to the understanding of the AC mechanism. Tafel slopes for hydrogen evolution have been found to decrease with increasing AC densities applied. For stainless steel it was also found that the exchange current density for hydrogen was increased by AC.
- During cathodic potentiostatic polarization tests on carbon steel, the current response was seen to make positive shifts when tested at -850 mV/SCE while the response shifted the opposite direction at -1000 mV/SCE. The shifts increased with increased AC.
- Cathodic current densities for both carbon steel and stainless steel have been found to increase with increased AC densities.
- Weight losses for both carbon and stainless steel are reported to increase with increased AC density.

In accordance with this, the following effects of AC may be expected:
316L is expected to exhibit a higher cathodic activity than X65, when AC is applied. 316L is expected to result in lower corrosion rates than X65 when cathodically polarized at -800 and -1050 mV (SCE). 25Cr is expected to lose its passivity at AC densities above 100. An increase in the kinetics for the hydrogen reaction is also suspected.

3   Experimental

The methods described in this section cover test equipment and procedures used for immersion corrosion testing of metals with applied AC and the circuit chosen for this purpose.

All procedures for preparing bare solid metal for immersion tests, for removing corrosion products after the tests have been completed and for evaluating the corrosion damage that has occurred, are described.

The laboratory procedures are in accordance as far as possible with the methods described in practice standards [68-70].

3.1   Test specimen

Three materials have been tested for this study: AISI 316L stainless steel (SS), 25Cr super duplex stainless steel (SDSS) and X65 carbon steel (CS).

3.1.1   Material specification

The samples of AISI 316L SS were manufactured from a plate delivered by NTNU's technical laboratory of materials (Finmekanisk verksted, DU3). See Table 1 for information about the chemical composition.

Table 1: The chemical composition (wt%) of 316L SS used in the experiments.

Chemical composition								
	C	Cr	Ni	Mo	Mn	Si	P	S
AISI 316L SS	<0.03	16-18.5	10-14	2-3	<2	<1	0.045	<0.03

The 25Cr SDSS was delivered by *Smith Stål Nord Trondheim* as a plate which was manufactured into samples by NTNU's technical laboratory of materials (Finmekanisk verksted, DU3). See Appendix E.4 for the certificate of the material and Table 2 for information about the chemical composition.

Table 2: The chemical composition (wt%) of 25Cr SDSS used in the experiments.

Chemical composition									
	C	Cr	Ni	Mo	Mn	Si	P	S	Cu	N
25Cr SDSS	<0.017	25.75	6.88	3.77	0.58	0.29	0.021	0.0004	0.17	0.2780

The samples of X65 carbon steel were manufactured from a pipe by SINTEF (Materialer og kjemi, Perleporten). See Table 3 for information about the chemical composition.

Table 3: The chemical composition (wt%) of X65 CS used in the experiments.

Chemical composition								
	C	**Si**	**Mn**	**P**	**S**	**V**	**Nb**	**Ti**
X65 CS	0.16	0.45	1.65	0.020	0.010	0.09	0.05	0.06

Only the 25Cr type of steel was delivered with a certificate and the above listed information about the chemical composition is thus according to standards for such alloys [71].

3.1.2 Pretreatment

For all measurements, polished electrodes were used. While X65 CS samples were delivered polished, samples of 316L SS and 25Cr SDSS types of steel were polished by successively using finer grade of emery papers (220-500-1000grade) on a standard grinding table (KII) with running water. Specimens were engraved with a metal marker pen in order to keep track of samples (KII), and then washed with distilled water, acetone and ethanol 96% in that order prior to drying and weighing. The samples were dried using hot air from a blow drier. The following weighing was done on a standard analytical weight with an error of ±1mg.

3.1.3 Sample geometry

Samples were ordered in sizes of 80*20*2 mm, see Figure 24. The 25Cr specimens were manufactured from a thinner plate (≈1.5 mm) and each test sample had to be measured individually. Thickness of specimens could in general vary ± 0.2 mm.

Figure 24: The geometry of test samples. The area without paint insured electrical conduction between sample and electrolyte, at the bottom, and between sample and the clamp, at the top.

Due to the limited power output from the AC supply – the variAC – the exposed area of the samples was chosen to be 6.56 cm^2 for tests at AC densities of 0, 100 and 500 A/m^2 and 2.6 cm^2 for densities above, see Table 4 for dimensions.

Table 4: The dimensions of samples.

Sample dimensions			
	Height [cm]	Width [cm]	Thickness [cm]
$A_{exposed=6.56}$ ($i_{AC} \leq 500$ A/m^2)	1.4	2	0.2
$A_{exposed=2.6}$ ($i_{AC} > 500$ A/m^2)	0.5	2	0.2

The area not to be exposed to the electrolyte was coated with "Microshield - Stop off laquer" applied with Q-tips, see Figure 25 for information.

Figure 25: The coating and drying of samples took place in vented hood due to highly volatile lacquer.

This is a type of acetone-diluted acid-proof coating often used in laboratory experiments due to its favorable properties with respect to adhesion, curing time and easy removable. Initially, masking tape was used in order to get straight lines of coat on test-samples prior to experiments. But since the tape leaved traces of glue which were difficult to clean off, the coating was applied by free-hand.

All specimens were dried for 24 hours before a new layer of coating was added, and for another 24 hours prior to immersion into electrolyte.

3.2 Test procedure

The experiments were carried out in 3.5 wt% NaCl, an electrolyte holding the same salinity as water in the North Sea. The electrolyte was made by adding 365 g of reagent grade NaCl into a container and adding 10L of distilled water, stirring and storing the container lidded to avoid evaporation and thereby concentration errors.

Lidded glass beakers of 1.5 L were used as cells where the electrolyte was constantly stirred by an electrical driven glass rod in order to keep the oxygen content constant and homogeneous. Rotational speed was kept at 100 rpm for all cells.

Platinum counter electrodes and standard calomel reference electrodes (SCE) in saturated potassium chloride (KCl) were used. The reference electrodes displayed + *0.244 V vs. SHE* at 25 °C when used in combination with the saturated KCl solution, hence $E_{SHE} = E_{measured} + 0.244\ V$. All the DC potentials are hence reported versus this reference electrode.

The salt bridges for ionic contact between reference electrodes and immersed samples were prepared every two weeks by heating saturated KCl up to the boiling point, adding agar and

sucking the mixture up into U-shaped glass tubes delivered by the technichal laboratory at NTNU (Glassblåseverksted, DU3).

Cells were during experiments immersed into a temperature controlled chamber holding 25°C. The water in this chamber was constantly stirred. When removed from electrolyte, samples were stripped for coating with acetone and corrosion products were removed chemically. Inhibited hydrochloric acid was used on X65, while nitric acid was used on the stainless steels. Samples were then washed, dried and weighted.

3.2.1 Apparatus set-up

The circuit used is the same as utilized during several years of AC-studies at NTNU, based on a circuit first developed by Bolzoni *et al.* [3] and later modified by Statoil to enable the use of a potentiostat. The circuit can be seen in Figure 26.
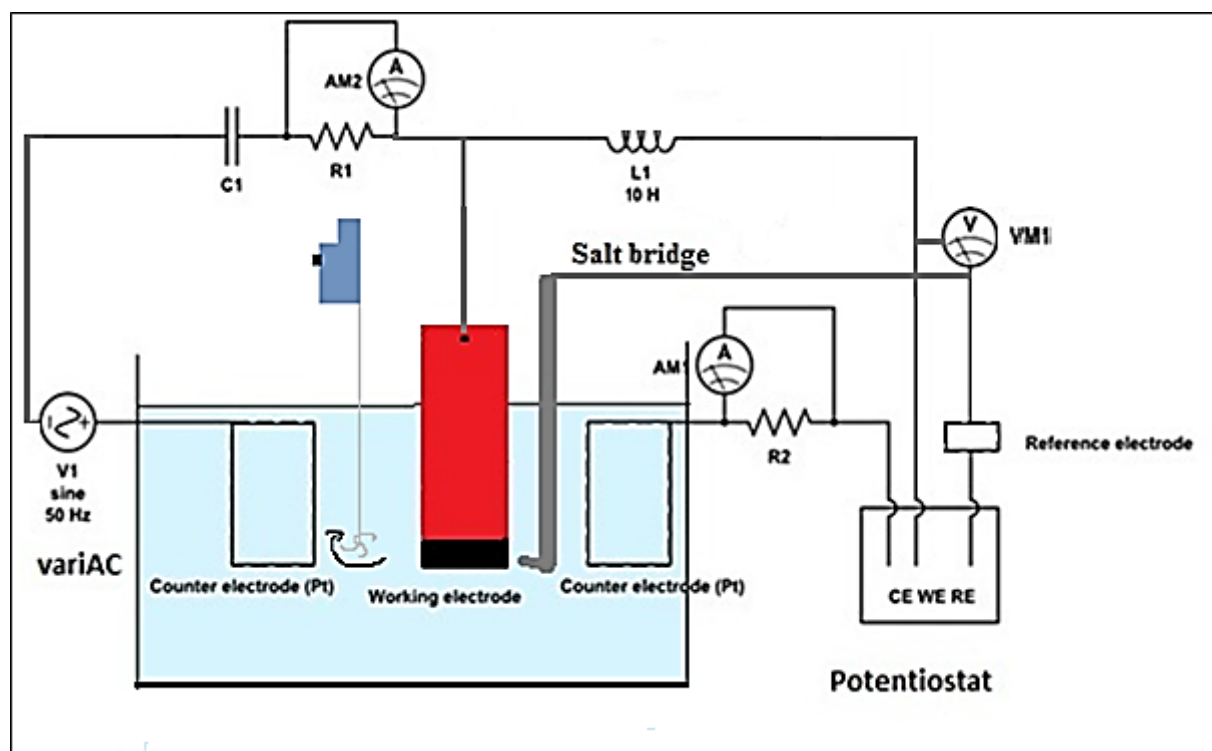
Figure 26: The electrical circuit used for both steel grades throughout all experiments. The AC part of the circuit is seen on the left while the DC part is seen on the right. A capacitor was introduced in the AC part to filter away DC signals and an inductor was introduced in the DC part to filter away AC signals.

All equipment that needed electrical supply was grounded and isolated by use of a transformer. See Figure 27 for information about the experimental set up and the apparatus in use.

Before experiments were initiated, all clamps and wires were checked for conductivity, and clamps were grinded in between all experiments to assure no corrosion products hindered perfect conductivity.
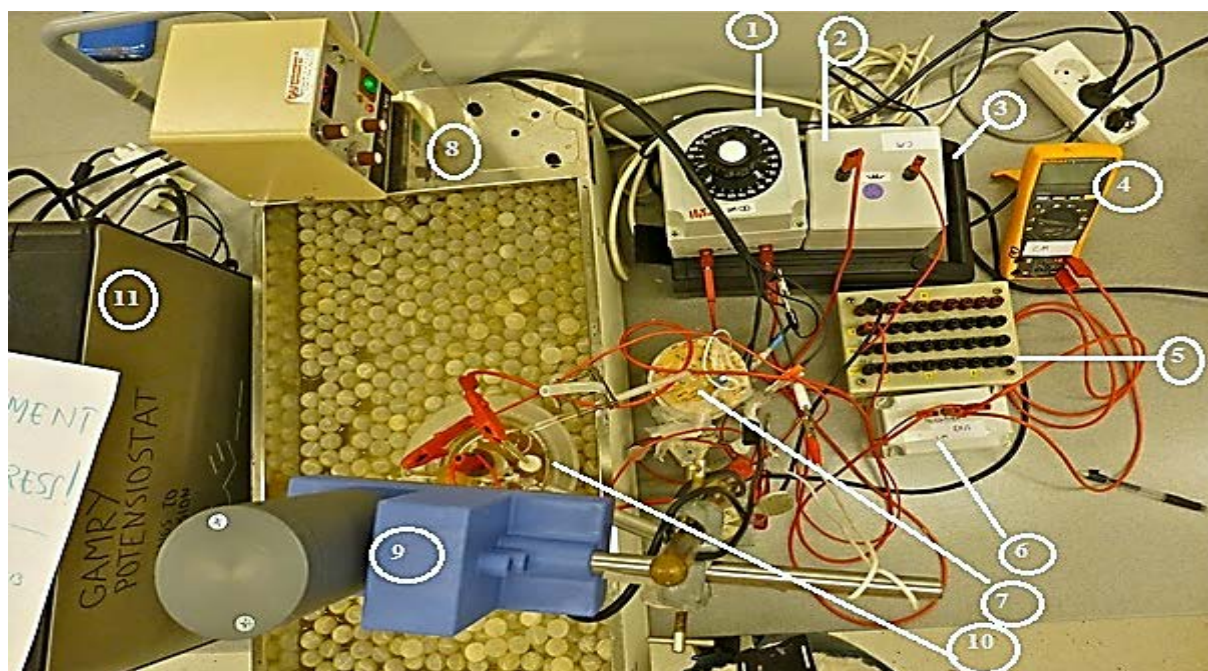
Figure 27: The apparatus required to perform the experiments: 1)VariAC 2)inductor 3)transformer 4)true-RMS multimeter 5)DC-resistance 6)capacitor and AC-resistance 7)calomel reference electrode 8)water bath with temperature controller and stirrer 9)stirrer for the test cell 10) the test cell 11)Gamry potentiostat

A VariAC was used as AC supply and in-PC Gamry potantiostats were used to monitor and effectuate different electrochemical technique programs. The Gamry potentiostat uses the Gamry Framework™ Software for data acquisition and the Echem Analyst™ for data analysis. Also Bank MP-81 Potentiostat (analog type) and an HP logger with Agilent 34830A Benchlink Data Logger Pro as software was in use during the experiments.

The VariAC delivered voltages at 50 Hz frequency in sinusoidal waves unfortunately at oscillating values, making it necessary to fine-tune the AV during experiments.

Fluke "TrueRMS"-multimeters were inserted into the circuit to monitor potentials and make it possible to do the AV tuning. In the AC part of the circuit a 500 µF capacitor was inserted to filter DC current. In the DC part of the circuit an inductor of 10 L was inserted to filter AC current. Both the capacitor and the inductor inserted resistances that needed to be considered for calculations and measurement corrections.

3.2.2 Electrochemical methods

Two sets of electrochemical experiments were performed:

1) *Cathodic polarization:* Samples of 316L and X65 were **potentiostatically** polarized at -800 mV and -1050 mV while AC densities at constant values were applied during experiments lasting from 72-96 hours for the stainless steel and 48 hours for the carbon steel.

2) *Anodic polarization***:** In order to maintain passivity, which for 316L was found to be impossible [48] for all applied AC values, the tests were performed on samples of 25Cr type

of steel. Potentiodynamic polarization curves were recorded with a sweep rate of 60 V/h = 0.167 mV/sec to -1200 mV and +1000 mV for AC densities between 0 and 1000 A/m^2 AC after an exposure period of 72 hours. A polarization in cathodic direction was recorded first before waiting for the potential to stabilize and subsequently recording the anodic polarization curve.

The knowledge about the passive region was used in following experiments where samples were **potentiodynamic** polarized by **ramping** the potential up to the passive potential area with a sweep rate of 0.015 mV/s followed by a **potentiostatic polarization** at the specific potential. AC densities at constant values were applied during experiments lasting a total of 72 hours.

3.2.3 Removal of corrosion products

Corrosion products were removed by a chemical treatment, as described in ASTM G1-03 (2011) [70]. Specimens of X65 type of steel were immersed in inhibited hydrochloric acid (HCl) while specimens of 316L and 25Cr type of steel were immersed in heated diluted nitric acid (HNO$_3$), seeTable 5 for information.

Table 5: The chemical cleaning procedure for removal of corrosion products.

	Solution	*Cycle time*	*Temperature*
X65	- 500 mL HCl (SG 1.19) - 3.5 g hexamethylene tetramine - Reagent water to make 1000 mL	30 sec	20 - 25 $^{\circ}$C
AISI 316L SS **25Cr SSDS**	- 100 mL HNO$_3$ (sp gr 1.42) - Reagent water to make 1000 mL	20 min	60 $^{\circ}$C

By weighing the control specimen before and after cleaning, the extent of metal loss resulting from cleaning was utilized to correct the corrosion mass loss, see Figure 28 for information about this experimental step.
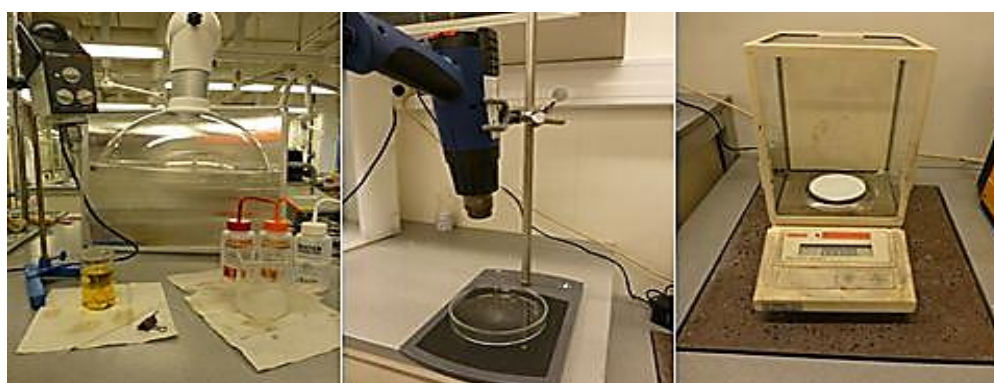
Figure 28: The process of removal of corrosion products, here illustrated for X65. Immersion into HCl for a number of times, then cleaning, drying and weighing.

3.3 Surface characterization

Characterization of the surfaces were carried out both on a macroscopical and a microscopical level:

i) A visual examination of the corroded specimens was carried out. Photographs were taken both prior to removal of corrosion products and after the removal.

ii) A morphological study of all surfaces was performed by Scanning Electron Microscopy (SEM). The chemical composition of films formed on 316L samples was investigated with Energy-dispersive spectroscopy (EDS). A LVSEM Hitachi S - 3400 (KII) at an accelerating voltage of $E_0 = 10$ kV-15 kV and a working distance of $a = 4.9$ mm – 10 mm was employed for these tasks.

4   Results

The main scope of this research was to study the polarization behavior of stainless steel as a function of applied AC densities. A total of 55 individual experiments have been performed during this study, with a duration of minimum 2 days and maximum 4 days: The first one was carried out to test the reproducibility of data. Then 23 tests were carried out on 316L, 17 were performed on X5 and nine on 25Cr.

Key results from experiments are reported in this chapter, while the Appendices serve as a platform for in-depth information regarding all parallels carried out in the order as follows:

> **Appendix A** presents calculation techniques used to evaluate the data
> **Appendix B** presents results from reproducibility investigation
> **Appendix C** presents results for 316L parallels
> **Appendix D** presents results for X65 parallels
> **Appendix E** presents results for 25Cr parallels

In the first part of this chapter results for cathodic potentiostatic polarization experiments are reported for 316L together with results from similar experiments on X65 for comparison reasons. A minimum of two parallels were carried out for each experiment. In the second part results for anodic potentiostatic polarization tests are reported for 25Cr SDSS. A minimum of one parallel was carried out for each experiment. In the third part a summary of results will be given.

The current response measured will be referred to as either positive or negative, as weight losses are not negligible. Currents calculated based on the current response and the weight losses will hence be referred to as either anodic or cathodic. All DC potentials reported here are versus the reference electrode used, a standard saturated calomel electrode (SCE) at +0.2444 V vs. SHE at 25 °C. All AC potentials reported here are RMS values as recorded by Fluke multimeters inserted in the circuit. It is also to be noted that for certain plots logarithmic scales have been used.

4.1   The effect of AC on the cathodic behavior of stainless steel

Experiments were performed on 316L with a duration of minimum 3 days (72 hours) at AC densities of 0, 100, 500 and 1000 A/m^2 and on X65 with a duration of 2 days (48 hours) at AC densities of 0, 100, 500 and 700 A/m^2. To ensure that the system had stabilized at 0 A/m^2 AC on 316L, tests were let to last 96 hours.

4.1.1   Polarization behavior

During the potentiostatic polarization at -800 mV and -1050 mV the DC current response was recorded as well was the AC cell potential (V_{AC}) at the specific applied AC density. The V_{AC} was recorded both for 316L and for X65 by a multimeter inserted in parallel with the working electrode and the counter electrode in the AC part of the circuit. Values have been averaged over the period of time in order to recognize whether an increase or decrease with AC

densities and DC potentials has happened. Key results from these recordings are summarized in Table 6.

Table 6: Key results from the cathodic polarization experiments on 316L and X65. i_net values are averaged over the period of time for two-four parallels. Values for i_{NET_START} are collected 1.5 hours into the experiments.

316L						
i_{AC} [A/m^2]	**-800 mV DC**			**-1050 mV DC**		
	$\overline{V}_{AC}$ [V]	i_{NET_START} [A/cm^2]	i_{NET_END} [A/cm^2]	$\overline{V}_{AC}$ [V]	i_{NET_START} [A/cm^2]	i_{NET_END} [A/cm^2]
0	-	-3.00E-05	-3.35E-05	-	-1.62E-05	-1.24E-03
100	0.640	-5.30E-05	-5.90E-05	0.510	-6.88E-04	-8.07E-04
500	1.61	-1.20E-03	-4.49E-04	1.63	-2.98E-03	-1.37E-03
1000	1.62	-3.04E-03	-1.50E-03	1.62	-7.61E-03	-3.00E-03
X65						
i_{AC} [A/m^2]	**-800 mV DC**			**-1050 mV DC**		
	$\overline{V}_{AC}$ [V]	i_{NET_START} [A/cm^2]	i_{NET_END} [A/cm^2]	$\overline{V}_{AC}$ [V]	i_{NET_START} [A/cm^2]	i_{NET_END} [A/cm^2]
0	-	-2.76E-05	-2.99E-05	-	-1.22E-04	-5.69E-04
100	0.299	1.17E-06	-4.32E-05	0.377	-1.76E-04	-4.41E-04
500	1.37	-2.63E-05	-4.80E-05	1.46	-8.03E-04	-1.28E-03
700	1.03	-2.19E-05	-4.80E-05	1.14	-1.45E-03	-2.35E-03

Additional information about calculations is to be found in Appendix A and particular information about current response recordings for 316L and X65 parallels, is to be found in Appendix C.2 and D.2 respectively.

Start values for DC current response were collected 1.5 hours into the experiment in order to capture the effect of applied AC onto the DC current response, as the DC current response for both 316L and X65 was seen to oscillate at the start of the experiments.

Another concern was that current densities for X65 were seen to become positive sometime after AC was applied before returning to negative values when polarized at -800 mV. At -1050 mV this was not seen to happen.

As can be observed from plots for X65 in Figure 31 - Figure 32 the DC current responses did not become positive at the same time – for 100 A/m^2 AC the positive DC currents evolved 70 minutes into the experiment and were again negative after 95 minutes, while at 500 A/m^2 AC and 700 A/m^2 AC the positive currents evolved immediately after start. See Table 7 for data about the positive current response.

Table 7: Information about the length of time positive currents were present and the charge related to these currents.

i_{AC} [A/m^2]	$t_1 - t_2$ [min]	$\Delta t_{currents}$ [min]	Q [As]
100	70 - 95	25	2.18E-06
500	3 - 41	38	5.43E-04
700	5.4 - 62	57	3.43E-04

It is to be noted that experiments at 0 A/m^2 AC lasted 96 hours, while for all other AC densities the experiments only lasted 72 hours.

From the data provided in the table, it is worth noting:
1) The AC cell potentials V_{AC} were higher for the experiments on 316L than for those on X65.
2) The current response i_{NET} was higher for 316L than for X65 at all times.
3) The current response increased in the cathodic direction with increasing AC densities.

The obtained DC current response curves as a function of time are for 316L shown in *Figure 29 - Figure 30* and for X65 these are shown in *Figure 31-Figure 33.*
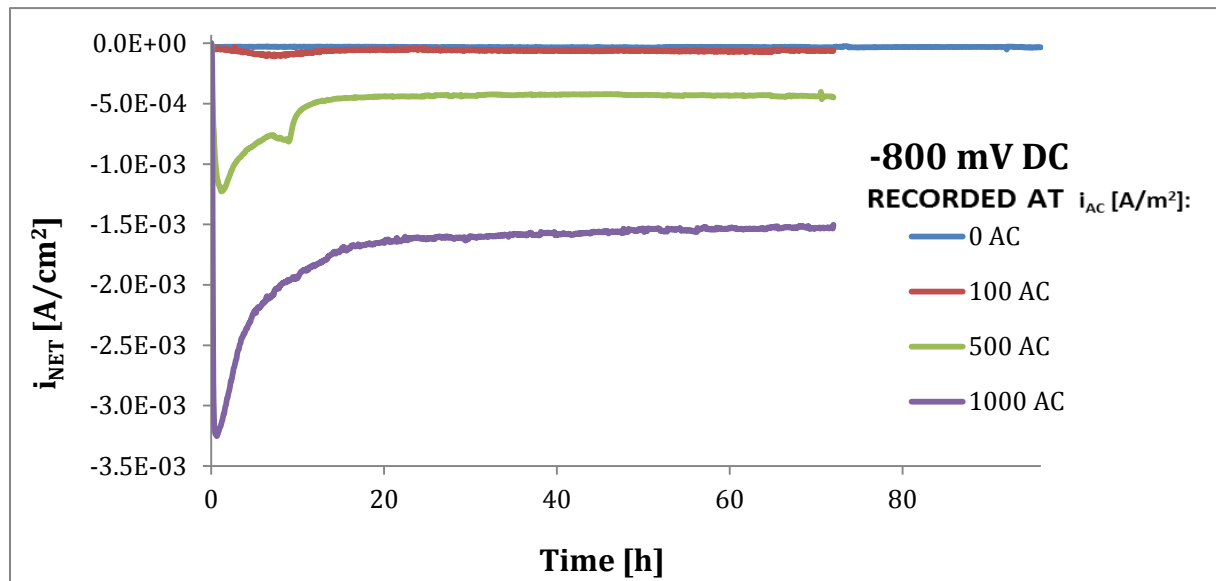
Figure 29: The recorded current density response for experiments on 316L under cathodic potentiostatic polarization at -800 mV as a function of time when samples have been tested for 72-96 hours for increasing AC densities. Experiments lasted 96 hours for samples tested at 0 A/m^2 AC to ensure stabilization of values.
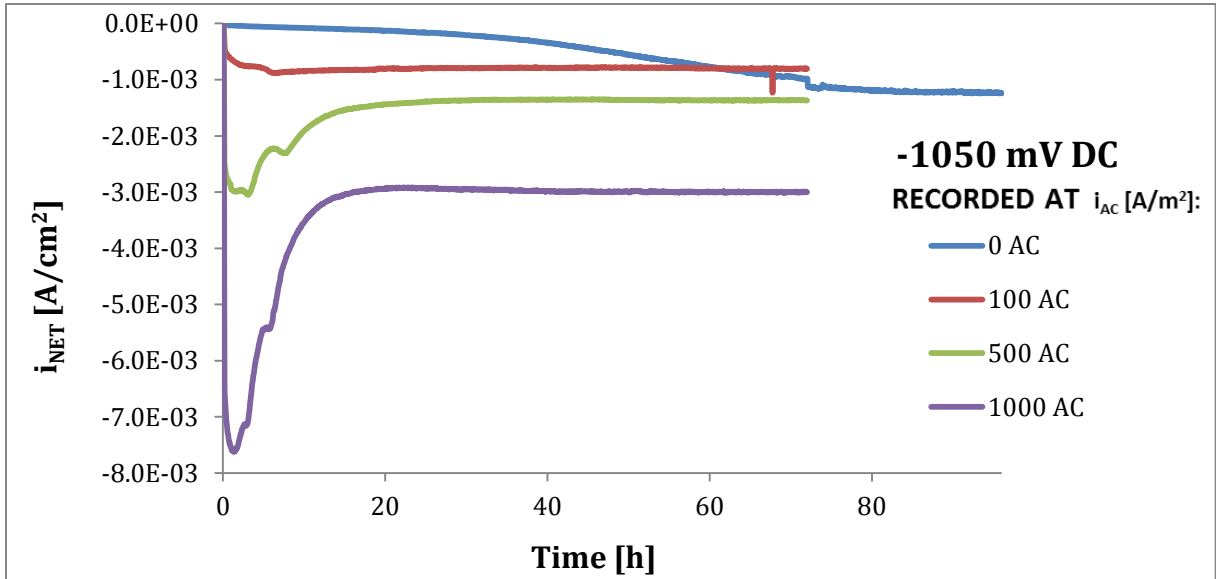
Figure 30: The recorded current density response for experiments on 316L under cathodic potentiostatic polarization at -1050 mV as a function of time when samples have been tested for 72-96 hours for increasing AC densities. Experiments lasted 96 hours for samples tested at 0 A/m² AC to ensure stabilization of values.

For 316L it can be observed that for the highest AC densities applied, the current response was more negative during the first ten hours of the experiment before it stabilized on less negative values, as it also could be noted from the data in Table 6. It should also be noted that at -1050 mV and no applied AC, the DC current continued to drop until it was more negative than at 100 A/m² AC.

A similar trend for the current response for X65 at 0 A/m² AC and -1050 mV can also be seen from Figure 33. Figure 31 shows the trend for current response in time at -800 mV, whereas Figure 32 shows the first five hours in detailed manner. As can be seen, the DC currents were positive for a period of time after AC was applied, before they stabilized on negative values.
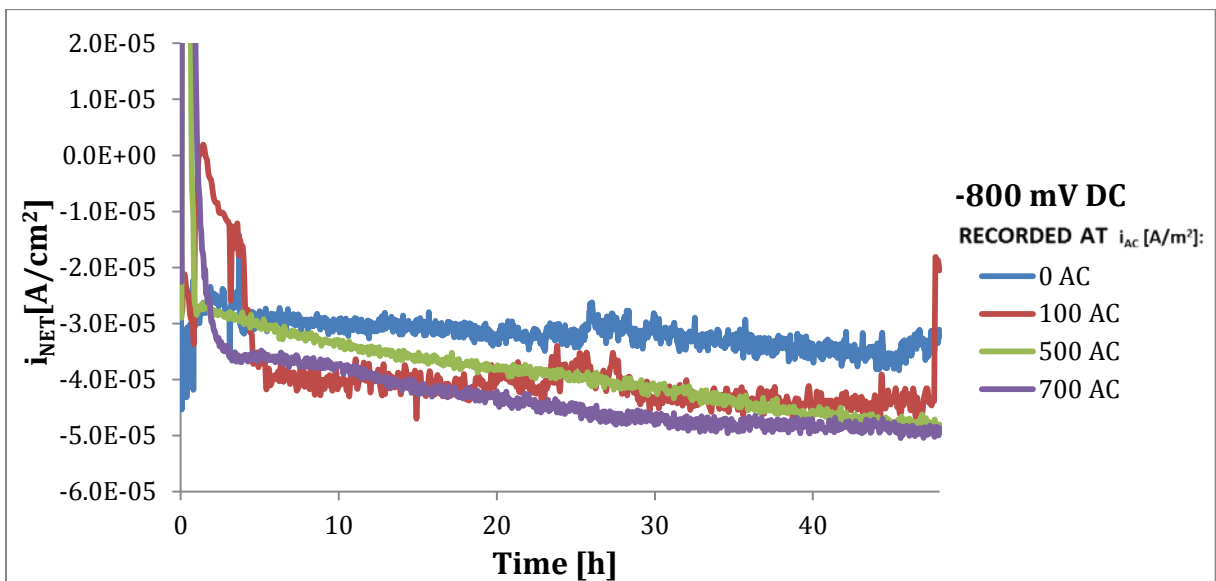
Figure 31: The recorded current density response for experiments on X65 under cathodic potentiostatic polarization at -800 mV as a function of time when samples have been tested for 48 hours for increasing AC densities.
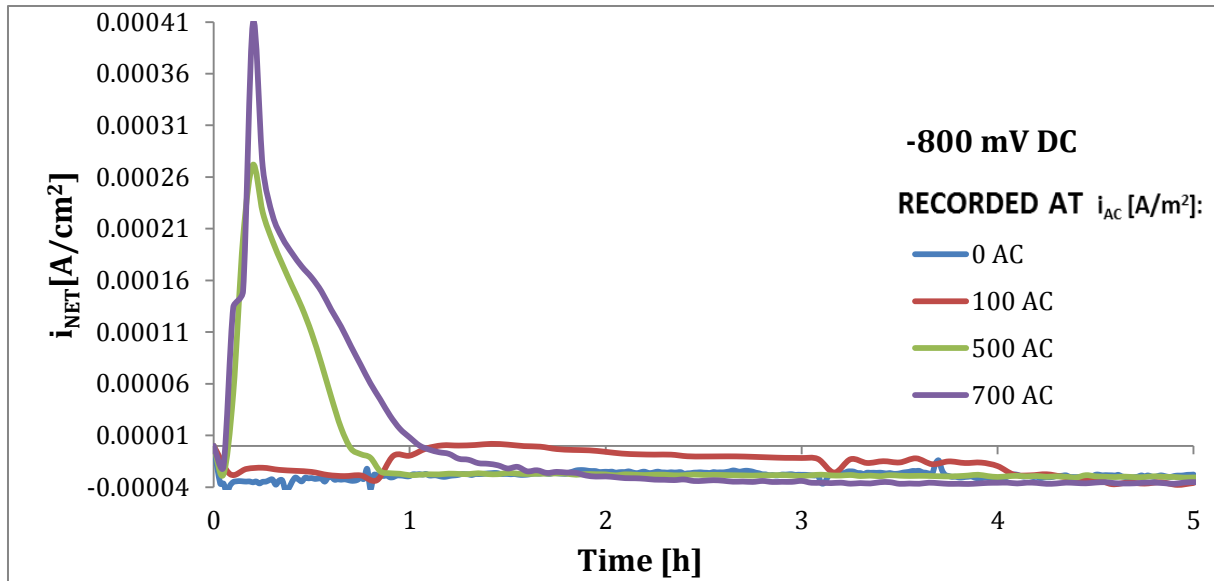
Figure 32: The recorded current density response for experiments on X65 under cathodic potentiostatic polarization at -800 mV as a function of time when samples have been tested for 48 hours for increasing AC densities. First five hours of the experiment can be seen in a detailed manner.
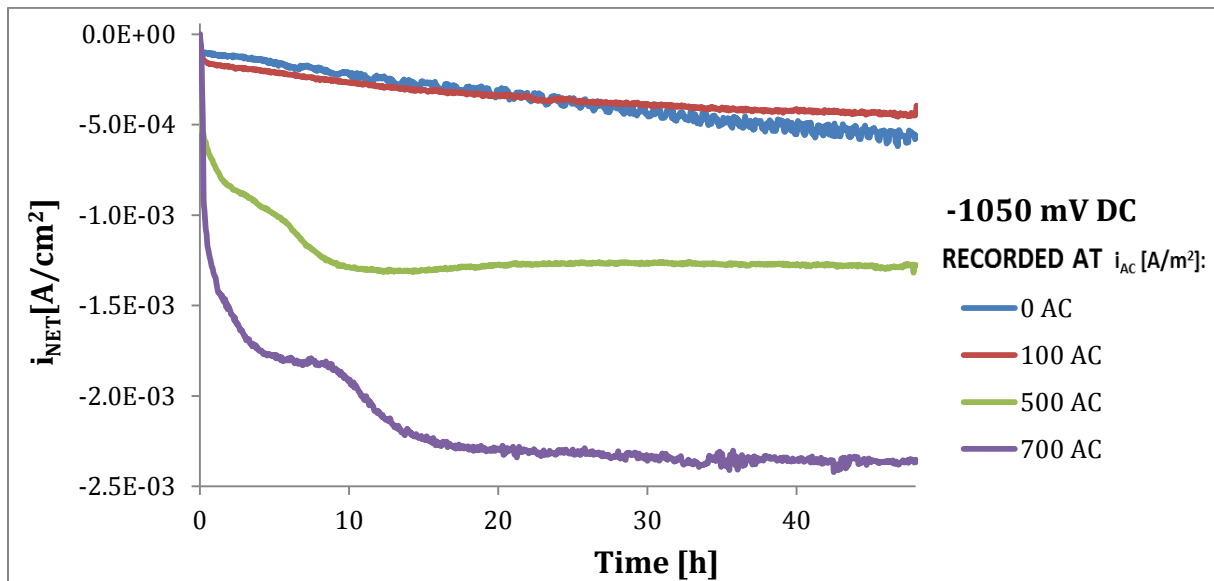
Figure 33: The recorded current density response for experiments on X65 under cathodic potentiostatic polarization at -1050 mV as a function of time when samples have been tested for 48 hours for increasing AC densities.

Polarization curves recorded for X65 were in addition recorded and are reported in Appendix D.2.

The V_{AC} values recorded during the experiments were seen to increase with increased AC densities and all recorded values gained a maximum value within the first 15 hours of the experiment. As can be seen in Figure 34, the highest V_{AC} measured for the 316L experiments was 2.182, corresponding to experiments when 1000 A/m^2 AC were applied on samples polarized at -800 mV.
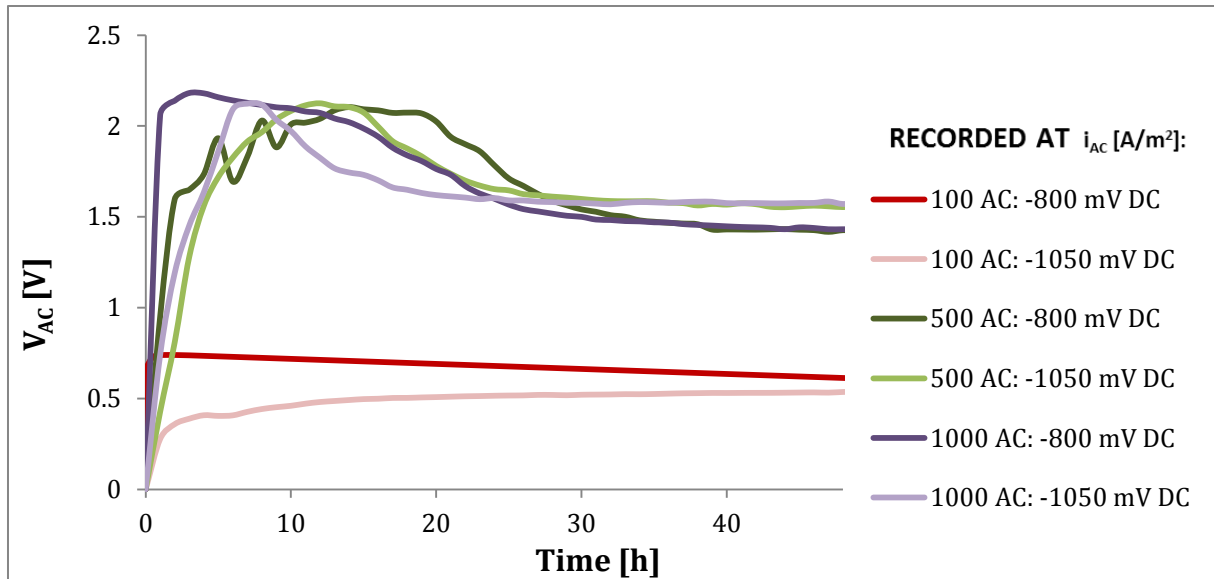
Figure 34: Recorded V$_{AC}$ for experiments on 316L under cathodic potentiostatic polarization at -800 mV and -1050 mV as a function of time when samples have been tested for 72 hours for increasing AC densities.

Similar recording of V_{AC} during experiments on X65 show that values were lower when compared with those recorded for 316L. As can be seen in Figure 35 the highest V_{AC} measured for X65 experiments was 1.5 V_{AC} and in addition this corresponds to an applied AC density of 500 A/m ^{2} on samples polarized at -800 mV. However after a stabilization time of 30 hours, values for 316L have approached those for X65.
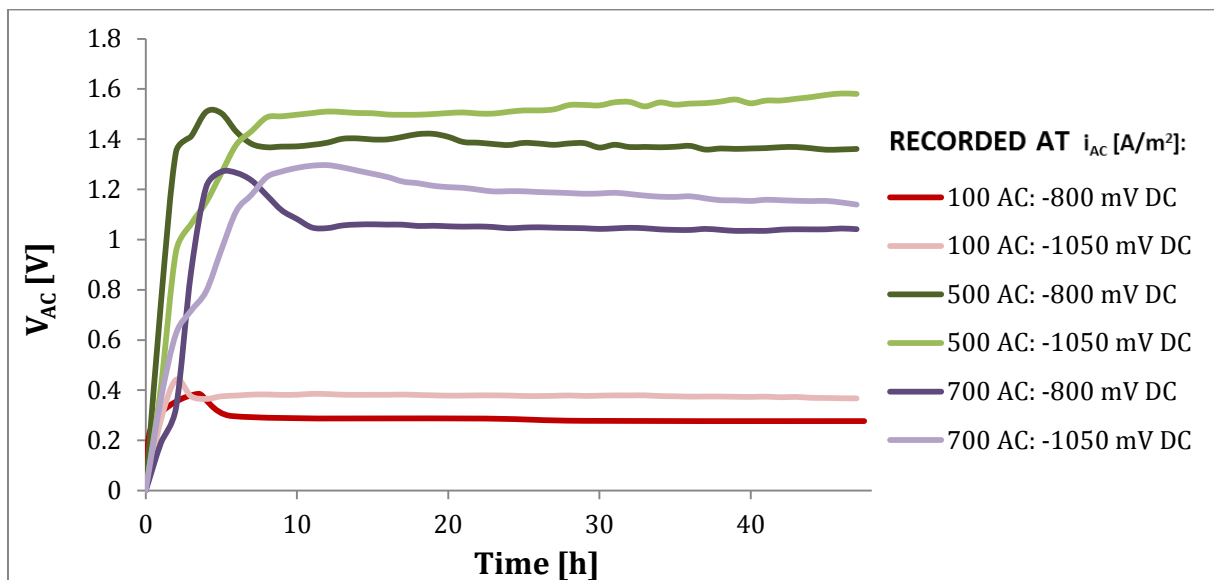
Figure 35 Recorded V_{AC} for experiments on X65 under cathodic potentiostatic polarization at -800 mV and -1050 mV as a function of time when samples have been tested for 72 hours for increasing AC densities.

4.1.2 Weight loss measurements

The measured weight losses at the end of experiments enabled calculation of corrosion current densities based on the total time of exposure; see Figure 36 for average results for 316L and Figure 37 for average results for X65, both plotted with their respective spread. The plots contain as well information about results from similar experiments conducted the autumn of 2012 during the project work, where the behavior of 316L and X65 was investigated at the open circuit potential (E_{OC}).

Additional information regarding calculations is to be found in Appendix A and particular information about weight loss measurements for 316L and X65 parallels, is to be found in Appendix C.1 and D.1 respectively.
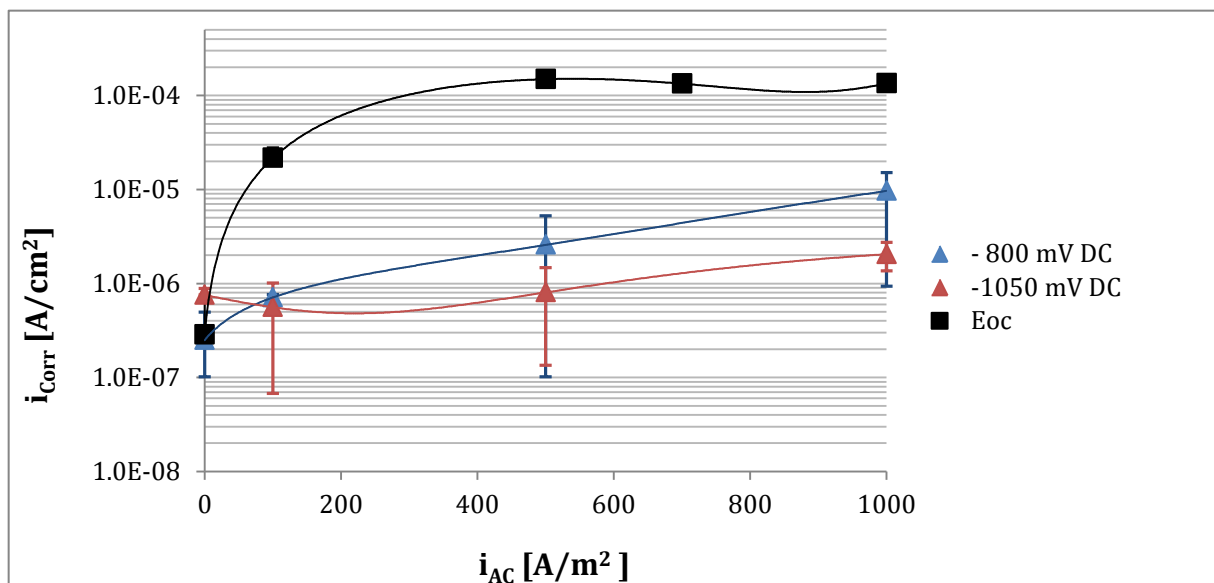
Figure 36: Corrosion current densities for 316L as calculated from weight losses when increasing AC densities are applied. Results from experiments under cathodic potentiostatic polarization are plotted along with results from experiments at E_{OC} [48]. All values are plotted with the respective spread.

Referring to the values obtained, it can be seen that for 316L an increase in AC density caused an increase in weight loss and the loss was higher at the least cathodic potential, -800 mV.

For values obtained at E_{OC}, corrosion stabilized when AC densities above 500 A/m^2 were applied. When polarizing cathodically this trend was not seen neither at -800mV nor -1050 mV.
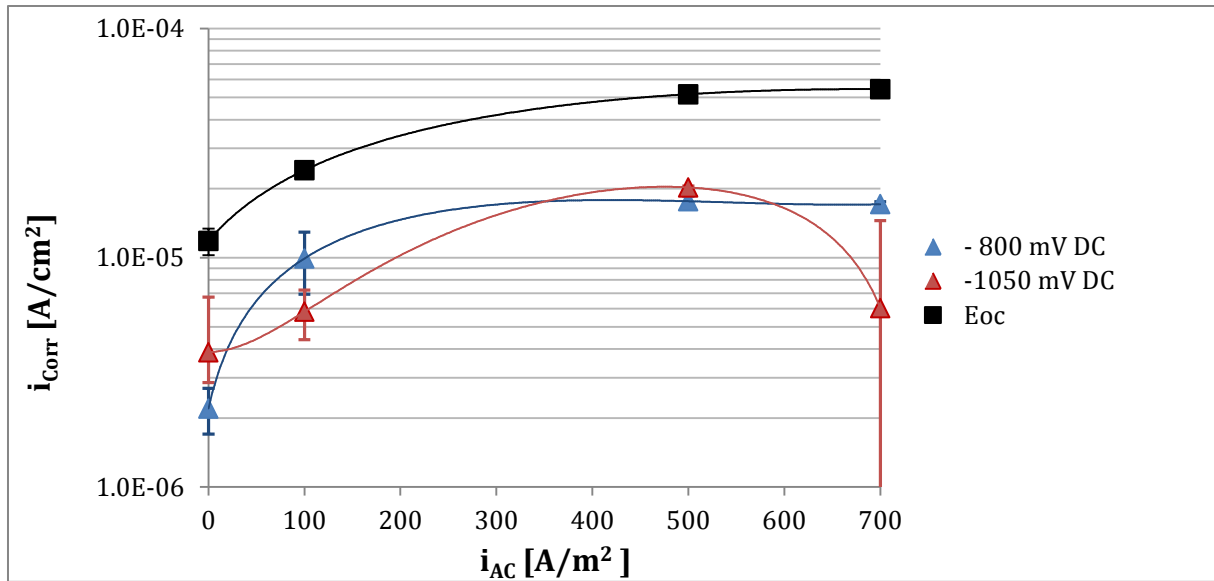
Figure 37: Corrosion current densities with error bars for X65 as calculated from weight losses when increasing AC densities are applied. Results from experiments under cathodic potentiostatic polarization are plotted along with results from experiments at E_{OC} [48]. All values are plotted with the respective spread

Corrosion current densities measured for X65 stabilized when polarized potentiostatically at -800 mV, whereas at -1050 mV corrosion current densities first increased before these again decreased.

At -1050 mV and 500 A/m^2 AC the weight loss appeared to be lower than for similar experiments at 700 A/m^2 AC. However, the spread for the achieved results at 700 A/m^2 AC was found to be high.

4.1.3   Surface morphology

Photos captured of specimens prior to removal of corrosion products and after such removal are used in combination with micrographs from a SEM study in order to investigate the morphology changes as a function of applied DC potentials and AC densities.

Figure 38 and Figure 39 show how the surfaces of 316L were increasingly affected when increasing AC densities were applied at -800 mV and -1050 mV respectively.

When samples were retrieved from cells, the ones tested from 500 A/m^2 AC and higher smelled faintly of chlorine. During the tests some gas evolution in form of transparent bubbles was seen at these AC densities to evolve over the surfaces, especially around corners and edges.

At these AC densities some blistering was found on the upper layers of the coating as can be observed from the photos.
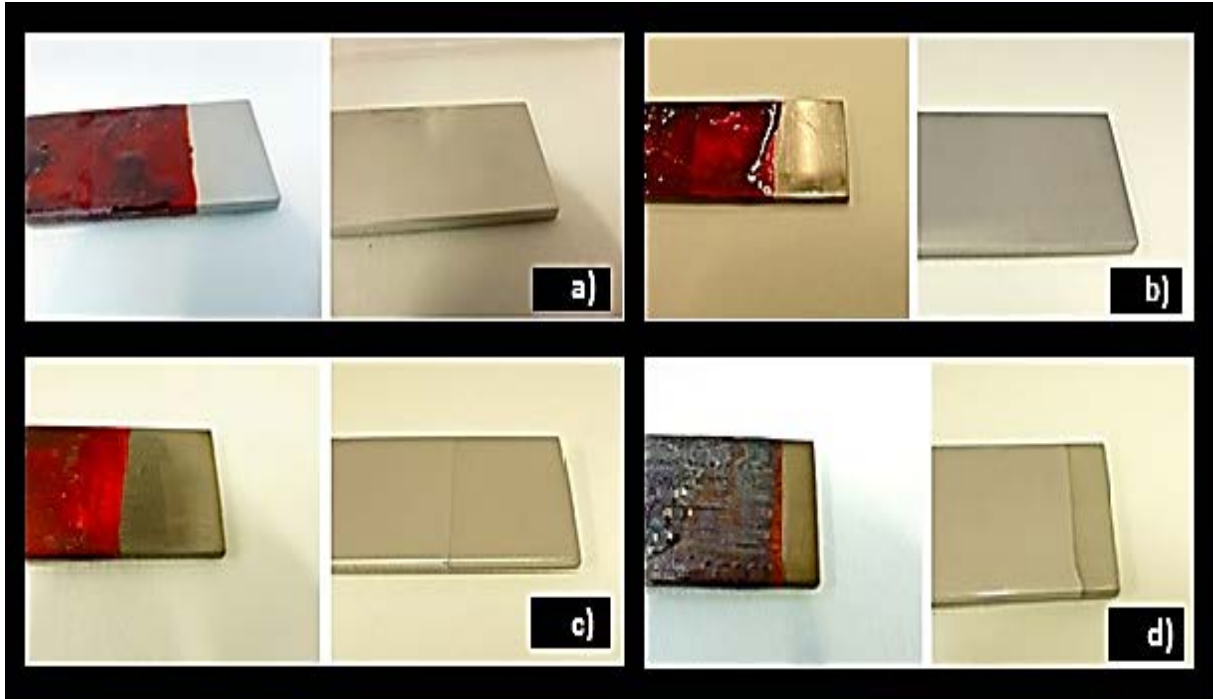
Figure 38: Photos of 316L sample surfaces tested at -800 mV at an applied density of a) 0 A/m^2 AC b) 100 A/m^2 AC c) 500 A/m^2 AC and d) 1000 A/m^2 AC .
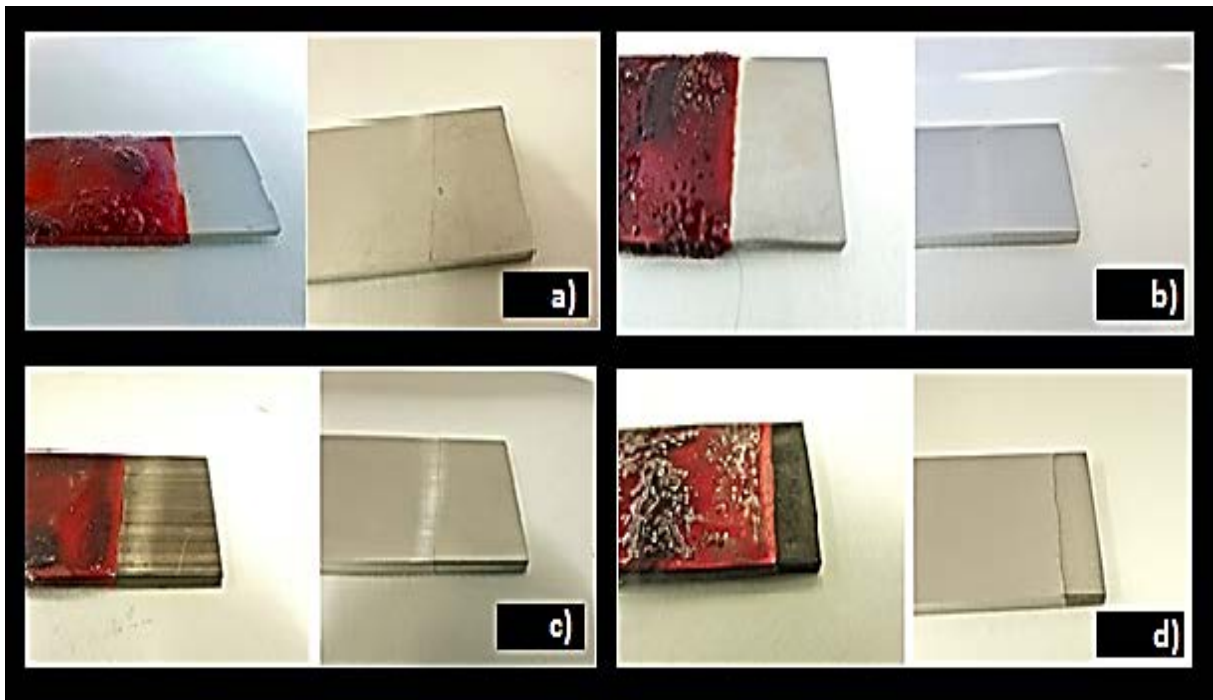
Figure 39: Photos of 316L sample surfaces tested at -1050 mV at an applied density of a) 0 A/m^2 AC b) 100 A/m^2 AC c) 500 A/m^2 AC and d) 1000 A/m^2 AC .

Increasingly dark layers of film were found on 316L surfaces when samples were taken out from test cells. Most of the products were easily removed when immersed in solutions for such removal. But not everything came off, as it is possible to deduce from the photos in Figure 38-Figure 39.

SEM photomicrographs were captured for all samples at magnifications of M=100X and M=500X with working distances between of 5-10 mm and an accelerating voltage of E_0=15Kv. SEM micrographs taken at 100X magnification of 316L samples tested at 100 A/m^2 AC and 1000 A/m^2 AC are seen in Figure 40 - Figure 41. Micrographs taken at 500 X magnification are provided in Appendix C.3. When samples were investigated in SEM, it was noted that:

1) Pits were found to become deeper with increased AC densities. Also numbers of pits were found to increase.

2) It was confirmed that a layer of film had not been successfully removed on 316L, for samples tested with applied AC. It was also discovered that some of what seemed to be a non-soluble film was actually substantially dense pitting, which gave the surface the greyish look when studied with the naked eye.

3) Grain boundary corrosion was identified on a 316L sample tested at the highest cathodic potential and AC density, i.e. at -1050 mv and 1000 A/m^2 AC.
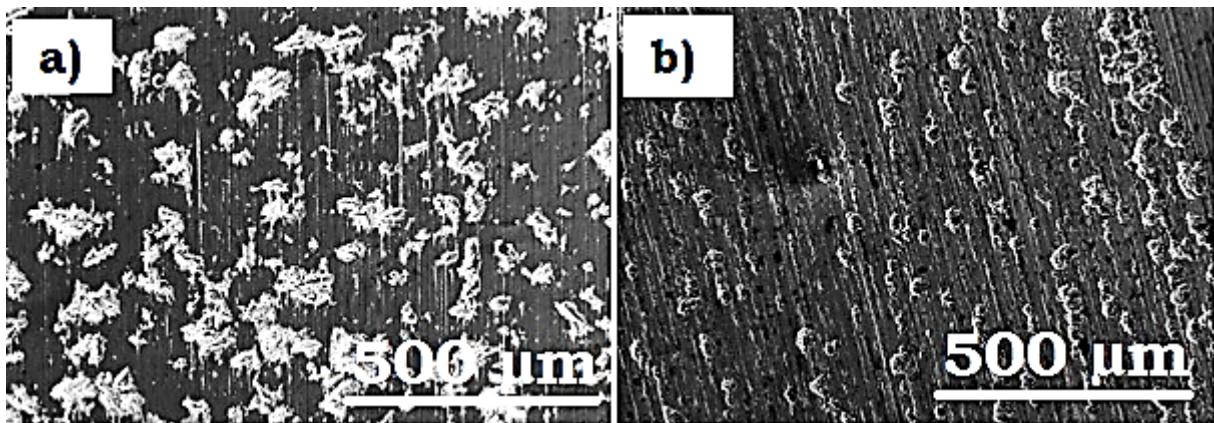
Figure 40: SEM micrographs of surface damages on samples tested at -800 mV DC (SCE) and an applied AC density of a)100 A/m^2 and b)1000 A/m^2 seen at 100X magnification.
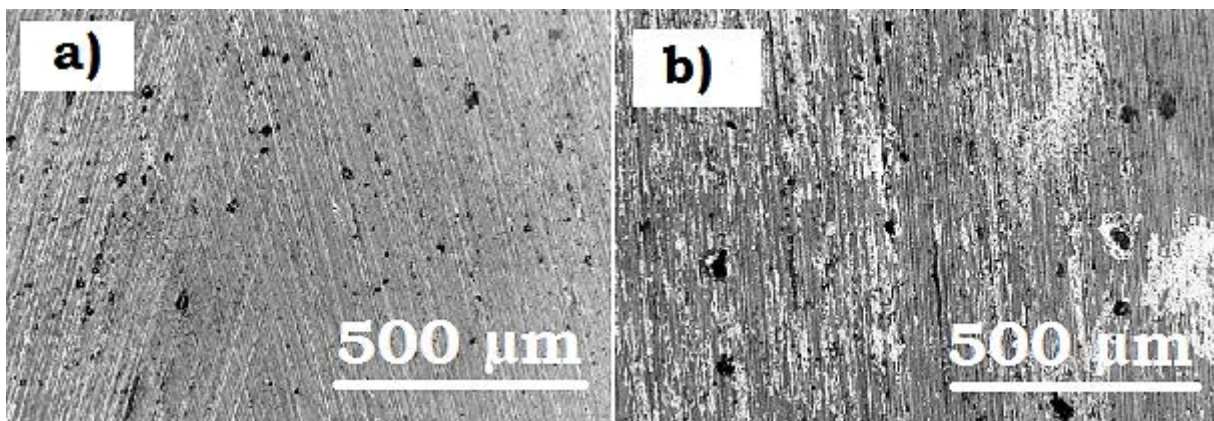
Figure 41: SEM micrographs of surface damages on samples tested at -1050 mV and an applied AC density of a)100 A/m^2 and b)1000 A/m^2 seen at 100X magnification.

It is seen that pitting both in depth and number increased when increasing densities were applied. At 1000 A/m^2 AC grain boundary corrosion was found close to crevices on a sample tested at and -1050 mV, see Figure 42.
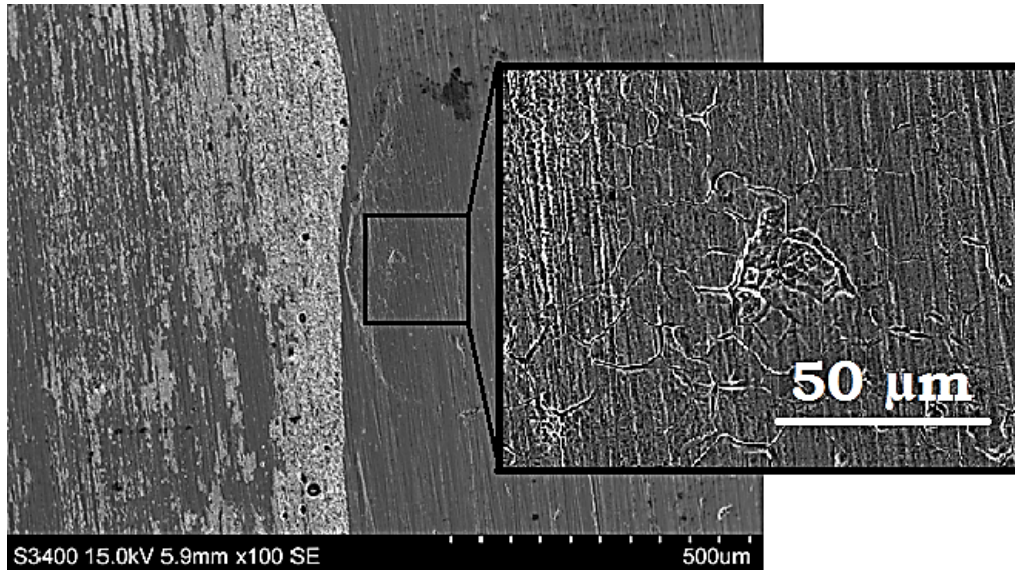
Figure 42: Grain boundary corrosion identified on a sample of 316L type of steel tested at -1050 mV and 1000 A/m^2 AC.

An EDS analysis was performed in order to study the chemical composition of the non-soluble layers of film identified on samples of 316L. These films which were non-soluble in the used solutions for corrosion product removal used on 316L (warm, diluted HNO$_3$), were greyish-black in color in room-light and turned up as white spots when investigated in SEM.

Studies in SEM and EDS indicated that these layers had formed on placed identified as heavily corroded – close to areas where pits and creviced had developed on the surfaces. The SEM micrographs in Figure 43 shows how the film deposited on pitted areas for samples tested at 100 and 1000 A/m^2 AC when polarizing cathodically at -800 mV.
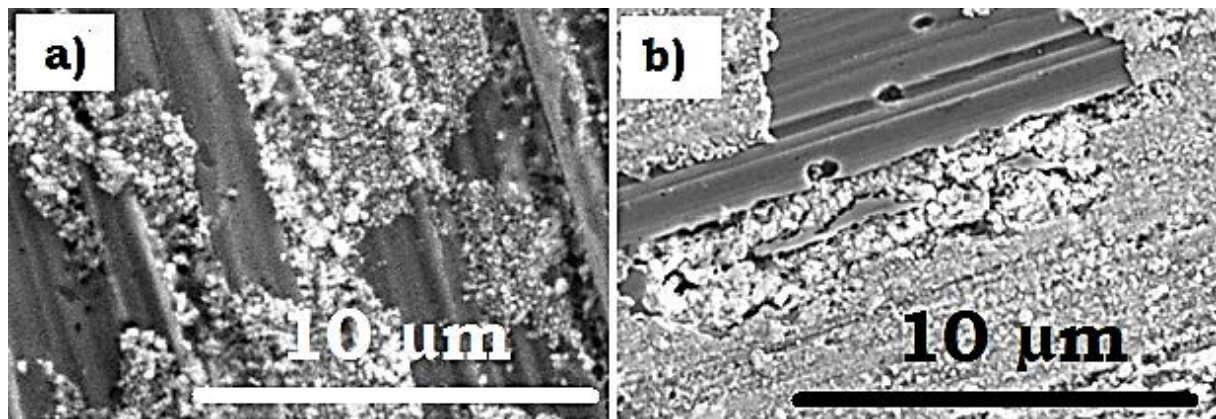
Figure 43: SEM micrograph of the film layer on samples tested at -800 mV and a) 100 A/m^2 AC b) 1000 A/m^2 AC. (5.5kX)

The results from the EDS analysis of surfaces on 316L samples tested at 100, 500 and 1000 A/m^2 covered with and without film are reported in Appendix C.3 and C.4. The EDS analysis revealed that the film consisted mainly of platinum (Pt).

Photos of X65 in Figure 44- Figure 45 show how the surfaces turned increasingly darker in color when increasing AC densities were applied. No layers of non-soluble films similar to those found on 316L were identified on X65.
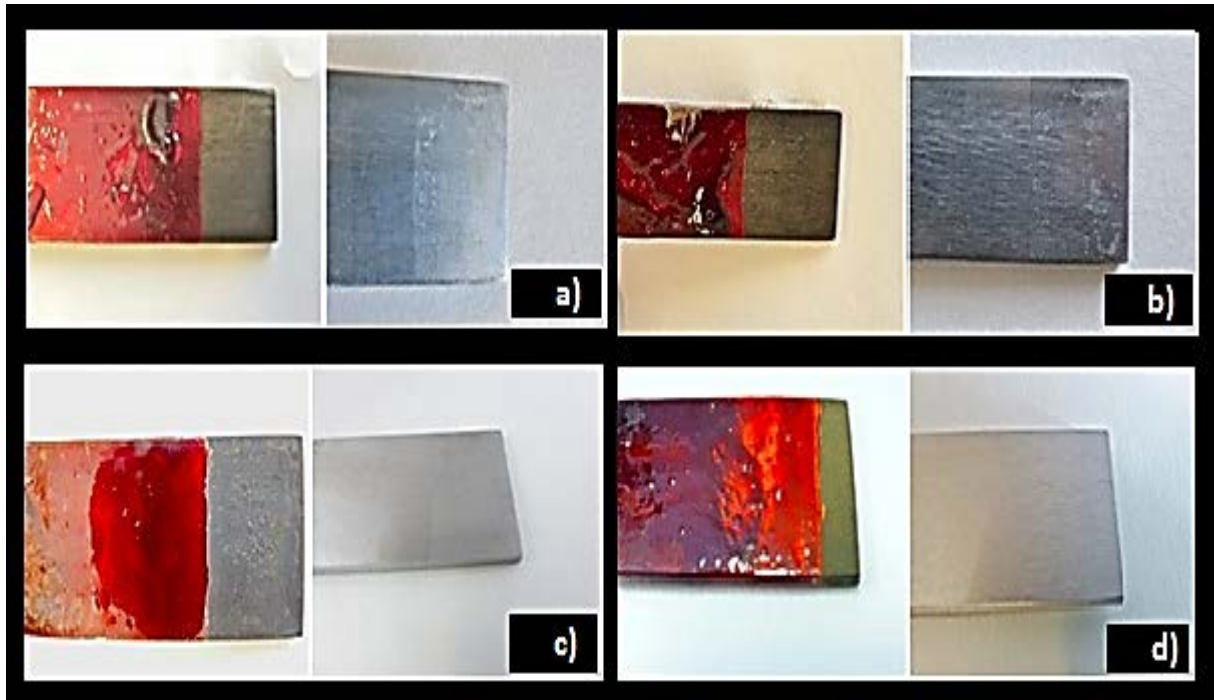
Figure 44: Photos of X65 sample surfaces tested at -800 mV at an applied density of a) 0 A/m^2 AC b) 100 A/m^2 AC c) 500 A/m^2 AC and d) 1000 A/m^2 AC .
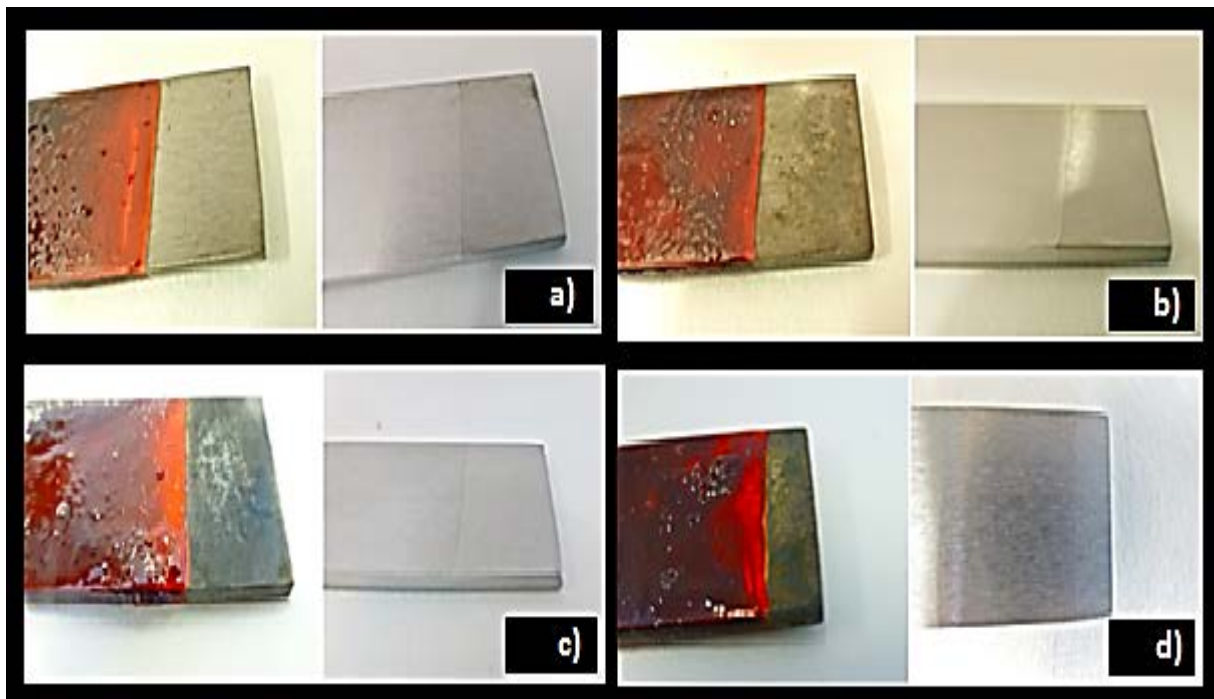
Figure 45: Photos of X65 sample surfaces tested at -800 mV at an applied density of a) 0 A/m^2 AC b) 100 A/m^2 AC c) 500 A/m^2 AC and d) 700 A/m^2 AC .

When studied in SEM, micrographs of surfaces confirmed the visual observations, as it can be seen from Figure 46-Figure 47. The surfaces were covered with a higher number of pits which increased in depth with increasing AC densities. As can be seen from the micrographs

taken at 500X magnification provided in Appendix D.3, at the highest AC densities applied the surfaces were uniformly covered with pits.
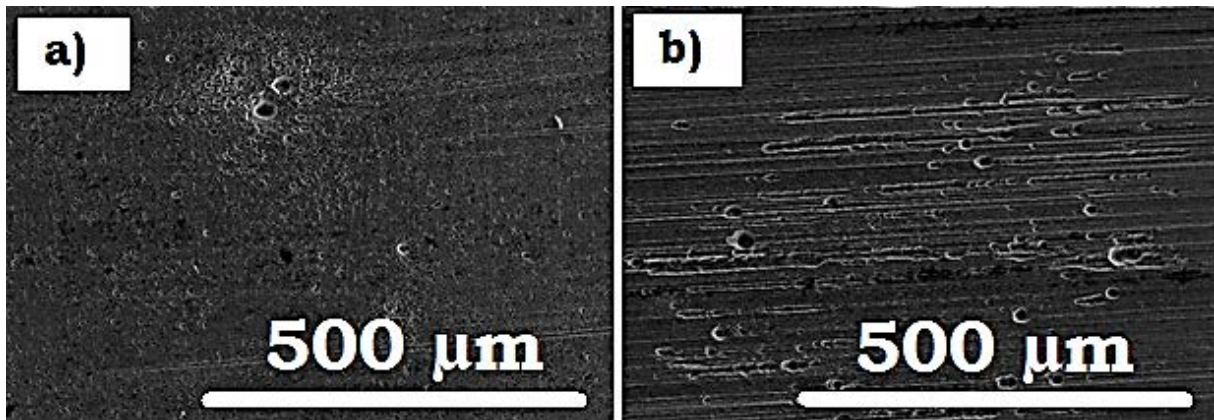
Figure 46: SEM micrographs of surface damages on samples tested at -800 mV and an applied AC density of a)100 A/m^2 and b)700 A/m^2 seen at 100X magnification.
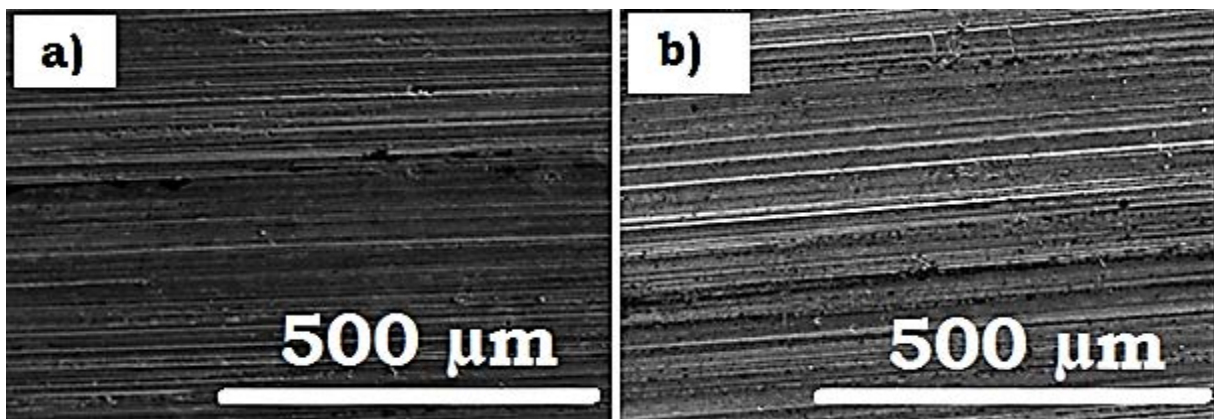
Figure 47: SEM micrographs of surface damages on samples tested at -800 mV and an applied AC density of a)100 A/m^2 and b)700 A/m^2 seen at 100X magnification.

4.2   The effect of AC on the anodic behavior of stainless steel

Experiments were performed on 25Cr SDSS with a duration of 3 days (72 hours). Experiments mapped the open circuit potential (E_{OC}) at AC densities of 0, 100, 500 and 1000 A/m^2 before anodic polarization tests were conducted under passive conditions.

4.2.1   Open circuit measurements

The time dependence of the open circuit potential (E_{OC}) on the applied amount of AC density was examined over a period of 72 hours as shown in Figure 48. At 100 A/m^2 AC the time needed to reach a stable E_{OC} was 10 hours. For higher densities a similar stabilization was not observed as the potential oscillated between positive and negative potentials. E_{OC} shifted by approximately 227 mV in the positive direction when 100 A/m^2 AC was applied relative to the recorded E_{OC} when no AC was applied, but shifted in the negative direction when higher AC densities were applied.
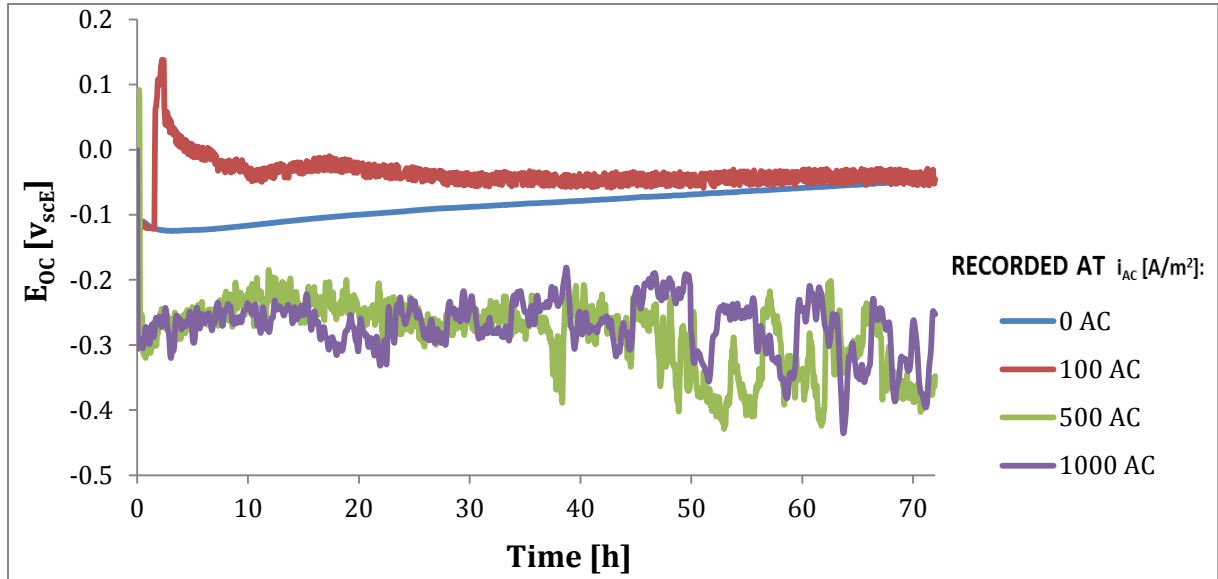
Figure 48: The time dependence of the open circuit potential (OCP) when measured on 25Cr for AC densities from 0-1000 A/m^2 AC in 3.5 wt% NaCl during 72 hours of testing.

4.2.2 Polarization behavior

Polarization scans at 0.147 mV/s were recorded at 0,100, 500 and 1000 A/m^2 AC and the plots resulted from the scanning are presented in Figure 49.
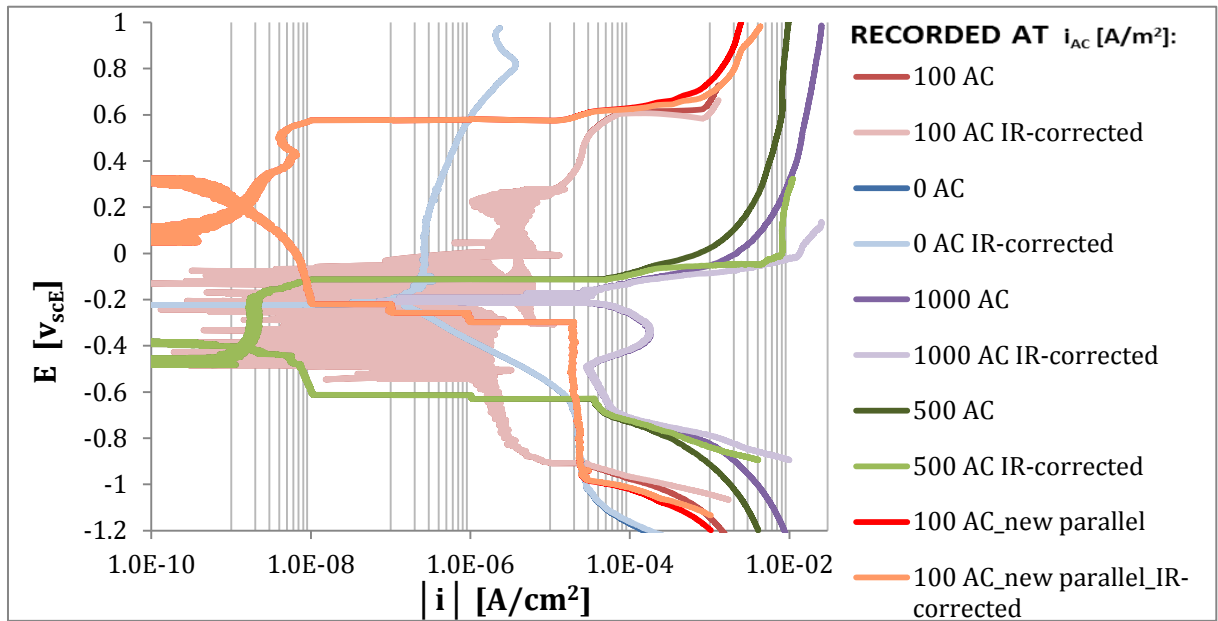
Figure 49: Polarization curves recorded at a sweep rate of 0.167 mV/sec for AC densities from 0 to 1000 A/m^2 on stagnant electrodes of 25Cr immersed in 3.5 wt% NaCl for 72 hours.

The curves, when plotted, were corrected for the potential drop due to resistance in the electrolyte, R_s. Information about resistances and corrosion parameters deduced from the curves is to be found in Appendix E.2.

The mass transport limited oxygen reaction i_{O2_lim} was determined graphically from the curves to be $3*10^{-5}$ A/cm^2. The pitting potential was found to be 600 mV/SCE at 0 and 100 A/m^2 AC, while the passive region was found to lie between -100 mV and +200 mV. For higher AC

densities the passive region disappeared. The rate of the hydrogen reaction was seen to increase with increased AC while the mass transport limited oxygen reaction was not seen to increase. As can be noted, two parallels were performed at 100 A/m^2 AC. The second parallel depicted in orange, was seen to exhibit both a lower passive current density and a more positive corrosion potential, while the pitting potential was the same as for the first parallel.

Based on the findings from E_{OC} measurements and polarization curves, experiments were decided to be performed with 0 and 100 A/m^2 AC at +100 mV and +200 mV. Four distinct programs were designed to ensure passive conditions, see Table 8.

Table 8: The experimental procedure for the anodic polarization tests of 25Cr SSDS.

Experiment	*Polarization program*
Test 1 at 0 A/m^2 AC	Potentiodynamic ramping up to +100 mV during 2 hours, then potentiostatic polarization at this potential for 70 hours. (72 hours in total)
Test 1 at 100 A/m^2 AC	Potentiodynamic ramping up to +100 mV during 2 hours, then potentiostatic polarization at this potential for 70 hours. (72 hours in total) AC applied after 17 hours.
Test 2 at 100 A/m^2 AC	Potentiodynamic ramping up to +200 mV during 2 hours, then potentiostatic polarization at this potential for 70 hours. (72 hours in total) AC applied after 17 hours.
Test 3 at 100 A/m^2 AC	Potentiodynamic ramping up to +100 mV during 2 hours, then potentiostatic polarization at this potential for 70 hours. (72 hours in total) AC applied from the start of the experiment.

During the experiments the DC current response was recorded as well as the AC cell potential response at the specific applied AC density. Two parallels were carried out at 0AC, but data for one of them was erased due to power failure. However, weight loss data is provided for this parallel as well. Key results from these recordings are based on only one parallel and are summarized in

Table 9. The current response data provided in the table is given as:

$i_{NET}\_t = 0h$ The start value measured at once the sample was inserted into the test cell.

$\overline{i_{NET}}\_t = (0-2)h$ The average current response for the first two hours of the experiment when the ramping of potential in anodic direction was finalized

$\overline{i_{NET}}\_t = (10-17)h$ The average current response between hour 10 and hour 16 of the experiment

$\overline{i_{NET}}\_t = (60-72)h$ The average current response at the end of the experiment between hour 60 and hour 72 of the experiment, when the effect of applied AC may have reached a steady-state.

Values are reported as averaged since current responses were found to oscillate and choosing one of the values would provide incomplete information about the current response at the specific time.

Table 9: Key results from anodic polarization experiments in 3.5 wt% NaCl on 25Cr.Test lasted 72 hours.

i_{AC} [A/m^2]	$\overline{V}_{AC}$ [V]	$i_{NET}\_t=0h$ [A/cm^2]	$\overline{i_{NET}}\_t=(0-2)h$ [A/cm^2]	$\overline{i_{NET}}\_t=(10-17)h$ [A/cm^2]	$\overline{i_{NET}}\_t=(60-72)h$ [A/cm^2]
0	-	5.78E-08	5.47E-08	4.29E-09	4.36E-10
100	0.771	-1.59E-08	-1.55E-09	1.83E-09	-2.44E-07
100	0.796	-2.45E-07	-3.97E-08	1.34E-08	-7.58E-08
100*	0.755	1.38E-06	-7.11E-06	-8.50E-06	9.26E-06

) The AC density was applied from the start

From the data provided in the table, it is worth noting:

1) At the start of experiments a positive current response was measured for two of the samples, whereas a negative current response was measured for the two other samples.

2) When AC was applied, the current response turned negative, no matter whether it was positive or negative to begin with.

3) The sample tested with no applied AC started with a positive current response which in time decreased.

The DC current response has been plotted as a function of time, as can be seen in Figure 50-Figure 51 for the sample tested at 0 A/m^2 AC and in Figure 52-Figure 57 for samples tested at 100 A/m^2 AC.

It is to be noted the use of logarithmic time scale where this has occurred. All mV reported are related to the DC potential applied.
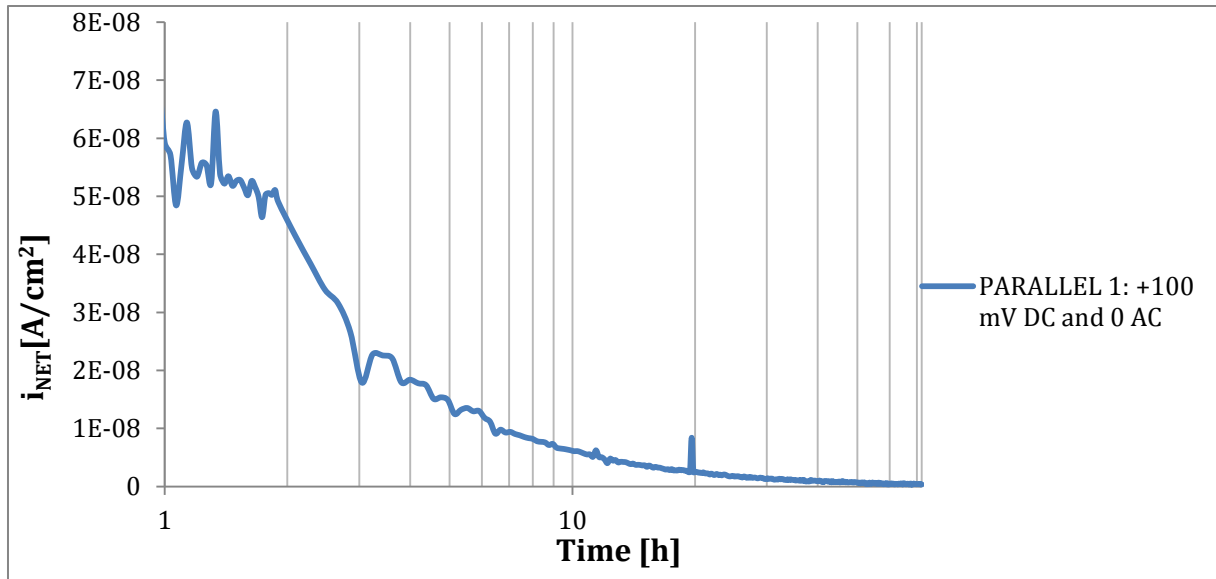
Figure 50: The recorded current density response for a 25Cr sample tested during 72 hours at an applied AC density of 0 A/m². The first two hours are potentiodynamic ramping of the DC potential with a sweep rate of 0.015 mV/s up to +100 mV. The last 70 hours are potentiostatic polarization at +100 mV.
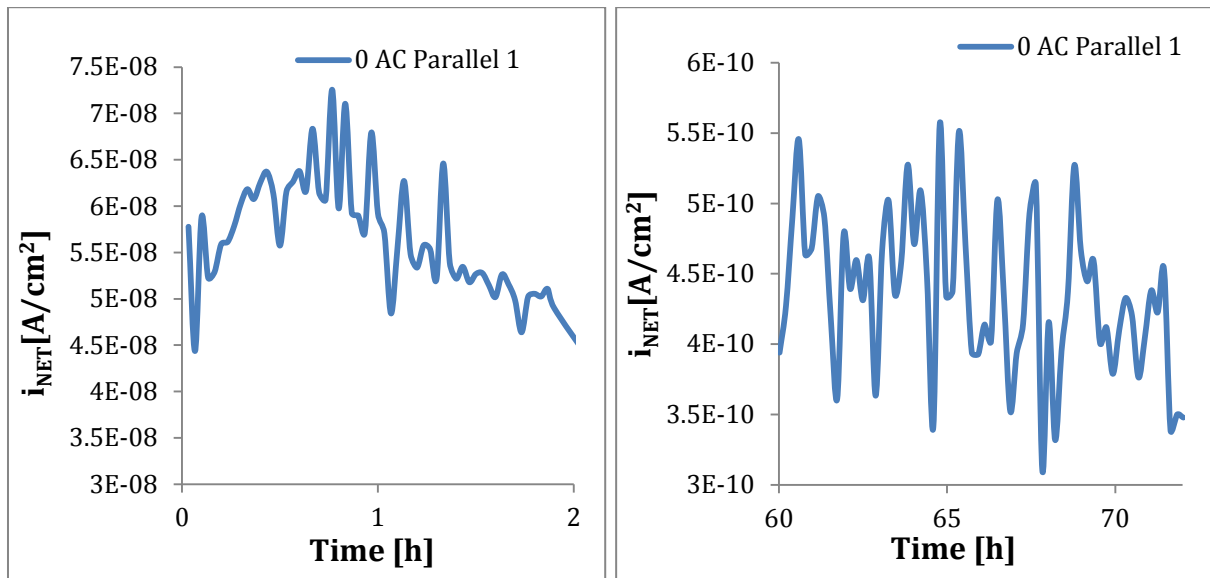
Figure 51: The current response <u>left)</u> at the start of the experiment during the potentiodynamic ramping of DC potential up to +100 mV with a sweep rate of 0.015 mV/s and <u>right)</u> during the last 12 hours of potentiostatic polarization at +100 mV.

From plots for the parallel tested at 0 A/m² AC, it is to be observed that the current response was positive throughout the whole experiment, but decreasing.

All current response curves plotted for samples tested at 100 A/m² AC are depicted in Figure 52.

51
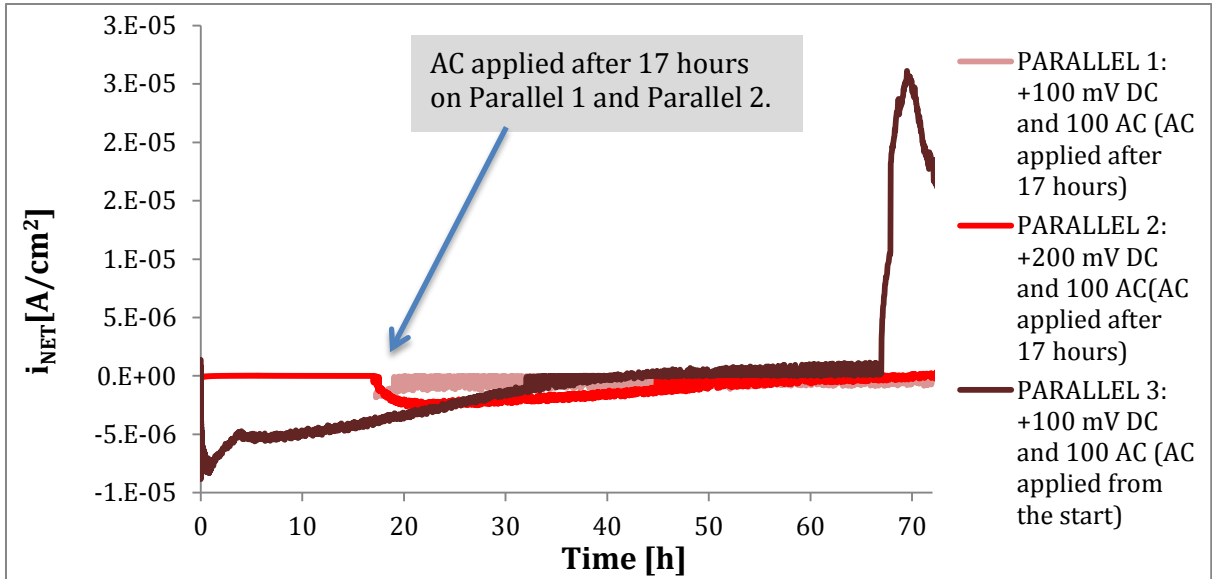
Figure 52: The recorded current density responses for 25Cr samples tested during 72 hours at an applied AC density of 100 A/m². For Parallel 1 the first two hours are potentiodynamic ramping of the DC potential with a sweep rate of 0.015 up to +100 mV. The last 70 hours are potentiostatic polarization at +100 mV. Parallel 2 is similar in procedure but the DC is +200 mV. For Parallel 3 the AC is applied from the start and the DC is +100 mV applied by a similar procedure as for Parallel 1 and 2.

As can be seen from Figure 52 and the following plots, the surfaces of Parallel 1 and 2 (tested at 100 A/m² AC applied after 17 hours) started out with a negative current response which developed to a positive current response during the potentiodynamic ramping of potential. When AC was applied the currents became negative.
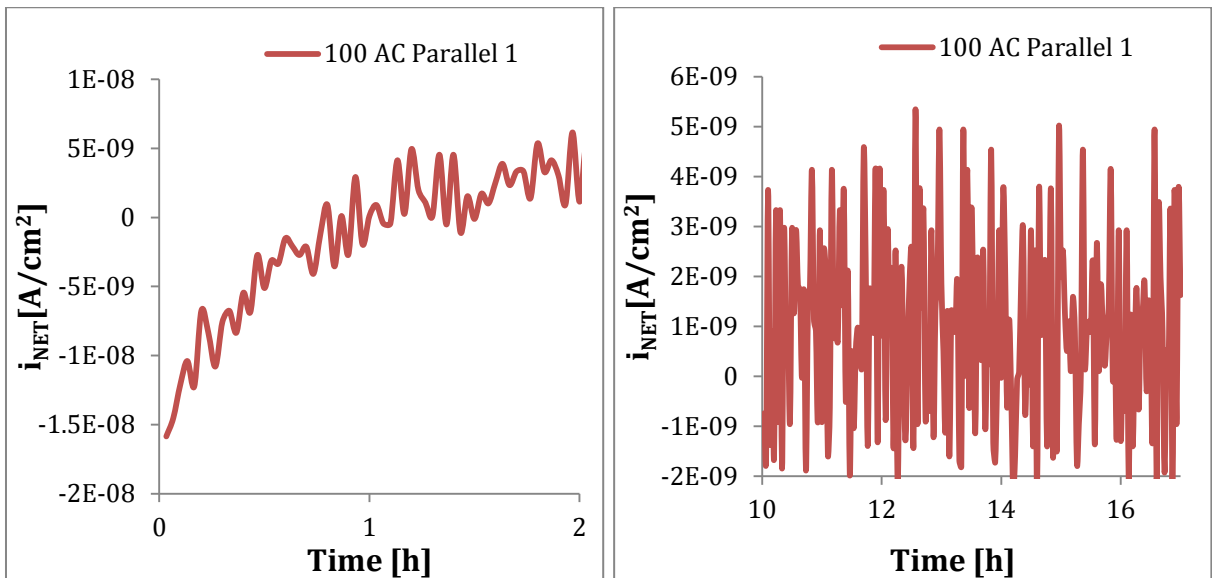
Figure 53: The current response <u>left)</u> at the start of the experiment during the potentiodynamic ramping of the DC potential up to +100 mV and <u>right)</u> before applying AC (after the 17th hour of the experiment) for Parallel 1 tested at 100 A/m² AC.
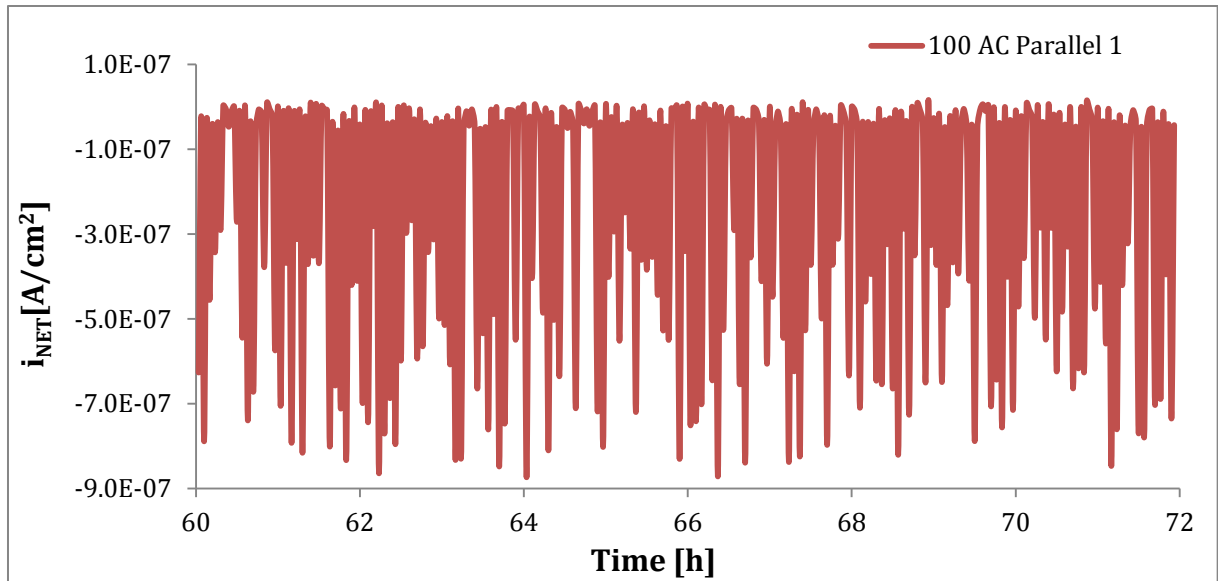
Figure 54: The current response for the last 12 hours of the experiment during the potentiostatic polarization of the sample at +100 mV and 100 A/m² AC (applied after 17 hours) for Parallel 1.

The current response recorded for Parallel 2 tested at +200 mV oscillated after AC was applied, but within a smaller magnitude range when compared with Parallel 1 tested at +100 mV.
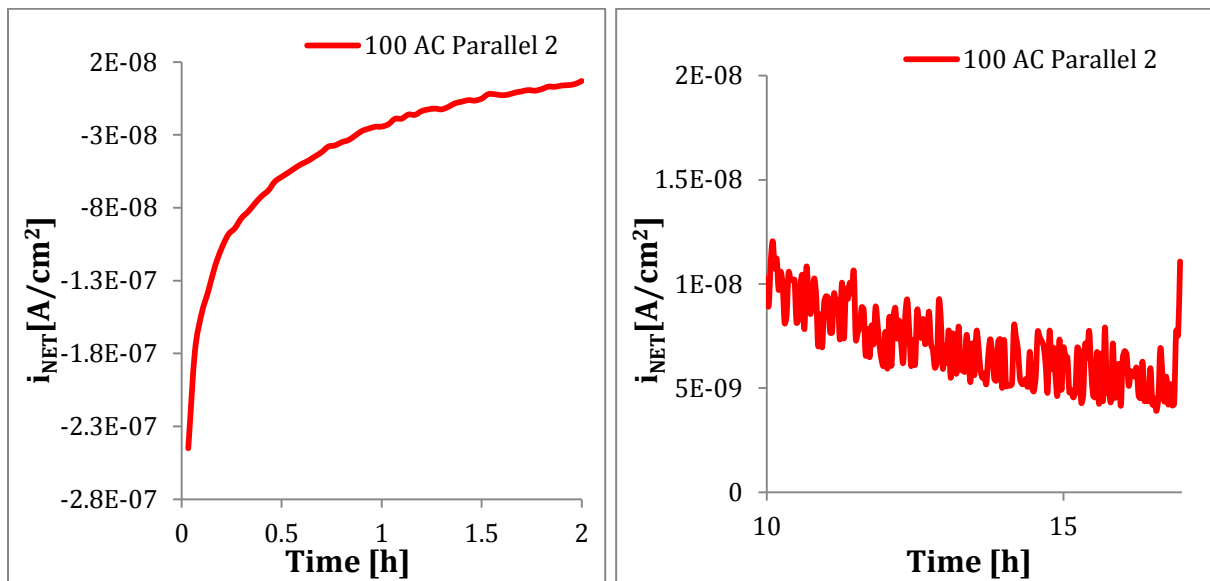
Figure 55: The current response left) at the start of the experiment during the potentiodynamic ramping of the DC potential up to +200 mV and right) before applying AC (after the 17th hour of the experiment) for Parallel 2 tested at 100 A/m² AC.
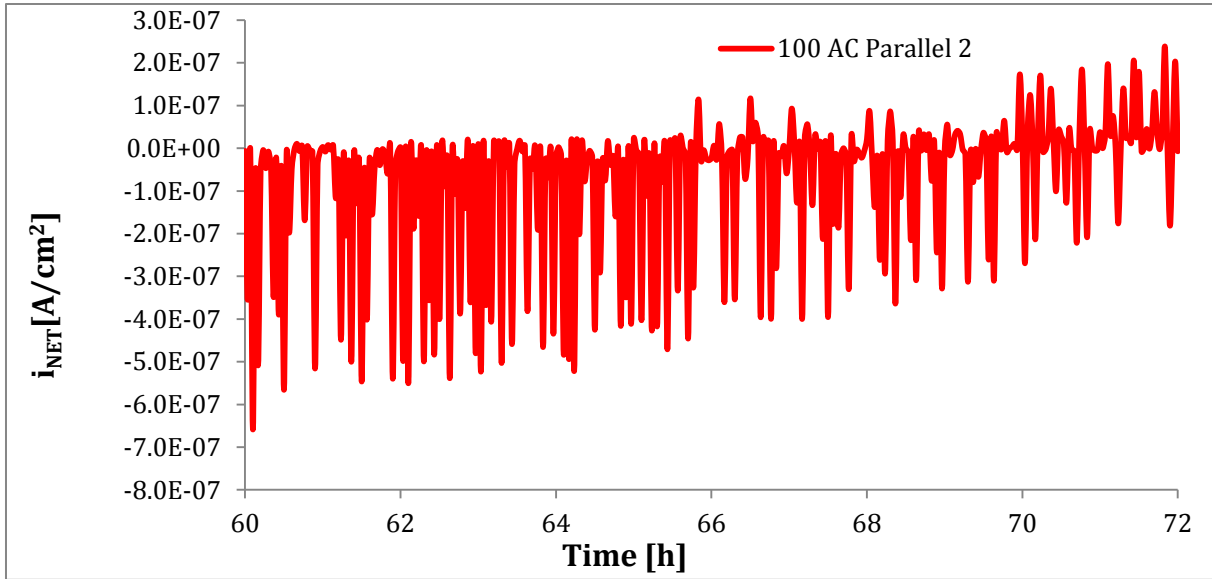
Figure 56: The current response for the last 12 hours of the experiment during the potentiostatic polarization of the sample at +200 mV and 100 A/m^2 AC (applied after 17 hours) for Parallel 2.

For Paralell 3 the current response was initially positive, but at once the VariAC was turned on delivering 100 A/m^2, the currents changed to be negative as can be observed from Figure 57 , until they slowly developed to be positive during the 36th hour of the experiment.
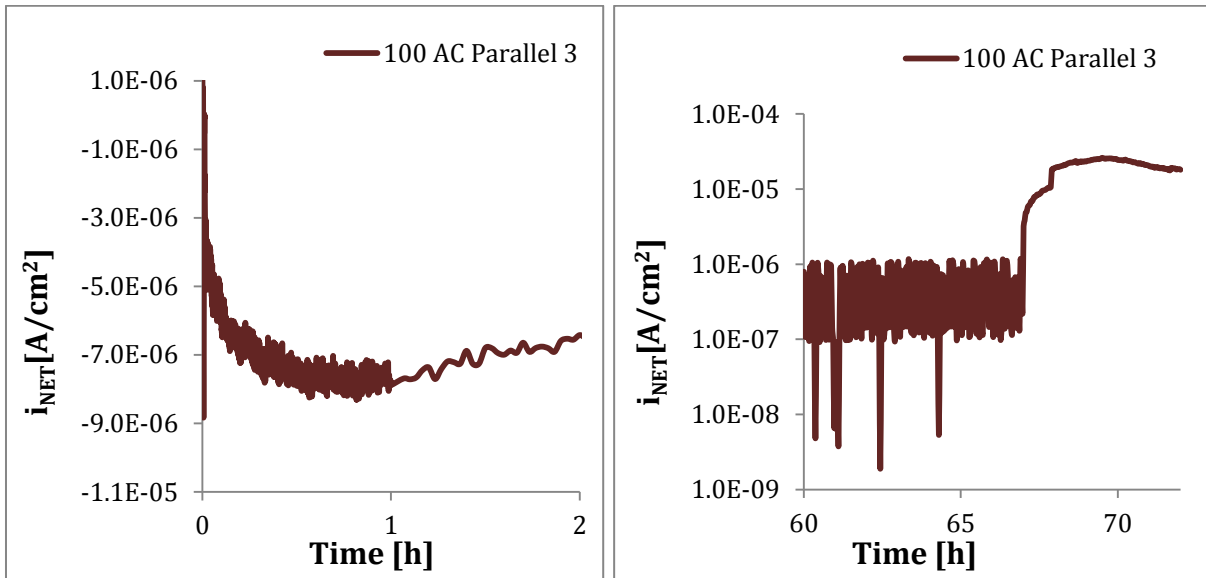
Figure 57: The current response left) at the start of the experiment during the potentiodynamic ramping of the DC potential up to +100 mV and right) for the last 12 hours of the experiment during the potentiostatic polarization of the sample at +100 mV for Parallel 2 where an AC density of 100 A/m^2 was applied from the start.

The AC cell potential, V_{AC} was recorded by a multimeter inserted in parallel with the working electrode and the counter electrode in the AC part of the circuit. Plots of V_{AC} as a function of time can be seen in Figure 58. The V_{AC} for 25Cr gained higher values than seen from experiments on both 316L and X65 when these were tested at an applied AC density of

100A/m^2 under cathodic potentials. The highest $\overline{V}_{AC}$ was measured to 0.796 at 100 A/m^2 AC as can be seen from Table 9, corresponding to Parallel 2 tested at +200 mV DC.
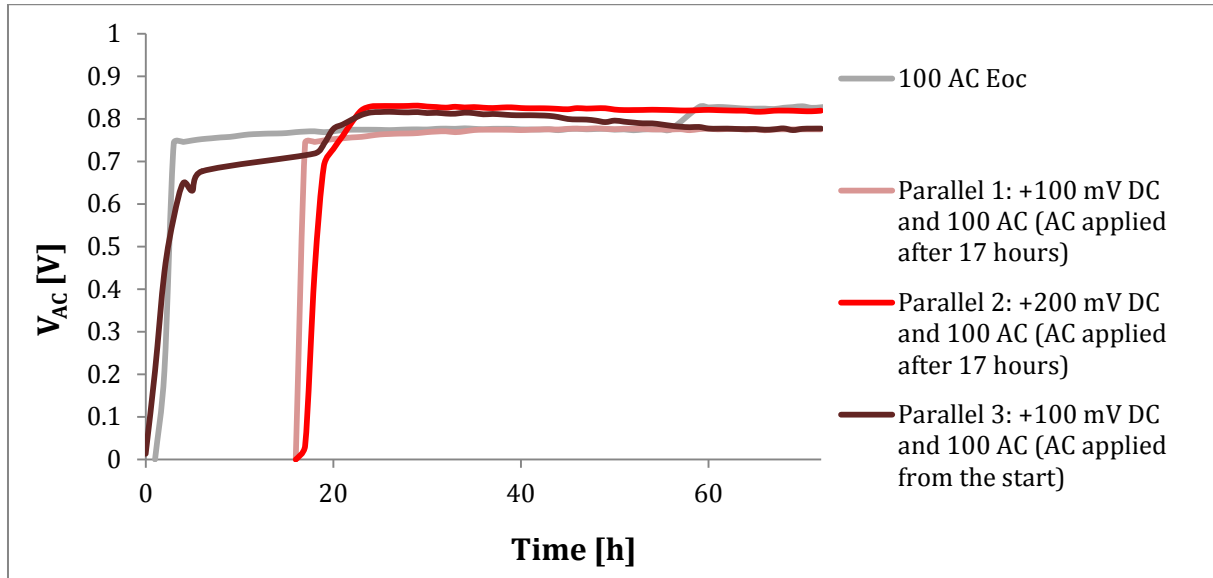
Figure 58: Recorded V_{AC} for experiments on 25Cr when 100 A/m^2 AC were applied on samples tested at *Eoc* and under anodic bias in 3.5 wt% NaCl for 72 hours.

4.2.3 Weight loss measurements

The measured weight losses at the end of experiments enabled calculation of corrosion current densities and corrosion rates (CR) based on the total time of exposure, see Table 10 for results from weight loss measurements for samples tested at different test conditions.

To correct for additional weight losses related to the removal of corrosion products, un-corroded samples were tested as described in ASTM G1-03[70]. It was found that 25Cr remained unaffected. The steel showed no mass loss due to the chemical removal step and all mass losses recorded after experiments for this steel type are therefore actual losses due to corrosion of the material during the experiments.

Table 10: Key results from weight loss measurements for 25Cr.

Sample	V_{DC} [V]	i_{AC} [A/m²]	Δm_{corr} [mg]	$\overline{\triangle m}_{corr}$ [mg]	$i_{corr}{}^{WL}$ [A/cm²]	CR^{WL} [mmy]
Parallel 1	0.1	0	0.192	0.163	4.17E-07	0.005
Parallel 2	0.1	0	0.133		2.84E-07	0.003
Parallel 1	0.1	100[+]	0.867		1.87E-06	0.022
Parallel 2	0.2	100[+]	0.868		1.88E-06	0.022
Parallel 3	0.1	100*	0.425		8.94E-07	0.010

[+] *V_{AC} applied after 17 hours.*

* *V_{AC} applied from the start.*

The lowest weight loss was measured for the sample tested in the absence of AC. As it can be seen from the table, the weight loss was lower when AC was applied from the start.

4.2.4 Surface morphology

Photos captured of specimens prior to removal of corrosion products and after such removal are used in combination with micrographs from a SEM study in order to investigate the morphology changes as a function of applied DC potentials and AC densities.

Figure 59 displays how the surfaces of 25 Cr were affected when samples were tested at the conditions specified above.
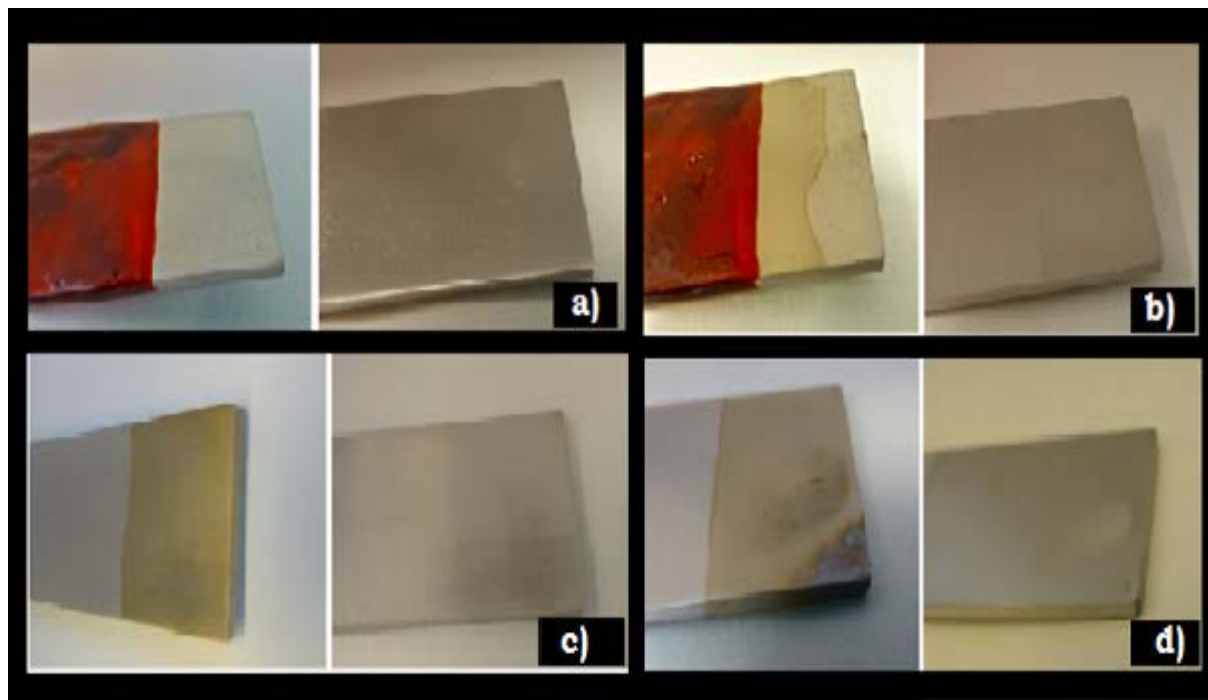
Figure 59: Photos of 25Cr sample surfaces tested at a) +100 mV and 0 A/m^2 AC b) +100 mV and 100 A/m^2 AC applied after 17 hours c) +200 mV and 100 A/m^2 AC applied after 17 hours and d) +100 mV and 100 A/m^2 AC applied from the start .

It can be seen that with applied AC, the surfaces changed color to yellowish tones. The sample tested with AC from the start seen in Figure 59d) had in addition some blue traces at its left corner. When the sample was removed from the test cell this corner was found to correspond to the part closest to the AC-counter electrode. As can be seen from a close-up of the area, pitting has also taken place in this area, see Figure 60 and Figure 61.
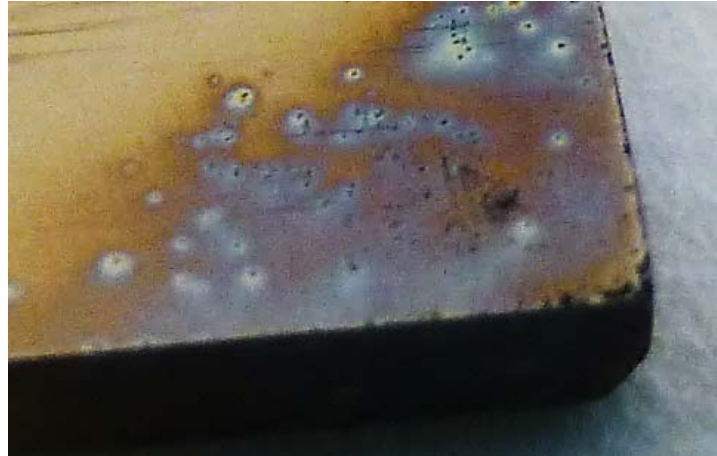
Figure 60: Corner on 25Cr sample tested at +100 mV and 100 A/m² AC applied from the start of the experiment. The surface is photographed <u>before</u> corrosion products were removed.
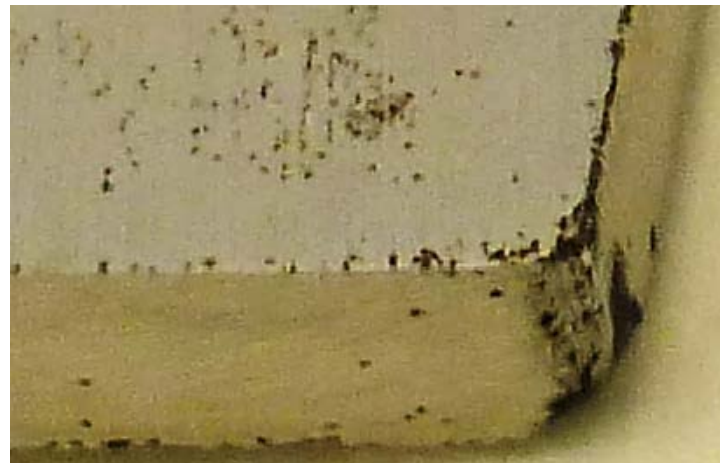
Figure 61: Corner on 25Cr sample tested at +100 mV and 100 A/m² AC applied from the start of the experiment. The surface is photographed <u>after</u> corrosion products were remove.

SEM micrographs were captured for all samples at magnifications of M=500X and M=1.5kX with working distances between of 5-10 mm and an accelerating voltage of E_0=15Kv.

SEM micrographs taken with 1.5kX magnification of samples tested at the different conditions are seen in Figure 62. Micrographs recorded at 500X magnification are provided in Appendix E.3.
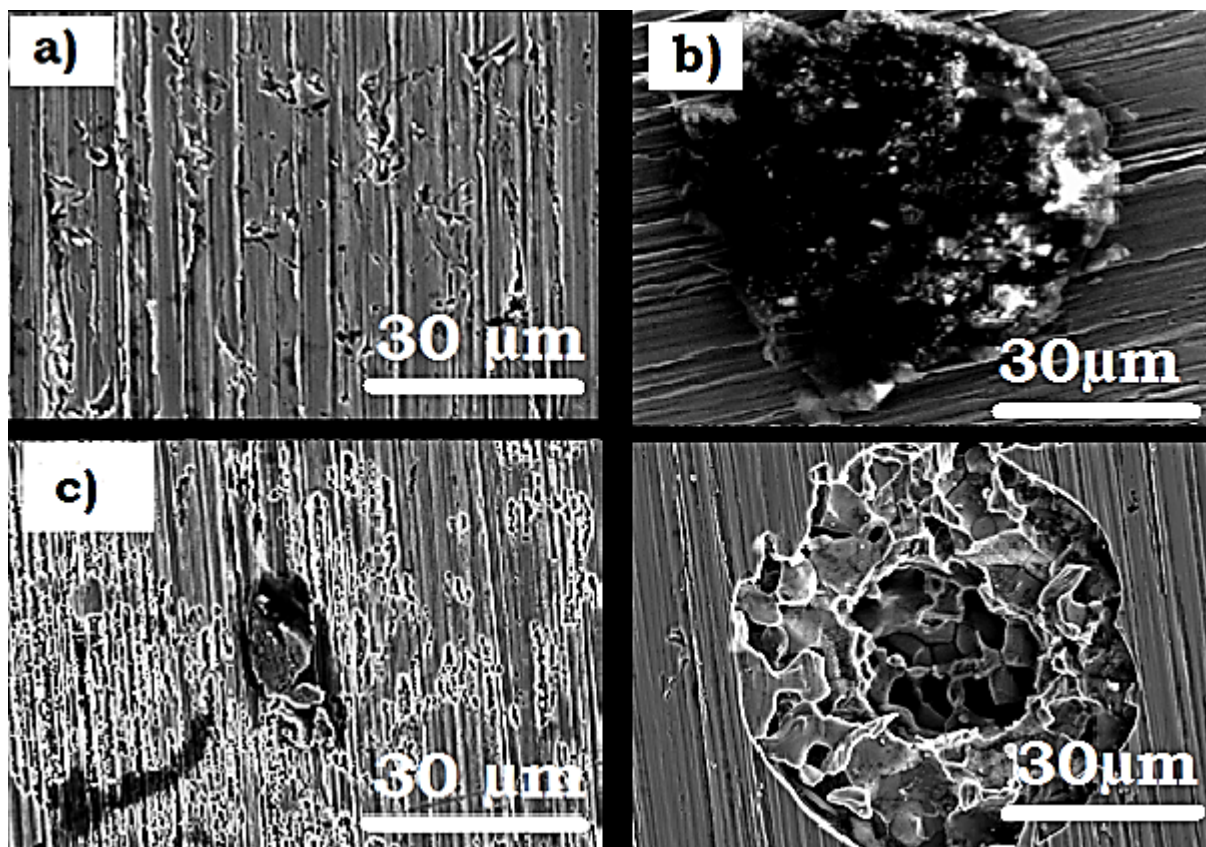
Figure 62: SEM micrographs of samples tested at a) +100 mV and 0 A/m² AC b) +100 mV and 100 A/m² AC applied after 17 hours c) +200 mV and 100 A/m² AC applied after 17 hours and d) +100 mV and 100 A/m² AC applied from the start. Seen at 1.5kX magnification.

From the micrographs it is possible to deduce two trends:

- pits increased in number and changed configuration when the DC potential was increased in positive direction, from +100 to +200 mV while AC was kept unchanged.
- pits changed configuration when AC was applied for a longer period of time, i.e. 72 hours instead of being applied 17 hours into the experiment, while DC was kept unchanged.

An EDS analysis of surfaces was performed as for 316L. The study showed no traces of platinum.

4.3   Summary of results

A summary of the most important results from the experimental work is given.

4.3.1   Cathodic polarization

Current behavior

The DC current response recorded was more negative for 316L compared to X65 for all applied AC densities at both -800 and -1050 mV. Currents made a negative shift for 316L when AC was applied at both -800 and -1050 mV while they made a positive shift when AC was applied for X65 at -800 mV. When cathodic current densities, $\left| i_{red} \right|$ are calculated from

the measured weight losses and the current response (see eq.(A.4) in Appendix A), it can be observed that $\left|i_{red}\right|$ increased on 316L at both DC potentials with increasing AC densities. In addition all $\left|i_{red}\right|$ were higher for 316L than for X65, as can be seen from Figure 63 and Figure 64.
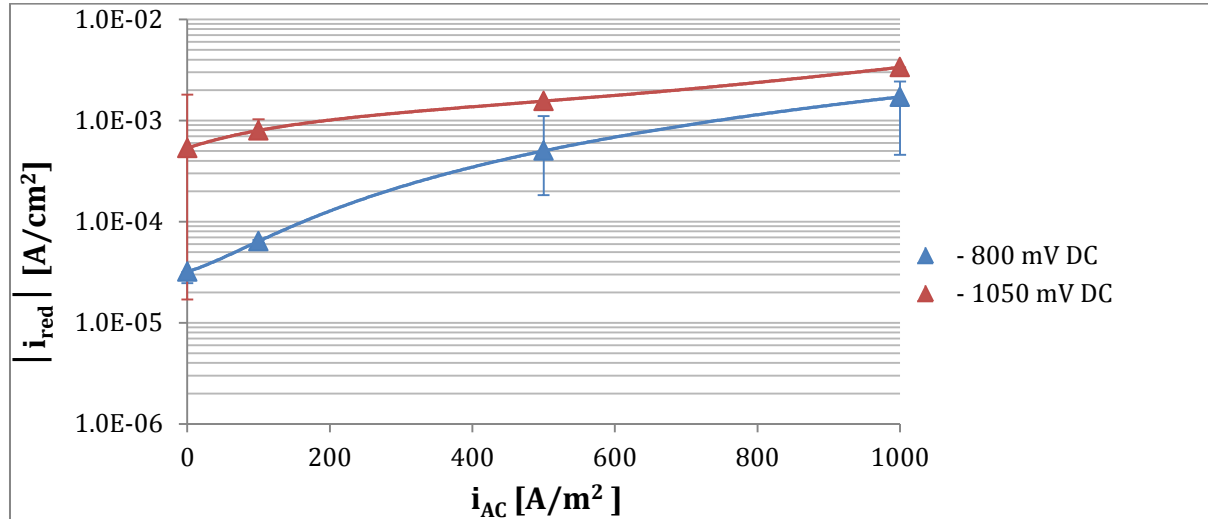
Figure 63: Calculated values for cathodic partial current densities for 316L during 72-96 hours of testing when increasing AC densities were applied under cathodic DC potentials.
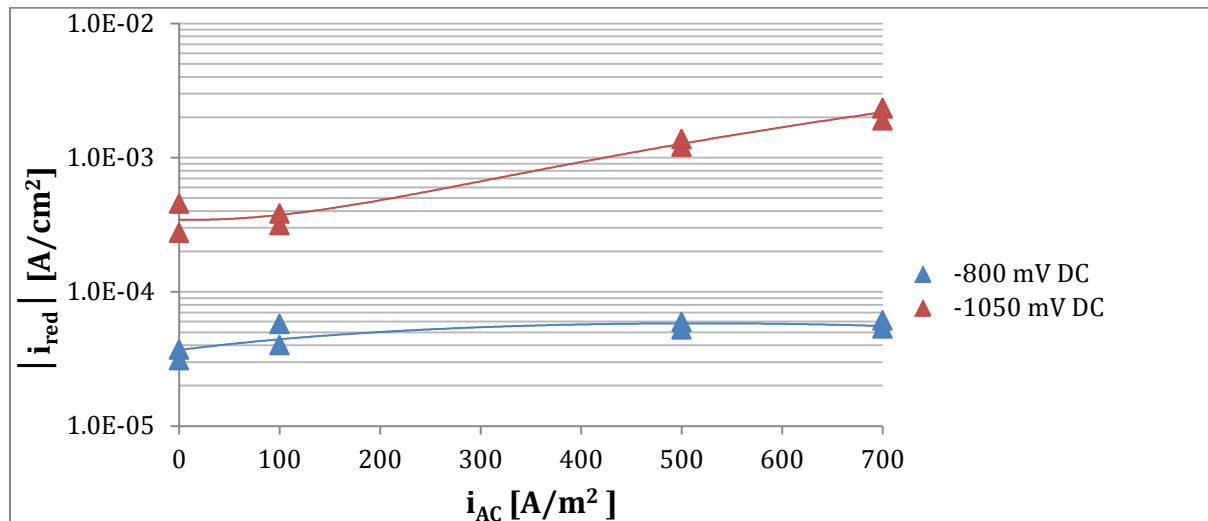
Figure 64: Calculated values for cathodic partial current densities for X65 during 72-96 hours of testing when increasing AC densities were applied under cathodic DC potentials.

AC cell potential

The highest V_{AC} for 316L was 2.182V identified at -800 mV and 1000 A/m^2 AC. The highest V_{AC} for X65 was 1.51 V seen at -800 mV and 500 A/m^2 AC. The averaged values ($\overline{V}_{AC}$) were higher for 316L compared to X65 for all applied AC densities at both -800 and -1050 mV.

Weight loss measurements

Corrosion current densities calculated from weight losses for 316L were at all times lower when compared with X65 at both -800 and -1050 mV. The highest corrosion current density registered for 316L – $9.69*10^{-6}$ A/cm^2 (0.113 mm/y) – was found at 1000 A/m^2 AC when

polarizing at -800 mV. The highest corrosion current density registered on X65 - 2.03 $*10^{-5}$ A/cm^2 (0.236 mm/y) – was found at 500 A/m^2 AC and -1050 mV.

Surface morphology

For 316L pits were found to both increase in density and change configuration with increased AC densities - from an etched pit type at lower AC density, to a polished pit type at high AC densities. On X65 the density and depths of pits increased with increased applied AC density, but decreased when increasing the cathodic potential. A layer of non-soluble film formed on 316L was in EDS identified to be a layer of Pt.

4.3.2   Anodic polarization

Open circuit potential

The E_{OC} was shifted by approximately 227 mV in the positive direction when 100 A/m^2 AC was applied relative to the recorded OCP value when no AC was applied, but shifted in the negative direction when higher levels of AC densities were applied.

Current behavior

The mass transport limited oxygen reaction i_{O2_lim} was graphically determined to 3$*10^{-5}$ A/cm^2 from polarization curves when AC densities of 0 and 100 A/m^2 were applied. The pitting potential was found to be 600 mV/SCE at 0 and 100 A/m^2 AC, while the passive region was found to lie between -100 mv and +200 mv. For higher AC densities the passive region disappeared, while the hydrogen reaction was found to make a positive potential shift.

AC cell potential

The V_{AC} was seen to take higher values at an applied AC density of 100A/m^2 relative to the measured values on 316L and X65 at this AC density.

Weight loss measurements

The lowest corrosion current density, 2.84$*10^{-7}$ A/cm^2, was measured for the sample tested in the absence of AC. The weight loss when AC was applied from the start 8.94$*10^{-7}$A/cm^2 was lower relative to the corrosion current density when it was applied after 17 hours – 1.88$*10^{-6}$ A/cm^2.

Surface morphology

The surfaces were observed to change color to yellowish tones with applied AC densities. When AC was applied from the start the sample developed blue-green tones on the corner identified to be nearest the AC counter electrode.

5   Discussion

From the performed experiments, the following observations can be made about the influence of the applied AC densities:

- The cathodic current densities for 316L increase significantly with increased AC at both DC potentials, while for X65 a similar behavior is only seen at -1050 mV.
- When the cathodic DC potential is increased from -800 mV to -1050 mV the corrosion rates decrease. The highest CR for 316L and X65 were found at the conditions where the highest averaged AC cell potential ($\overline{V}_{AC}$) were identified for the respective steels.
- Hydrogen evolution is the predominant cathodic reaction on 316L at all applied AC densities when the stainless steel is cathodically polarized. The same can be said for X65 at -1050 mV.
- The cell potential measured in the AC part of the circuit (V_{AC}) increases for the same applied AC density, as following:

<div align="center">X65< 316L<25Cr</div>

- On 316L and X65 pitting increases in number and depth with increased AC densities. On 25Cr pitting is seen to change configuration dependent on the AC-condition.

In the following chapter these observations will be discussed based on the literature provided in chapter 2 and with grounding in the overall collected data.

5.1   Polarization behavior

5.1.1   Cathodic kinetics

It is seen that the DC current response recorded for 316L is more negative compared to X65 for all applied AC densities at both -800 mV and -1050 mV (Table 6 in section 4.1, Table C.2.1/C2.2 and Table D.2.1/D.2.2 in Appendices). At -1050 mV and 1000 A/m^2 AC the average current response for 316L is -3.35*10^{-3} A/cm^2 while it is -2.17*10^{-3}A/cm^2 for X65 at -1050 mV and 700 A/m^2 AC. The most cathodic current behavior is seen to evolve at the highest applied AC density in combination with the highest cathodic polarization potential. The increase in cathodic direction for 316L is of two orders of magnitude at -800 mV and one order of magnitude at -1050, when increasing AC densities are applied relative to the current at no applied AC. In contrast to this, the current response is of same magnitude for X65 at -800 mV and increases with one order of magnitude at -1050 mV.

From the current response for 316L, the cathodic current density , $\left| i_{red} \right|$, is found to increase with one order of magnitude at -800 mV and with two orders of magnitude at -1050 mV when increasing AC densities are applied relative to the current when no AC is applied. In contrast to this it can be seen that for X65 all $\left| i_{red} \right|$ at -800 mV are of same magnitude (an increase of 40%) but increase with one order of magnitude at -1050 mV (Figure 63 and Figure 64). In addition, all $\left| i_{red} \right|$ are higher for 316L than for X65, with 3.35*10^{-3} A/cm^2 at -1050 mV and 1000 A/m^2 AC for 316L, versus 2.18 *10^{-3} A/cm^2 at -1050 mV and 700 A/m^2 AC for X65. The cathodic reaction rates are thus reflecting the current response recorded. Stainless steels

exhibit as expected (section 2.4) a higher cathodic activity than carbon steel during cathodic potentiostatic polarization under applied AC.

The cathodic behavior in the presence of AC is comparable with several previous reports: Stamnes [58] revealed for X65 a similar increase in reduction currents at -1050 mV while currents of same magnitude were reported at -800 mV, see Figure 14 (section 2.3.2.3). Also polarization curves for X65 recorded during the present study, Figure 94 (Appendix D.2), indicate the same: As the cathodic currents at -800 mV for all applied AC densities are ***mainly*** related to the mass transport limited oxygen reduction reaction (mixed control), these are found to be of same magnitude. At -1050 mV the hydrogen evolution controls the cathodic kinetics and $\mid i_{red} \mid$ increases one order of magnitude when increasing AC densities are applied. However, polarization curves suggest that cathodic reaction rates should have been higher than the calculated values from current response measurements, a concern also regarding 316L as can be seen from polarization curves reported for this steel grade [48] in Figure 17 (section 2.3.2.4).

When studying the polarization curves for 316L it is obvious that cathodic currents will at -800 mV increase with one order of magnitude when increasing AC densities are applied, whereas the increase will be of two orders of magnitude at -1050 mV. The increase is related to the complete disappearance of the oxygen reduction from the polarization curves when applying AC > 100 A/m^2. It was seen that hydrogen was the predominent cathodic reaction already at -600 mV when applying AC > 100 A/m^2 on 316L. From polarization curves recorded on 25Cr a similar cathodic behavior is identified. When AC densities are increased, the hydrogen reaction will be the predominant reaction during the cathodic half cycles of the AC applied. The mass transport limited oxygen reaction happened on both 25Cr and 316L at the same rate, $i_{O2\_lim} = 3*10^{-5}$ A/cm^2, when 0 and 100 A/m^2 AC were applied. At higher AC densities the reaction disappeared completely from the curves while the hydrogen evolution was seen to makes a positive potential shift, controlling the kinetics already at -600 mV. The consequence for 25Cr is the lost passivity. The pitting potential initially seen at 600 mV at 0 and 100 A/m^2 AC has apparently decreased to -100 mV. In addition the corrosion current densities were graphically determined at increasing rates (Table E.2.1 in Appendix E.2) with increased AC, probably caused by the observed acceleration of the hydrogen reaction.

Thus, hydrogen evolution is the reaction controlling the corrosion of stainless steels when AC current densities higher than 100 A/m^2 AC are applied at -800 mV, whereas hydrogen evolution is controlling the corrosion for all steel grades at all AC densities when polarizing to -1050 mV. Hence the increase in reduction rates of two orders of magnitude for 316L at -800 mV is explained by the fact that two different reactions are controlling the corrosion reaction at this DC potential – the oxygen reduction first and the hydrogen evolution next.

5.1.2 Current shifts

The current response for 316L at both -800 mV and -1050 mV makes a dip in the cathodic direction when AC is applied, before stabilizing on less negative currents, see Figure 29 and Figure 30. The time for the shift decreases with increased AC densities. At 100 A/m^2 AC and

-800 mV the shift happens during the 7th hour whereas it happens during the first hour at 1000 A/m^2 AC. The current response for X65 is contrary to the behavior for 316L observed to decrease steadily, as can be observed from Figure 31 - Figure 33. When tested at -800 mV currents actually makes a shift in the anodic direction after AC is applied. Goidanich [55] proposed that AC may cause a variation in the double layer's chemical composition with a consequent growth of corrosion product films on the surface.

The stabilization on less negative currents for 316L following the initial increase seen after some 20 hours may be related to an initial acceleration of the hydrogen evolution reaction to begin with, where in time the reaction will be slowed down by oxides formed on the surface and cathodic limitations related to the formation of a gas carpet. Pagano [47] explained the development as an activation of the surface followed by a subsequent increase in polarization resistance due to pH-effects and the formation of an oxide layer. The built-up of a gas carpet on the surface will hinder the conductivity at the interface, slowing down the kinetics of the corrosion process, with an ohmic resistance.

The highest positive current was measured at the highest applied AC density, i.e. 700 A/m^2 AC, at $4*10^{-4}$ A/cm^2 and at this AC density the DC currents are seen to be positive for the longest period of time, lasting 57 minutes. As a comparison the highest positive current measured at the lowest AC density, i.e. 100 A/m^2 AC, was found to be $1.92*10^{-6}$ A/cm^2 and the positive currents lasted a total of only 25 minutes. When integrating the positive current response over the time integral and thus finding the charge corresponding to these currents, it was found that weight loss measured at the end of the experiments were much higher than the weight loss corresponding this charge, which means that the dissolution of carbon steel is a process happening during the whole experiment and not specifically related to the conditions at the start at the experiment.

Similar shifts in the current response with applied AC were also seen on 25Cr. When AC was applied at 100 A/m^2 under anodic bias, the current response turned negative independent of whether it was positive or negative to begin with. In relation to this it can be observed that E_{OC} makes a positive shift at this AC density, explaining the negative current response recorded when AC is applied. The sample tested with no applied AC showed a decreasing anodic behavior - thus reflecting the increased stability of the oxide film formed during the anodization with respect to dissolution - as the resistance to corrosion imposed by oxides (on stainless steels) is explained by the semiconductive properties [13, 32] related to the alloying elements.

5.1.3 The AC potential

The changes occurring on surface of steel with increased AC may also be detectable by studying the recorded alternating cell potential, V_{AC}. The AC cell potential is a potential difference between the working electrode and the counter electrode (Pt) related to the ohmic resistance Φ at the electrode - see eq.(20).

$$\Delta V_{AC} = \Delta V_{AC\_Pt} - \Delta V_{AC\_steel} = \left(V_{AC\_Pt} - \Phi_{Pt} \right) - \left(V_{AC\_steel} - \Phi_{steel} \right)$$

(20)

Geometrical factors related to surfaces affected by formation of corrosion products or gas carpets, will influence the magnitude of the ohmic resistances. The variation of V_{AC} measured in time is not clearly understood, but it is seen an increase in the magnitude before a subsequent stabilization, hence surfaces are increasingly affected by either corrosion products or gas carpets. As Pt is an inert electrode, it is expected that the geometrical changes are mainly related to the changed surfaces of steel. As it will be discussed later in this chapter, on the surfaces of stainless steel it was found insoluble films containing platinum according to an EDS analysis (Appendix C.3.3/C.3.4). However, since V_{AC} for 316L does not differ much from the value measured on X65 – where platinum was not found – it is excluded that the changes in V_{AC} may be related to the changes of the Pt electrode affected and dissolving or that such layers may have shielded the electrode surface acting like a resistance.

The highest V_{AC} values for both 316L and X65 are seen to evolve at the same conditions that resulted in the highest corrosion rates (CR) reported. The highest V_{AC} for 316L was measured to 2.18V at -800 mV and 1000 A/m^2 AC. On X65 the highest V_{AC} measured was 1.5V at -800 mV and 500 A/m^2 AC. For X65, an investigation of the proportionality of corrosion current densities as a function of $\Delta V_{AC}{}^2$ - as the proportionality according to Orazem will be valid for steels corroding with an activation controlled corrosion kinetics [5] - did however not lead to any answers regarding the found correlation between CR and V_{AC} for X65.

When averaged over time, see Figure 65 , $\overline{V}_{AC}$ is higher for 316L for the same applied AC density compared to X65 and seen to increase with increased AC densities. The stabilization in $\overline{V}_{AC}$ for 316L from 500 A/m^2 at both potentials may imply that the resistance of the corrosion layer is unchanged when AC>500 A/m^2 is applied, but from weight loss measurements it can however be observed that material loss increases with increased AC density.
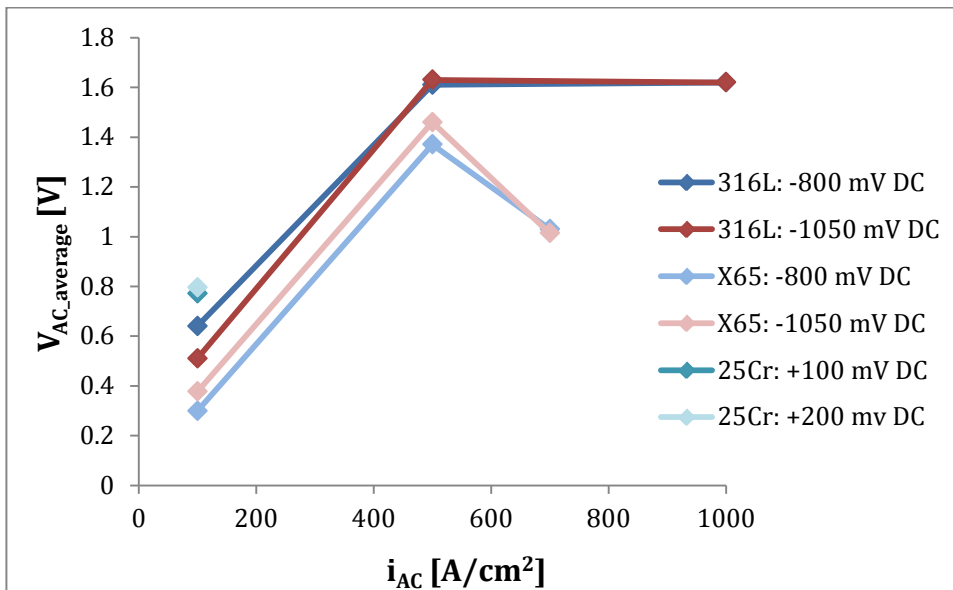
Figure 65: The average alternating cell potential $\overline{V}_{AC}$ measured and calculated for all three steel grades when increasing AC densities are applied at different DC potentials.

For X65 $\bar{V}_{AC}$ is seen to increase and then decrease, a trend also confirmed by the corrosion rates as these are seen to peak at 500 A/m^2 AC at both DC potentials. It is also interesting to observe that $\bar{V}_{AC}$ for X65 increases from -800 mV to -1050 mV but values for 316L do not change substantially. The observation may be related to the increase in cathodic kinetics which X65 experiences at -1050 mV relative to the rates at -800mV.

The V_{AC} is for 316L seen (Figure 34) to shift in the positive direction during the first 25 hours before stabilizing on lower values. For X65 the shift was also seen (Figure 35) but it observed during the first 10 hours. These observations correlate well with the reported shifts in current densities, before a subsequent stabilization. An increased resistance due to the built-up of gas carpets and oxide films may hence be the explanation.

A similar increase in V_{AC} was also measured for 25Cr during the anodic potentiostatic polarization tests, but it gains higher maximum values than for experiments on both 316L and X65 at an applied AC density of 100A/m^2. Assuming that surfaces of samples are oxidized during the anodization process - as also the yellowish color of samples when removed from test cells may indicate - the surfaces are covered with passive film layers. When comparing with $\bar{V}_{AC}$ data measured and calculated for 25Cr at 100 A/m^2 AC, it can be observed that $\bar{V}_{AC}$ is higher than the ones for both 316L and X65 at this AC density. The higher $\bar{V}_{AC}$ for 25Cr may suggest an increased polarization resistance corresponding to a thicker anodically grown oxide. As 25Cr contains more Cr than 316L, see Table 1, the oxide formed will also have a higher resistance against electronic conductivity.

5.1.4   The alkalization process

High cathodic DC currents will along with AC sources result in higher pH levels due to the production of OH$^-$ first by $2H_2O + O_2 + 4e^- \rightarrow 4OH^-$ and then by $2H_2O + 2e^- \rightarrow H_2 + 2OH^-$, thus leading to an alkalization of the surface for both steel grades. Inside pits formed on the surfaces of steel, an acidification process will take place simultaneously.

Oxides on carbon steel will form easily at 10 <pH<12 and be stabilized in this pH region. At pH>13 the alkalization will be detrimental according to the Pourbaix diagram Figure 4 (section 2.2.1). Stainless steels alloyed with Ni, will have oxides stabilized at high pH as well. A surface enrichment of a monolayer of Ni on steel will in addition increase the resistance by decreasing the kinetics for active dissolution [34], as Ni is seen to buffer the local pH thus slowing down the acidification in the pits [35]. The oxides formed on stainless steel have a higher resistance than oxides formed on carbon steel against ion mobility related to Cr, which has a lower electronic conductivity than Fe, and to Mo which blocks the penetration of Cl$^-$ [33].

Hence, the net weight loss measured for 316L is related to the acidification process inside the pits. Here the dissolution may have been autocatalytic due to decreased pH caused by the hydrolysis of steel in combination with the oxidation of Cr to Cr^{3+}, thus resulting in the build-up of a film containing Fe-Cr in the pits. The formation of an oxide layer will increase the

polarization resistance inside the pit. During the anodic half cycles of AC, new pits may be formed on the surface.

For X65 the corrosion measured is related to the alkalization process during the cathodic half cycles and the active dissolution during the anodic half cycles. Carbon steels corrode mainly uniformly in neutral saline solution, but pitting corrosion has also been observed especially when deposit layers are present on the steel surface [9]. Thus pitting will happen on carbon steel underneath the layer of corrosion products when AC is applied.

5.2   The AC corrosion mechanism

From the present study it is seen that $\left| i_{red} \right|$ increases at -1050 mV with two orders of magnitude for 316L and one order of magnitude for X65 with increased AC density from zero to 1000 A/m^2. At -800 mV the increase is of one order of magnitude for 316L while for X65 it is about 40% for the same increase in the AC density. These results indicate a significant acceleration of cathodic kinetics with applied AC. Weight loss measurements indicated also an increase in the corrosion rate with increased applied AC. However, the cathodic reaction rates were much higher than the anodic reaction rates at these two applied DC potentials.

Two reactions are responsible for the cathodic processes: the oxygen reduction, eq.(11) and the hydrogen evolution reaction, eq.(12). Both reactions result in increased pH by the production of OH$^-$. Both reactions require the diffusion of reactant to the reaction site. The application of AC is however from present and previous [48] studies by the author found to affect the hydrogen evolution by catalyzing it on stainless steel already at -600 mV and for X65 the acceleration is seen from -900 mV (Figure 16). The observed acceleration of cathodic kinetics for 316L under applied AC is by the author found to be related to a positive potential shift for the hydrogen evolution reaction. Similar studies known from literature show that the hydrogen evolution is happening at less negative potentials [64]. Also on carbon steel it is found evidence from literature [3, 55, 57] for such an increase in potential for the hydrogen reaction, however the author has no evidence for such.

In addition, the Tafel constants for the hydrogen reaction are from polarization curves on 316L seen to decrease with increased AC. Reports by Bockris and Matthews [72] explain an experimentally observed decrease in Tafel constants with a decrease in temperature. In this study the temperature is kept stable by a temperature controlled water bath water. Therefore, the explanation is not seen as satisfactory. Bolzoni [3] reported a decrease in Tafel slopes for the hydrogen reaction on carbon steel during cathodic polarization with applied AC, Wendt et al [63] reported the same for stainless steels.

The oxygen reaction is not seen to be affected by the applied AC. The cathodic polarization behavior of carbon steel is believed to be under mixed control and i_{O2_lim} is not seen. From polarization curves on 316L and 25Cr it is evident that the mass transport limited oxygen reduction reaction happens at same rate independent of the applied AC. The value is graphically determined from cathodic polarization curves recorded on 316L and 25Cr to be $3*10^{-5}$A/cm^2. The reaction was only detected at 0 and 100A/m^2 AC while higher AC densities

result in a cathodic kinetics being controlled by hydrogen evolution. When the corrosion reaction shifts from being controlled by the oxygen reaction to being controlled by the hydrogen reaction, the corrosion rates evidently increase.

The reason for the increased kinetics for the hydrogen reaction is still unknown. A sinusoidal AC signal present is seen to contribute to the resulting potential by superposition, which is not symmetric some workers suggest [3, 49-51]. Theoretical works [5, 52] show that AC of large amplitudes applied at low frequency will contribute to the electrochemical reaction by generating a DC potential of a magnitude proportional to the square of the applied AC, leading to a contribution of the AC applied potential to the faradaic reactions given by $i_f = i_{corr \ DC + AC}$. Recently [54] voltammetric studies at high AC amplitudes, show that irreversible processes are accelerated due to an accelerated electron-transfer and an alteration of the concentration of immediates, which under certain circumstances may lead to an alteration in the reaction mechanism. While only hydrogen evolution is however seen to be accelerated during the cathodic half cycle, passivity is seen to be lost for stainless steels as can anodic polarization curves recorded on 316L and 25Cr reveal. The cyclic nature of AC will thus affect both anodic and cathodic processes, but no evidence is found that the oxygen reaction is affected, only by its disappearance it becomes evident that the diffusion of oxygen to the surface cannot keep up with the speeded kinetics.

Analyzing the results from a cathodic protection perspective it is obvious that the current response for 316L developing in a more cathodic direction also implies that when increasing AC densities are applied, the current demand for protection of the steel increases in accordance with the relation $\sum I_{ox} = \sum \left| I_{red} \right|$.

5.3 Weight loss

The highest corrosion rates (CR) 0.205 mm/y and 0.236 mm/y were found for X65 at 500 A/m^2 AC and -800 mV and -1050 mV DC respectively. (Table C.1.1 and C.1.2 in Appendix C.1 and Table D.1.1/D.1.2 in Appendix D.1). The highest CR for 316L - 0.113 mm/y - was found at -800 mV and 1000 A/m^{2}AC. The corrosion rates for 316L increase with applied AC with one order of magnitude at - 800 mV and with orders of magnitude at -1000 mV. For X65 the increase is with one order of magnitude at both - 800 mV and - 1000 mV.

The measured weight losses for 316L are thus as expected (section 2.4) lower when compared with X65. The lowest CR was found for 316L when exposed to the most cathodic potential, i.e. -1050 mV. At this potential also X65 displays in general lower corrosion rates than at -800 mV.

However, at 500 A/m^{2}AC and -1050 mV/SCE there is actually seen an increase in corrosion rates. In addition it is found that both steel grades experience an increase in corrosion rate in the absence of AC when applying -1050 instead of -800 mV. For 316L the increase measured is 66% while it is 43% for X65. For X65 the behavior can be explained thermodynamically, as the alkalization process happening faster at -1050 mV will destabilize the surface (as

explained in section 5.1.3) possibly leading to the higher weight loss measured here relative to the measurement at -800 mV. However, for stainless steel, the surface is actually stabilized by Ni. Hence by this, the finding for stainless steel may be seen as an incorrect measurement. The weight losses at -1050 mV and 0 AC are for both 316L and X65 very small and may result in large errors.

Similar results for X65 have been reported before, see Figure 37, by Stamnes (NTNU, 2010) [58]. The corrosion rates at both 0 and 500 A/m^2 AC lie at -1050 mV above the rates at -800 mV. However the similarities stop more or less here, as can be depicted from Figure 66 when plotting the results by Stamnes together with results from the present study.
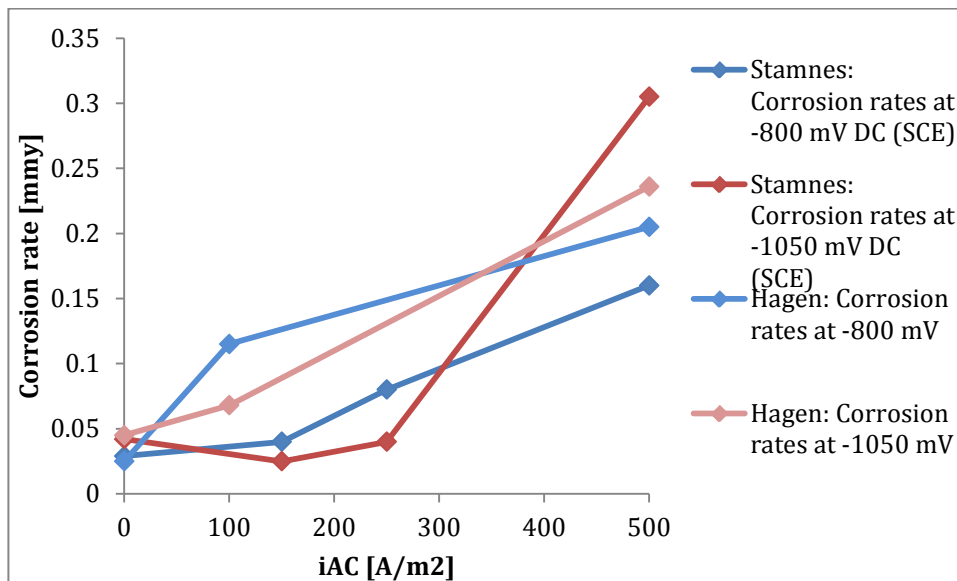
Figure 66: Corrosion rates calculated from weight losses under potentiostatic polarization from studies by Stamnes (2010) and Hagen (2013).

The highest corrosion rate registered on X65 in the present study – 0.236 mm/y – is found at 500 A/m^2 AC and -1050 mV while the value at this AC density from Stamnes's study is seen to be 0.305 mm/y. Weight loss measurements are unfortunately sensible to different types of errors and studies [73] have confirm that weight loss data sometimes leads to higher corrosion rates than electrochemical data.

According to the ASTM standard G1-03, corrosion rates calculated from mass losses can be misleading when deterioration is highly localized as in pitting or crevice corrosion products due to unsuccessful removal of corrosion products. For X65 it has been observed very different mass losses related to the process of corrosion products removal, as the standard does not provide precise information about the immersion time. In a previous study by the author (Autumn 2012) cycles with an immersion time of 10 minutes were used, but when same procedure was employed at the start of the current study, weight losses were found to be too high relative to the amount of cathodic potential applied and immersion time for removal of products was shortened down to 30 seconds. Where only one such immersion was necessary to remove all products in the previous study, 3-4 such cycles were found necessary

for this present study. After removal surfaces were upon inspection found free for corrosion products, something being confirmed by the SEM and EDS analysis of surfaces.

As all weight losses measured for 316L are found to be lower than the analytical weight's error of ±1mg, the weight losses for these steel grades should not be given much importance on their one – but be used as additional information about the polarization effect of applied AC on material losses. For 316Lit is seen that the higher cathodic protection, the better effect against AC. With increasing AC, the weight losses increase. The same applies with regards to errors possibly introduced for weight losses measured for 25Cr after anodic polarization. It is however interesting to observe that the weight loss is lower when AC is applied from the start relative to the application after 17 hours. As the potential of the sample was seen to shift in anodic direction when measured under open circuit conditions whith applied AC and the current response turned cathodic when 100 A/m^2 AC was applied – AC may increase the resistivity of the oxide formed.

5.4 Surface morphology

The most interesting morphological findings were obtained on stainless steels: Grain boundary corrosion was identified at the highest voltage combinations of DC and AC. For all applied AC densities in combination with high DC cathodic potentials, a layer of platinum was determined by an EDS analysis. On 25Cr a colored film layer formed during the anodic polarization. The film was blue – on the corner close to the AC counter electrode - when AC was applied for 72 hours, while it was yellowish when AC was applied for 55 hours. A higher applied DC potential did not lead to any changes.

Grain boundary corrosion is usually related to a sensitization process happening during high temperature treatments of stainless steel, the temperature reported from literature as T>500°C [46], where the depletion of chromium around grains may lead to corrosion when the material is put in service in a corrosive environment. The AC is in the industry actually employed for its heat generating effect, but it is seen as very unlikely that such high temperatures as the diffusion of chromium needs, actually evolved as extreme temperatures are counteracted by the utilized water bath with temperature controller. It is most probably that the processing method of the plates used for testing resulted in the depletion of chromium around the grains by diffusion. The boundary corrosion was localized in areas with a high density of crevices and pits at the coating/metal interface. As the samples were handled carefully prior to immersion in electrolyte the crevices, pitting and the grain boundary corrosion have most probably formed simultaneously in a sensitized area where potential gradients easier could be formed [39]. The pits are not surprisingly found in areas with crevices as it is known that in the presence of a layer of rust pitting has seen to increase in propagational speed [40].

Pits were found to become deeper with increased AC densities and they changed configuration from an etch-pit type at lower AC density, to the polish-pit type at high AC densities. The etch pit type is related to the more active type of pitting happening at lower potentials in the active states, while the polished type happens when surfaces usually are

covered by a salt layer at high potentials during the transpassive dissolution [13]. Pit propagation is thus possible despite the resistance present. The high AC cell voltages recorded indicate that during the anodic half cycle, potentials may have reached substantially high values. The highest V_{AC} was measured at 2.2 V, a potential which even when superimposed on cathodic potentials will be far beyond the transpassive dissolution. However, also numbers of pits were found to increase significantly and at the highest AC density the surface was greyish when inspected visually, but the SEM study revealed the color was a result of the high pit density.

The platinum layers found on 316L may be related to the high potentials arising from the combination of DC and AC on stainless steel, thus implying that it is the platinum counter electrode in the AC side of the circuit which is the donor of Pt. With chloride ions present Pt is more prone to oxidation by formation of chlorine complexes, and with the AC densities applied this process will go even faster, as literature has reported due to a possible de-passivation of the metal during the negative half-cycle of AC. Recent studies on the electro dissolution of platinum under potentiodynamic and galvanodynamic conditions in combination with applied alternating currents have shown that the maximum amount of dissolved platinum actually occurs at the frequencies close to 50Hz[62].

Also Fe was found to be present in this film, but due to a high emission volume generated by the applied accelerating voltage (15kV) this can be regarded as the signal of the surface underneath the film layer. While the surfaces free of film have a Cr content more or less according to the material specification for 316L, the Pt layers were found to contain around one third of this content thus also probably being the signal of the surface underneath that contributes. There is found some oxygen on the surfaces both with and without Pt-film, but the oxygen is most likely trapped on the sample surface during the analysis and may be seen as a source of error. It may be that platinum contributed to increase the amount of hydrogen gas formed as hydrogen has a lower overpotential on Pt than on steel, hence resulting in a carpet of gas covering the electrode surface and thus the increased V_{AC}. It may thus be that the dissolution and subsequent plating of platinum is actually controlling the current response seen on steel and also the surprising linear weight loss with increased AC which is not expected from previous findings at E_{OC}.

When anodizing with AC, the surface will transform into an oxide by the dissolution of steel accompanied by the reduction of chromium. Different thicknesses will lead to different colors due to interference of light reflected at the oxide film/air and steel/oxide interfaces [19]. All 25Cr samples were covered by a yellowish oxide when removed from test cells, except for the sample tested with the longest duration of applied AC samples covered with a blue film on one part of the surface. The film was found on the corner near the AC counter electrode. Higher current densities may have been generated here leading to increased corrosion damages. When the film was removed several deep pits of irregular shape were identified.

The morphology of 25Cr changed both with applied DC and AC. By increasing the DC potential while keeping the AC constant, the density, depth and configuration of pits is seen to change from polished pits of a low number to shallow pits of irregular shaping covering the entire surface. By increasing the duration AC is applied while keeping the DC potential unchanged, pits are few, deep and of highly irregular shape.

Corrosion products on 316L were seen to dissolve when immersed in the removal solution, while those removed from carbon steel, flaked off and were identifiable on the bottom of the solution container. On 316L at -1050 mV and 1000 A/m^2 a black thick layer of corrosion products was observed, as can be seen in Figure 41 probably corresponding to the layer of platinum consisting film. On carbon steel the increase in cathodic potential evidently decreased the density and depths of pits as only a trace of pitting can be seen at -1050 mV in comparison with the surface morphology at -800 mV. However at 1000 A/m^2 AC and -1050 mV less pitting had happened, in contrast to the extensive pitting found at 500 A/m$^{2.}$AC. The observation is surprising, as higher AC was expected to result in more pitting. But when compared with results from weight losses, the SEM study actually supports the higher corrosion rates measured at the lower AC density. Compared with the pits on 316L they are less articulated in the means of pits growing isolated in depth with well-defined shapes. Pits on carbon steel are either small or identified to have emerged to a mass of close-lying pits giving the impression of uniform corrosion.

5.5 Evaluation of apparatus

The equipment was calibrated before experiments were started. A Faraday cage was used together with a dummy cell to calibrate the in-PC Gamry potentiostats. In addition all wires and connections were tested to ensure good conductivity. It is therefore assumed that the measured currents are correct. But as currents on 25Cr during the anodic polarization were measured as low as on nano-amp levels, it is to be questioned whether the resistance the currents were measured over was appropriate. The potentiostat in use is known to have an accuracy of 10µm. Measurements will thus potentially contain a lot of noise and not actually resemble the surface electrochemistry of the 25Cr samples.

Upon designing the experimental procedure, it was discussed to apply AC potentials instead of densities. Actions were taken in order to make the system possible to gain the AC potential levels wanted by excluding the filters inserted in the system - the effectiveness of which are unknown and assumed to give less than 0.01 % interference as reported by Bolzoni *et al.* [3]. In the AC part of the circuit a capacitor inserted to filter out DC currents, has a high resistance – around 8-11 (several parallels means several test cells, means several capacitors with different resistances) – making it difficult to apply AC potentials over ca. 3.8 V even when test areas were decreased. In addition, by operating the VariAc at its voltage limit, results in a non-steady delivery of current.

The exclusion of the filters was seen to cause two problems: 1) The need for a logging system that can distinguish between AC and DC being able to measure currents of small magnitude and 2) it would affect the experimental procedure chosen with the use of a potentiostat. If current would instead be supplied by anodes, a constant V_{AC} could instead have been applied. It was therefore decided to apply constant AC densities instead of constant AC potentials. Applying AC densities instead of potentials is also seen as being more adequate, taking in account the influence of geometric factors on potential.

Filters may be excluded on later experiments, if enough multimeters of the kind mentioned are available **or** if DC currents are supplied by sacrificial anodes. However, the counter electrodes on the AC side of the circuit were found to dissolve under the combination effect of high DC and AC voltages. Bigger test cells would allow for bigger counter electrodes, thus decreasing the current densities on these.

For the surface analysis SEM and EDS were used. However, due to the high emission volume related to EDS, for a higher depth resolution X-ray photo electron spectroscopy (XPS) or Glow discharge optical emission spectroscopy (GDOES) should be considered. The former analysis method will give information about both elements and their oxidation state, while the latter does not give information about the oxidation state. The analysis if applied both before and after testing can reveal the state of oxide films and any eventual enrichment of alloying elements on the surface of steel. In addition a photo camera with better macro capabilities should be employed for better close ups of the samples.

5.6   Evaluation of test procedure

In order to achieve an adequate reproducibility of results, it is important to ensure the same initial surface preparation for all samples prior to each experiment. Surface preparation was during the present study not controlled in a thorough manner: i) Surfaces were not polished in a standardized manner. As samples were much bigger than the exposed area and these were not possible to embed into epoxy resins, only the area to be exposed was polished while the remaining was left unpolished. ii) In addition the polishing left marks on the surface as either vertical or horizontal lines. As can be seen from SEM micrographs, pits and surface damages were located along either horizontal or vertical lines in the material (Appendix C.3.1/C.3.2 and Appendix D.3.1/D.3.2). This can have influenced the corrosion rates on stainless steels as the main cathodicreaction is the evolution of hydrogen and the amount of gas which possibly is entrapped in such paths will influence the net current response recorded.

Leakage of Cl$^-$ ions from the salt bridges into the electrolyte may in addition have contributed to the aggressive environment, hence resulting in higher corrosion current densities than it really is the case. It was observed at a couple of occasions that Agar mass was about to slip out from the glass container.

As pitting on stainless steel was localized close to crevices (Figure 42) at the coating/metal interface both during the present study and the previous project study, corrosion rates may have contributions corresponding to crevice corrosion. The concentration of aggressive ions and the acidification process inside the crevice influences all the determined parameters regarding stainless steels.

E_{OC} measurements of 25Cr (Figure 48) indicate that a stabilization time of around 10 hours is required for the samples to reach a steady-state free circuit potential under the influence of AC. But prior to the performed anodic polarizations, the samples were not allowed to settle for more than maximum 1 hour. The time needed for stabilization may be related to the wetting of the oxide by the electrolyte and thus to the rates of the different reactions happening on the metal surface. A shorter conditioning time before anodization may have resulted in slightly more positive start values for the samples tested in the absence of AC, as it can be seen that E_{OC} increases in time for 0 AC. Electrochemical data is in addition only available for only one parallel. For the samples tested with AC applied after 17 hours the conditioning time should not have any influence, since the oxide layer meanwhile has changed the surface conditions. For the sample tested with AC from the start, the short conditioning time may have resulted in higher negative currents at the start of the experiment than it is actually is the case, as the potential can be seen to make a positive shift during the first hour, before stabilizing on lower values.

6   Conclusions

The cathodic polarization behavior of 316L stainless steel has been studied and compared with the polarization behavior of X65 carbon steel. An investigation of the passivity of stainless steels with and without AC was done by anodic polarization test of 25Cr.

➢ The results indicate a significant acceleration of cathodic kinetics with applied AC. Weight loss measurements indicated also an increase in the corrosion rate with increased applied AC. However, the cathodic reaction rates were much higher than the anodic reaction rates at the applied DC potentials, -800 mV and -1050 mV (SCE).

➢ The corrosion kinetics for stainless steels at -800 mV changes from being controlled by the oxygen reduction reaction to be controlled by the hydrogen evolution reaction at AC>100 A/m^2, whereas hydrogen evolution is controlling the corrosion for all steel grades at all AC densities when polarizing to -1050 mV.

➢ From the present study it is seen that $\left| i_{red} \right|$ increases at -1050 mV with two orders of magnitude for 316L and one order of magnitude for X65 with increased AC density from zero to 1000 A/m^2. At -800 mV the increase is of one order of magnitude for 316L while for X65 it is about 40% for the same increase in the AC density.

➢ The highest $\left| i_{red} \right|$ for 316L is 3.35*10^{-3} A/cm^2 at -1050 mV and 1000 A/m^2 AC. The highest $\left| i_{red} \right|$ for X65 is 2.18 *10^{-3} A/cm^2 at -1050 mV and 700 A/m^2 AC.

➢ The highest CR for X65 were found when applying 500 A/m^2 AC both at -800 mV and -1050 mV, with 0.205 mm/y and 0.236 mm/y respectively. The highest CR for 316L was 0.113 at 1000 AC and -800 mV.

➢ The passive region at 0 and 100 A/m^2 AC is for 25Cr between -100 mv and +200 mv. For higher AC densities it contracts to a small interval around 0 mV while the hydrogen reaction is seen to make appositive potential shift.

The following AC mechanism is proposed:
- The cyclic nature of AC will affect both anodic and cathodic processes.
- The hydrogen reaction is seen to be formed at less negative potentials and increased exchange current densities. Tafel constants are also seen to change. No evidence is found that the oxygen reaction is affected.
- The corrosion reaction switches from being controlled by the oxygen reduction to be controlled by hydrogen evolution.
- Corrosion rates are seen to increase.
- The passivity is seen to be lost, and potentials are seen to make shifts. The shifts depend of the electrochemical system.

The results implicate that:
➢ The presence of AC decreases the effectiveness of the cathodic protection.
➢ The current demand increases with increased AC density.

7   Further work

A proposal of further work regarding improved methodology and electrochemical experiments to supplement or replace the current ones are in this chapter provided based on the experiences made during this study:

➤ Performing galvanostatic experiments, i.e. applying constant currents thus monitoring the potential. As the current response is found to make shifts both in the negative and positive direction when AC is applied, it is of interest to monitor the potential behavior under galvanostatic cathodic and anodic polarization.

➤ Applying the cathodic protection effect by sacrificial anodes thus excluding the need for using Pt-electrodes can be considered as an alternative method in the investigation of the AC corrosion mechanism. It will however introduce new concerns related to the galvanic connection of two metals simultaneously being affected by AC.

➤ Increasing the exposure period of samples from three days to at least one week will give more information about the AC-mechanism on stainless steel. It will also decrease the sources of error related to the small weight losses measured.

➤ In order to discriminate the potential error sources, the surface finish of samples has to be standardized by the use of smaller test samples which can be mounted in epoxy resin and polished thoroughly on all the surfaces by dissolving the resin and repeating the procedure for all sides. The surface morphology will be highly dependent on process parameters such as belt speed and the pressure which is applied upon the sample when polishing it. Therefor same speed and same pressure should be applied on all samples, and same polishing direction should be complied for 220-500-1000 papers when polishing.

➤ Preliminary SEM study to identify whether scratches and other surface defects were eliminated during the polishing process on samples. Preliminary EDS/GDOES/XPS investigations of sample surfaces to identify the character of eventual films present.

➤ The passivation prior to the testing has to be strictly controlled by either storing the samples in Argon rich atmosphere, i.e. Argon filled container until the treatments can be performed, or exposing the samples to air for the same amount of time and the same conditions before introducing them into the NaCl solution. The exposure to air after mechanical polishing and before coating must also be controlled.

➤ A crevice-free cell may be considered employed to exclude contributions from crevice corrosion on the pitting properties of stainless steel.

➤ Pitting is temperature dependent. Temperature should be monitored locally by a temperature sensor at the surface of the sample. Thus the critical pitting temperature

(CPT) could be tested in relation to AC. By applying AC while polarizing the stainless steel up to the pitting potential for the specific AC, the temperature could be raised from 0 up to 90 ^{O}C.

➢ The alkalization process on carbon steel can be considered monitored by a pH-meter. Information about local pH gradients will also give information about the hydrogen reaction on stainless steel.

➢ The content of hydrogen in the steel before and after samples have been tested with applied AC may change dramatically due to the increased hydrogen kinetics on stainless steels seen with applied AC. Measuring this content can be fruitful to understand more about the evolution of hydrogen when AC is present but also from a hydrogen embrittlement perspective, as it is known that an overprotection of steel increases the risk for stress corrosion cracking (SCC).

References

1. Hosokawa, Y., *Overcoming the new threat to pipeline integrity : AC corrosion assessment and its mitigation in 23rd World Gas Conference2006: Amsterdam. p. 18.*

2. DNV, *RECOMMENDED PRACTICE RP-B401, in CATHODIC PROTECTION DESIGN2011, Det norske veritas. p. 37.*

3. Bolzoni, F., et al. *Laboratory test results of AC interference on polarized steel. in CORROSION 2003 2003. San Diego, California, USA: NACE Conference Papers (NACE International)*

4. Strandheim, E.O., *AC induced corrosion of Carbon Steel in 3.5 wt % NaCl, in Department of Materials Science and Engineering2012, Norwegian University of Science and Technology: Trondheim. p. 72.*

5. Orazem, M.E. and B. Tribollet, *The Electrochemical Society Series. Electrochemical Impedance Spectroscopy. 2008: John Wiley & Sons, Inc.*

6. King, F. and M. Kolar, *Theory Manual for the Steel Corrosion Model Version, 2009, Integrity Corrosion Consulting Ltd. LS Computing Ltd.*

7. Lu, Z., et al., *Effects of a magnetic field on the anodic dissolution, passivation and transpassivation behaviour of iron in weakly alkaline solutions with or without halides. Corrosion Science, 2006. 48(10): p. 3049-3077.*

8. Webb, S.L. and G. Bohnsack, *The Kinetics of the Schikorr Reaction on Steel Surfaces at Low Temperatures. Corrosion, NACE, 1989. 89(31).*

9. Meng, G.Z., C. Zhang, and Y.F. Cheng, *Effects of corrosion product deposit on the subsequent cathodic and anodic reactions of X-70 steel in near-neutral pH solution. Corrosion Science, 2008. 50(11): p. 3116-3122.*

10. Uhlig, H.H., *Passivity in metals and alloys. Corrosion Science, 1979. 19(11): p. 777-791.*

11. Beverskog, B. and I. Puigdomenech, *Revised pourbaix diagrams for iron at 25–300 °C. Corrosion Science, 1996. 38(12): p. 2121-2135.*

12. Hamilton, D.L. 2000 *[cited 2013 04.06]; The Pourbaix diagram]. Available from: http://nautarch.tamu.edu/CRL/conservationmanual/File9.htm.*

13. Sato, N., *An overview on the passivity of metals. Corrosion Science, 1990. 31(0): p. 1-19.*

14. Olsson, C.O.A. and D. Landolt, *Passive films on stainless steels—chemistry, structure and growth. Electrochimica Acta, 2003. 48(9): p. 1093-1104.*

15. Shih, C.-C., et al., *Effect of surface oxide properties on corrosion resistance of 316L stainless steel for biomedical applications. Corrosion Science, 2004. 46(2): p. 427-441.*

16. Klages, P.E., et al., *Enhancing resistance to pitting corrosion in mechanically polished stainless steel 316 LVM by water treatment. Electrochemistry Communications, 2012. 15(1): p. 54-58.*

17. Knudsen, O.Ø. and T.M. Devine *Formation of Surface Oxides on 13% Chromium Stainless Steel.*

18. Carmezim, M.J., et al., *Capacitance behaviour of passive films on ferritic and austenitic stainless steel. Corrosion Science, 2005. 47(3): p. 581-591.*

19. Stoychev, D., et al., *Chemical composition and corrosion resistance of passive chromate films formed on stainless steels 316 L and 1.4301. Materials Chemistry and Physics, 2002. 73(2–3): p. 252-258.*

20. Bruzzoni, P. and E. Riecke, *On the mechanism of hydrogen transport through the passive oxide film on iron. Corrosion Science, 1994. 36(9): p. 1597-1614.*

21.	Ameer, M.A., A.M. Fekry, and F.E.-T. Heakal, *Electrochemical behaviour of passive films on molybdenum-containing austenitic stainless steels in aqueous solutions.* Electrochimica Acta, 2004. **50**(1): p. 43-49.

22.	Vijh, A.K., *Electrical properties of non-metallic deposits.* Surface Technology, 1976. **4**(1): p. 7-30.

23.	Szklarska-Smialowska, Z., *Pitting corrosion of aluminum.* Corrosion Science, 1999. **41**(9): p. 1743-1767.

24.	Elfström, B.O., *The effect of chloride ions on passive layers on stainless steels.* Materials Science and Engineering, 1980. **42**(0): p. 173-180.

25.	Olefjord, I., *The passive state of stainless steels.* Materials Science and Engineering, 1980. **42**(0): p. 161-171.

26.	Olefjord, I. and L. Wegrelius, *Surface analysis of passive state.* Corrosion Science, 1990. **31**(0): p. 89-98.

27.	Wanklyn, J.N., *The role of molybdenum in the crevice corrosion of stainless steels.* Corrosion Science, 1981. **21**(3): p. 211-225.

28.	Sugimoto, K. and Y. Sawada, *The role of molybdenum additions to austenitic stainless steels in the inhibition of pitting in acid chloride solutions.* Corrosion Science, 1977. **17**(5): p. 425-445.

29.	Yaniv, A.E., J.B. Lumsden, and R.W. Staehle, *The composition of passive films on ferritic stainless steels.* Journal of Electrochemical Society, 1977. **124**(490).

30.	Exartier, C., S. Maximovitch, and B. Baroux, *Streaming potential measurements on stainless steels surfaces: evidence of a gel-like layer at the steel/electrolyte interface.* Corrosion Science, 2004. **46**(7): p. 1777-1800.

31.	Bruzzoni, P. and R. Garavaglia, *Anodic iron oxide films and their effect on the hydrogen permeation through steel.* Corrosion Science, 1992. **33**(11): p. 1797-1807.

32.	Hakiki, N.B., et al., *The electronic structure of passive films formed on stainless steels.* Corrosion Science, 1995. **37**(11): p. 1809-1822.

33.	Sakashita, M. and N. Sato, *The effect of molybdate anion on the ion-selectivity of hydrous ferric oxide films in chloride solutions.* Corrosion Science, 1977. **17**(6): p. 473-486.

34.	Newman, R.C. and T. Shahrabi, *The effect of alloyed nitrogen or dissolved nitrate ions on the anodic behaviour of austenitic stainless steel in hydrochloric acid.* Corrosion Science, 1987. **27**(8): p. 827-838.

35.	Lu, Y.C., M.B. Ives, and C.R. Clayton, *Synergism of alloying elements and pitting corrosion resistance of stainless steels.* Corrosion Science, 1993. **35**(1–4): p. 89-96.

36.	Addari, D., B. Elsener, and A. Rossi, *Electrochemistry and surface chemistry of stainless steels in alkaline media simulating concrete pore solutions.* Electrochimica Acta, 2008. **53**(27): p. 8078-8086.

37.	Vago, E.R., E.J. Calvo, and M. Stratmann, *Electrocatalysis of oxygen reduction at well-defined iron oxide electrodes.* Electrochimica Acta, 1994. **39**(11–12): p. 1655-1659.

38.	Le Bozec, N., et al., *Influence of stainless steel surface treatment on the oxygen reduction reaction in seawater.* Corrosion Science, 2001. **43**(4): p. 765-786.

39.	Yongjun, M.T. and R.R. Winston, *Heterogeneous Electrode Processes and Localized Corrosion*, ed. J.W. Sons. 2012. 264.

40.	Wilde, B.E. and E. Williams, *The use of current/voltage curves for the study of localized corrosion and passivity breakdown on stainless steels in chloride media.* Electrochimica Acta, 1971. **16**(11): p. 1971-1985.

41.	Suleiman, M.I., I. Ragault, and R.C. Newman, *The pitting of stainless steel under a rust membrane at very low potentials.* Corrosion Science, 1994. **36**(3): p. 479-486.

42. Kain, R.M., A.H. Tuthill, and E.C. Hoxie, *The resistance of types 304 and 316 stainless steels to crevice corrosion in natural waters.* Journal of Materials for Energy Systems, 1984. **5**(4): p. 205-211.

43. Wilde, B.E., *A relationship between steady-state corrosion potential and the anodic dissolution kinetics of the 300 series austenitic stainless steels.* Corrosion Science, 1967. **7**(6): p. 315-324.

44. Nisancioglu, K., *Corrosion basics and engineering,* N.U.o.S.a. Technology, Editor 2011, Norwegian University of Science and Technology.

45. Williams, D., C. Westcott, and M. Fleischmann, *Stochastic Models of Pitting Corrosion of Stainless Steels I. Modeling of the Initiation and Growth of Pits at Constant Potential.* Journal of the Electrochemical Society, 1985. **132**(8): p. 1796-1804.

46. Laws, M.S. and P.J. Goodhew, *Grain boundary structure and chromium segregation in a 316 stainless steel.* Acta Metallurgica et Materialia, 1991. **39**(7): p. 1525-1533.

47. Pagano, M.A. and S.B. Lalvani, *Corrosion of mild steel subjected to alternating voltages in seawater.* Corrosion Science, 1994. **36**(1): p. 127-140.

48. Hagen, C.H.M., *A comparative study of AC-induced corrosion of X65 Carbon Steel and 316L Stainless Steel in 3.5 wt% NaCl electrolyte,* 2012, Norwegian University of Science and Technology: Trondheim. p. 86.

49. Bosch, R.W. and W.F. Bogaerts, *A theoretical study of AC-induced corrosion considering diffusion phenomena.* Corrosion Science, 1998. **40**(2–3): p. 323-336.

50. Yunovich, M., *AC Corrosion State-of-the-Art: Corrosion Rate, Mechanism, and Mitigation Requirements* T.G. 327, Editor 2010: Houston.

51. Zhang, R., P.R. Vairavanathan, and S.B. Lalvani, *Perturbation method analysis of AC-induced corrosion.* Corrosion Science, 2008. **50**(6): p. 1664-1671.

52. Oldham, K.B., *Faradaic rectification: theory and application to the Hg22+/Hg electrode.* Transactions of the Faraday Society, 1957. **53**(0): p. 80-90.

53. Hosokawa, Y., F. Kajiyama, and T. Fukuoka, *Alternating Current Corrosion Risk Arising from Alternating Current-Powered Rail Transit Systems on Cathodically Protected Buried Steel Pipelines and Its Measures.* Corrosion - The journal of science and engineering, 2004. **60**(4): p. 200.

54. Baranski, A.S. and A. Boika, *Effect of large-amplitude alternating current modulation on apparent reversibility of electrode processes.* Anal Chem, 2010. **82**(19): p. 8137-45.

55. Goidanich, S., L. Lazzari, and M. Ormellese, *AC corrosion – Part 1: Effects on overpotentials of anodic and cathodic processes.* Corrosion Science, 2010. **52**(2): p. 491-497.

56. Hirschorn, B., et al., *Effect of Large Perturbation Amplitudes on the Impedance Response of an Electrochemical System.* ECS Transactions, 2008. **13**(13): p. 81-100.

57. Xu, L.Y., et al., *Development of a real-time AC/DC data acquisition technique for studies of AC corrosion of pipelines.* Corrosion Science, 2012. **61**(0): p. 215-223.

58. Stamnes, I., *AC corrosion of pipe line steel,* in Department of Materials Science and Engineering 2010, Norwegian University of Science and Technology: Trondheim. p. 125.

59. Xu, L.Y., X. Su, and Y.F. Cheng, *Effect of alternating current on cathodic protection on pipelines.* Corrosion Science, 2013. **66**(0): p. 263-268.

60. Juchniewicz, R., *Influence of the alternating current on anodic protection.* Corrosion Science, 1962. **2**: p. 225.

61. Juchniewicz, R., *The influence of alternating current on the anodic behavior of platinum.* Platinum Metals review, 1962. **6**(1962): p. 100-105.

62. *Benke, G. and W. Gnot, The electrochemical dissolution of platinum. Hydrometallurgy, 2002. **64**(3): p. 205-218.*

63. *Wendt, J.L. and D.T. Chin, The a.c. corrosion of stainless steel—II. The breakdown of passivity of ss304 in neutral aqueous solutions. Corrosion Science, 1985. **25**(10): p. 889-900.*

64. *Hesjevik, S.M., S. Olsen, and L.S. Lilleby, Effects from alternating current on cathodic protection of submarine pipelines, in Corrosion 20112011, NACE International (NACE).*

65. *Nielsen, L.V., et al., AC Induced Corrosion in Pipelines: Detection, Characterization and Mitigation. CORROSION 2004, 2004.*

66. *Kim, D.-K., et al., Electrochemical studies on the alternating current corrosion of mild steel under cathodic protection condition in marine environments. Electrochimica Acta, 2006. **51**(25): p. 5259-5267.*

67. *Fu, A.Q. and Y.F. Cheng, Effects of alternating current on corrosion of a coated pipeline steel in a chloride-containing carbonate/bicarbonate solution. Corrosion Science, 2010. **52**(2): p. 612-619.*

68. *ASTM, ASTM International G31-72(2004) "Standard Practice for Laboratory Immersion Corrosion Testing of Metals", 2004: West Conshohocken.*

69. *ASTM, ASTM International G46-94(2005) "Standard Guide for Examination and Evaluation of Pitting Corrosion", 2005: West Conshohocken.*

70. *ASTM, ASTM International G1-03 "Standard Practice for Preparing, Cleaning, and Evaluating Corrosion Test Specimens", 2011: West Conshohocken.*

71. *DNV, Offshore Standard DNV-OS-F101, in Submarine Pipeline Systems2012, Det Norske Veritas AS: Norway. p. 367.*

72. *Bockris, J.O.M., D. Drazic, and A.R. Despic, The electrode kinetics of the deposition and dissolution of iron. Electrochimica Acta, 1961. **4**(2–4): p. 325-361.*

73. *Hettiarachchi, S., Evaluation of corrosion rates by the faradaic rectification method. Corrosion Science, 1981. **21**(7): p. 531-539.*

APPENDICES

Appendix A Calculations

The information in this appendix presents the calculation techniques used to evaluate the data gathered and reported in this thesis. In Table A, information can be found about the fundamental constants and physical data used for the calculations.

Table A: Physical data used for calculations in this report.

Parameter	Value	Unit
Faraday constant, F	96485	C/mol
Steel density, ρ	7.9	g/cm^3
Steel molar weight, M	55.8	g/mol

A.1 Corrosion rates

The average corrosion rate (CR) in mm/y over the exposure duration was determined from before and after specimen weight measurements using the expression with a constant k equal to 8.76 *10^4:

$$CR = \frac{k * \Delta w}{\rho * A * t} \tag{A.1}$$

Corrosion current densities are calculated by reorganizing the equation as seen in:

$$i_{corr}^{WL} = \frac{\Delta w * n * F}{A * t} \tag{A.2}$$

Where:
Δw difference in weight   [g]
ρ steel density   [g/cm^3]
A sample area   [cm$^{2]}$
t exposure time   [h]

A.2 Current response

From the recorded current response during cathodic and anodic polarization, and from the calculated corrosion current densities based on weight loss measurements – the reduction current density associated with the specific applied AC density, could be calculated.

During polarization where steel makes the working electrode (WE) and the counter electrode (CE) is a platinum (Pt) plate, by employment of mixed potential theory:

$$\sum I_{ox} = \sum \left| I_{red} \right| \tag{A.3}$$

The current response is thus:

$$I_{net} = I_{ox,metal} - \left| I_{red,metal} \right| \tag{A.4}$$

Positive values of I_{net} will indicate that the oxidation reaction on the metal dominates the reduction reaction, and vice versa for negative values of I_{net}. From the equation above, the reduction current densities are calculated straightforward.

A.3 Calculation of charge, Q

From the positive currents that developed on X65 the charge was calculated by numerical integration. The numerical integration was performed by the Trapezoidal rule over the time integral [a,b] where Q [As] is given by:

$$Q = \int I * dt \tag{A.5}$$

and the numerical integration is given by:

$$\int_{a}^{b} I * dt \approx Q_0 + \frac{b-a}{2} * \left(I_1 + I_2 \right) \tag{A.6}$$

A.4 Corrosion parameters

Polarization curves recorded on X65 and 25Cr when plotted, were corrected for the potential drop due to resistance in the electrolyte, R_s , by tuning the resistance until lines visually showed increased linearity:

$$E_{corrected} = E_{measured} - \left| IR \right| \tag{A.7}$$

From polarization curves several corrosion parameters could be extracted. When mixed potential theory is to be obeyed, the relationship between cathodic and anodic currents is at open circuit potential given by:

$$I_{net} = I_{cathodic} + I_{anodic} = 0, \quad at \ E_{corr} \tag{A.8}$$

From the equation it follows that :

$$i_{corr} = i_{O2\_lim} + i_H \tag{A.9}$$

Corrosion current densities were by this determined from intersection of tangents to anodic and cathodic curves, a method called Tafel extrapolation.

Appendix B Reproducibility

The reproducibility of results was investigated when the experimental procedure was planned.

A weight loss measurement for 316L at an applied alternating current density of 1000 A/m^2 was compared with results achieved at E_{OC} during the project study (NTNU, 2012) [48].

As it can be seen from Figure 67, the result fitted the previous achieved and it was therefore concluded that the developed experimental procedure was suited for collection of new experimental data.
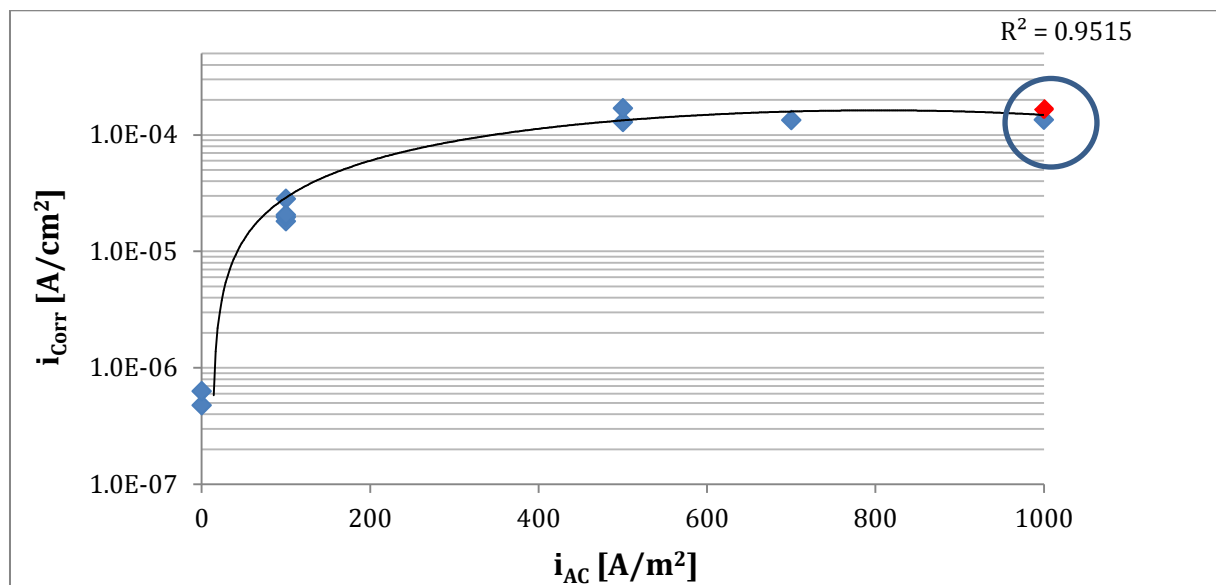

Figure 67: Plot of weight loss data achieved during the autumn project and from an experiment performed this spring. The data fitting harmonizes with earlier results.

Appendix C AISI 316L SS

C.1 Weight loss

To correct for additional weight losses related to the removal of corrosion products, un-corroded samples were tested as described in ASTM G1-03[70]. It was found that 316L remained unaffected. The steel showed no mass loss due to the chemical removal step and all mass losses recorded after experiments for this steel type are therefore actual losses due to corrosion of the material during the experiments. Table C.1.1 shows the results from weight loss measurements for samples tested at -800 mV while Table C.1.2 shows results for similar tests at -1050 mV.

Table C.1.1: Results from weight loss measurements at -800 mV when samples have been tested for 72-96 hours for increasing AC densities. Experiments for samples tested at 0 A/cm² AC lasted 96 hours to ensure stabilization of values.

i_{AC} [A/m²]	Δm_{corr} [mg]	$\overline{\Delta m}_{corr}$ [mg]	i_{corr}^{WL} [A/cm²]	$\bar{i}_{corr}^{WL}$ [A/cm²]	CR^{WL} [mmy]	$\overline{CR}^{WL}$ [mmy]
0	0.067	0.164	1.01E-07		1.18E-03	0.003
0	0.325		4.95E-07	2.50E-07	5.76E-03	
0	0.100		1.52E-07		1.77E-03	
100	0.325	0.350	6.60E-07	7.11E-07	7.68E-03	0.008
100	0.375		7.62E-07		8.86E-03	
500	1.17	1.27	2.37E-06		2.76E-02	0.030
500	2.59		5.27E-06	2.58E-06	6.12E-02	
500	0.050		1.02E-07		1.18E-03	
1000	2.95	1.89	1.51E-05		1.76E-01	0.113
1000	0.183		9.40E-07	9.69E-06	1.09E-02	
1000	2.53		1.30E-05		1.51E-01	

Table C.1.2: Results from weight loss measurements at -1050 mV when samples have been tested for 72-96 hours for increasing AC densities. Experiments for samples tested at 0 A/cm² AC lasted 96 hours to ensure stabilization of values.

i_{AC} [A/m²]	Δm_{corr} [mg]	$\overline{\Delta m}_{corr}$ [mg]	i_{corr}^{WL} [A/cm²]	$\bar{i}_{corr}^{WL}$ [A/cm²]	CR^{WL} [mmy]	$\overline{CR}^{WL}$ [mmy]
0	0.567	0.496	8.64E-07	7.56E-07	1.00E-02	0.009
0	0.833		1.27E-06		1.48E-02	
0	0		0		0.00E+00	
0	0.583		8.89E-07		1.03E-02	
100	0.300	0.275	6.10E-07	5.59E-07	7.09E-03	0.007
100	0.500		1.02E-06		1.18E-02	
100	0.033		6.77E-08		7.88E-04	
100	0.267		5.42E-07		6.30E-03	
500	0.725	0.396	1.47E-06	8.04E-07	1.71E-02	0.009

500	0.067		1.35E-07		1.58E-03	
1000	0.533	0.400	2.73E-06	2.05E-06	3.18E-02	0.024
1000	0.267		1.37E-06		1.59E-02	

Figure 68 shows the calculated corrosion current densities for all parallels based on obtained weight losses during cathodic polarization experiments at -800 mV and -1050 mV.
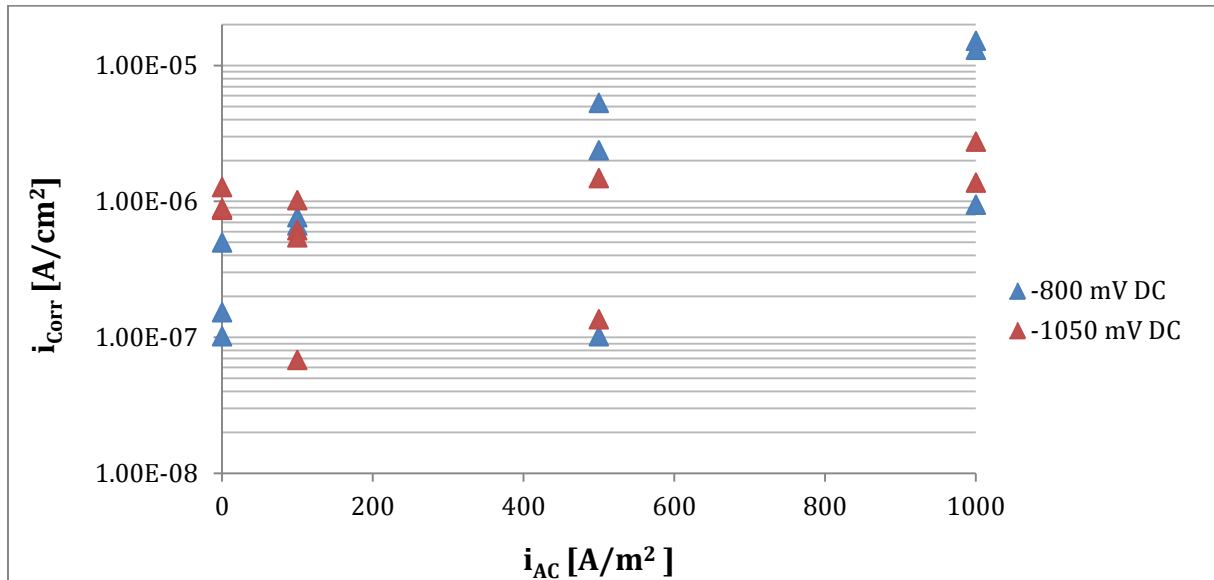

Figure 68: Corrosion current densities for all parallels of 316L as calculated from weight losses when increasing AC current densities are applied.

C.2 Polarization behavior

Figure 69 shows calculated values for $|i_{red}|$ based on obtained values for i_{NET} during the cathodic polarization of 316L, for all parallels.
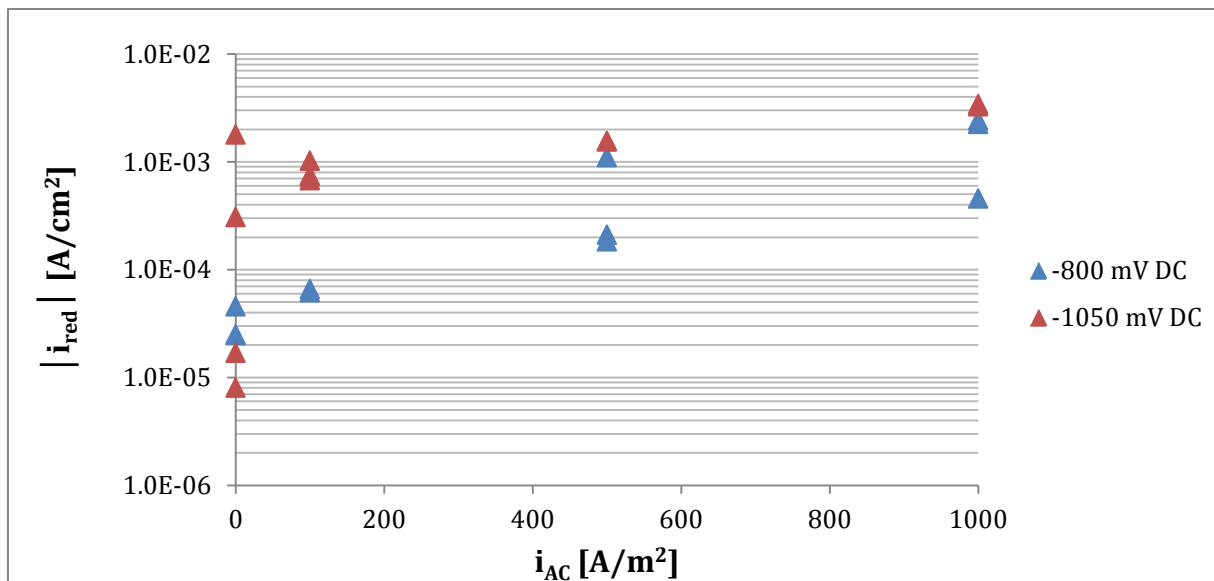

Figure 69: Calculated values for cathodic partial current densities for densities for all parallels of 316L during 72-96 hours of testing when increasing AC densities are applied under cathodic DC potentials

C.2.1 Results for samples polarized potentiostatically at -800 mV

Table C.2.1 shows averaged current response values for all parallels and averaged values for the experiments at -800 mV. In addition all calculated $|i_{red}|$ values for the parallels and average values for the experiments are given. Figure 70-Figure 73 depict the current response as a function of time for all parallels.

Table C.2.1: Results from potentiostatic polarization at -800 mV when samples have been tested for 72-96 hours for increasing AC densities. Experiments for samples tested at 0 A/cm² AC lasted 96 hours to ensure stabilization of values.

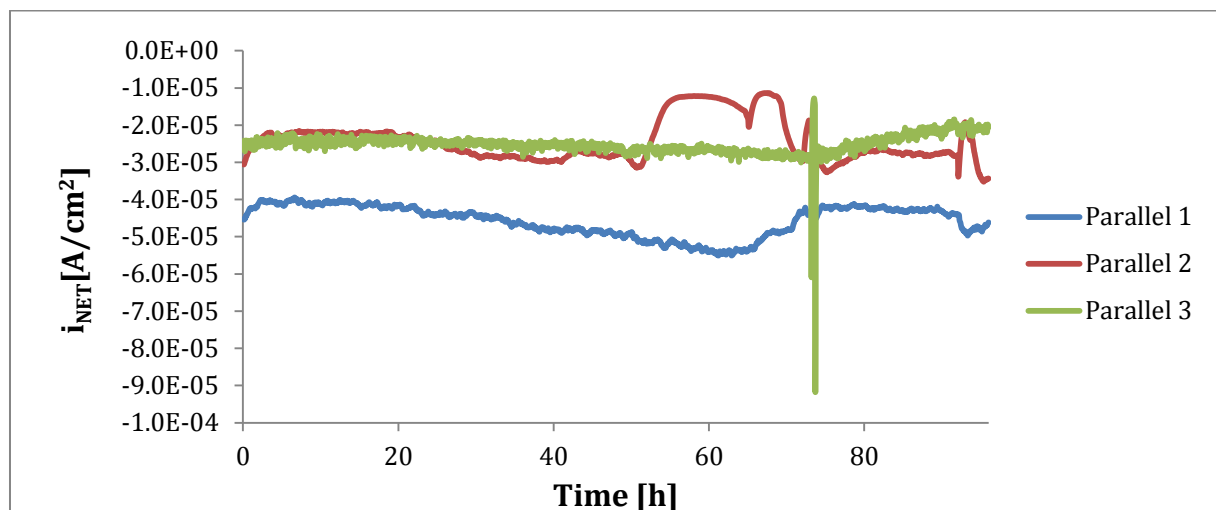| i_{AC} [A/m²]	$i_{NET} \left[A/cm^2 \right]$	$\bar{i}_{NET} \left[A/cm^2 \right]$	$\mid i_{red} \mid \left[A/cm^2 \right]$	$\mid \bar{i}_{red} \mid \left[A/cm^2 \right]$
0	-4.57E-05		4.58E-05	
0	-2.42E-05	-3.16E-05	2.47E-05	3.19E-05
0	-2.49E-05		2.50E-05	
100	-6.12E-05		6.17E-05	
100	-6.52E-05	-6.32E-05	6.59E-05	6.39E-05
500	-1.80E-04		1.83E-04	
500	-1.10E-03	-4.98E-04	1.11E-03	5.01E-04
500	-2.12E-04		2.12E-04	
1000	-2.41E-03		2.43E-03	
1000	-4.56E-04	-1.70E-03	4.57E-04	1.71E-03
1000	-2.23E-03		2.25E-03	

Figure 70: Recorded current density responses for experiments on 316L under cathodic potentiostatic polarization at -800 mV for samples tested 96 hours at 0 A/m² AC.
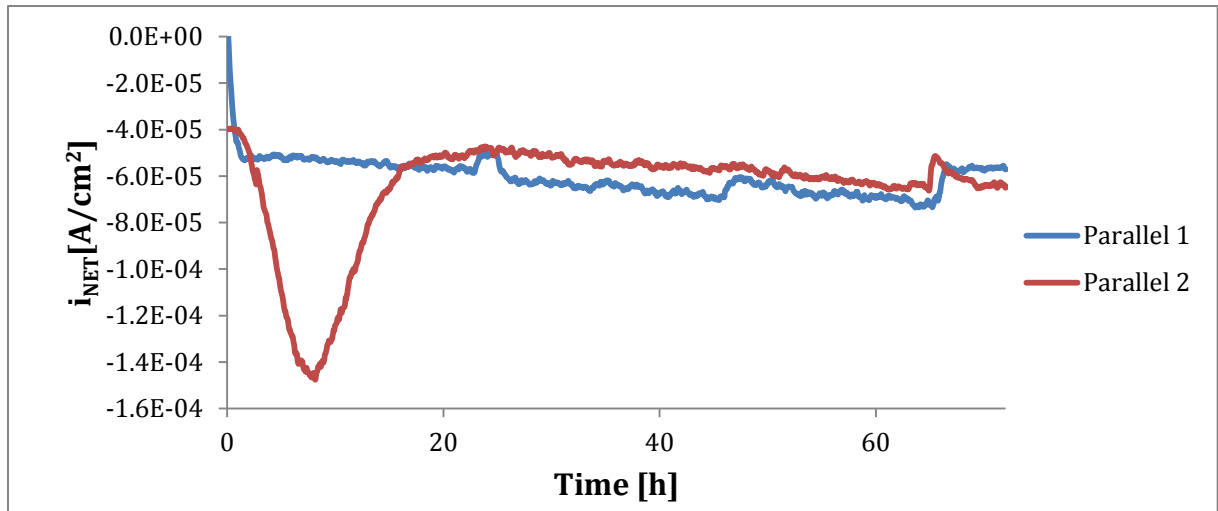
Figure 71: Recorded current density responses for experiments on 316L under cathodic potentiostatic polarization at -800 mV for samples tested 72 hours at 100 A/m^2 AC.
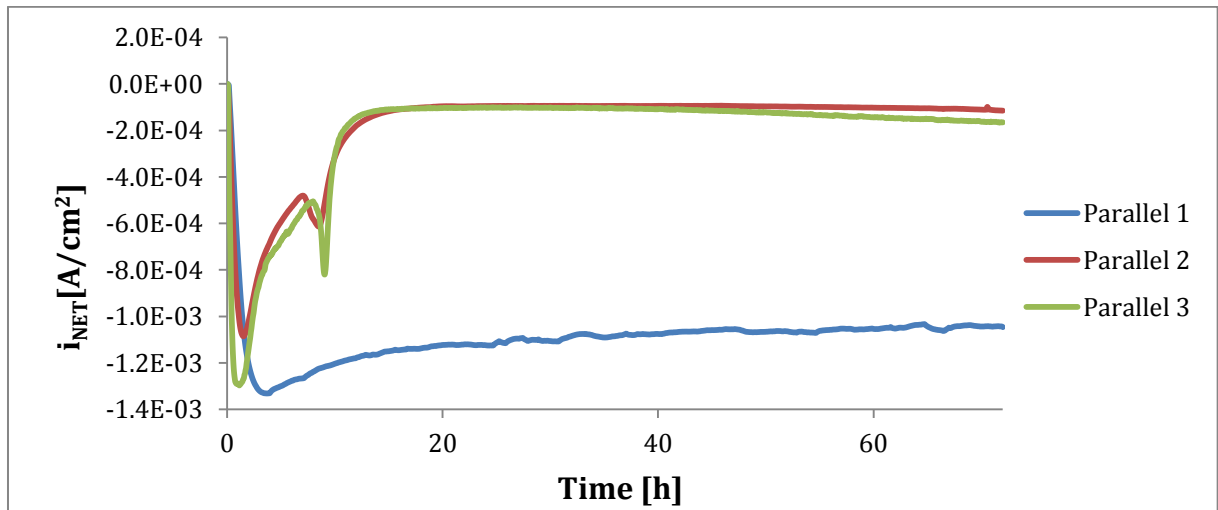

Figure 72: Recorded current density responses for experiments on 316L under cathodic potentiostatic polarization at -800 mV for samples tested 72 hours at 500 A/m^2 AC.
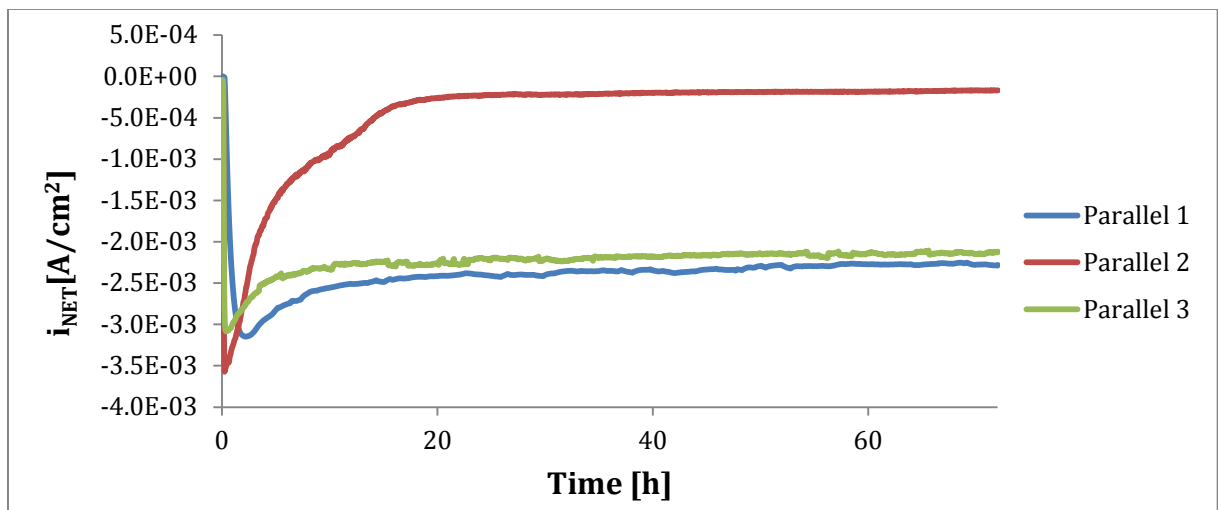

Figure 73: Recorded current density responses for experiments on 316L under cathodic potentiostatic polarization at -800 mV for samples tested 72 hours at 1000 A/m^2 AC.

C.2.2 Results for samples polarized potentiostatically at -1050 mV

Table C.2.2 shows averaged current response values for all parallels and averaged values for the experiments at -1050 mV. In addition all calculated $|i_{red}|$ values for the parallels and average values for the experiments are given. Figure 74-Figure 77 depict the current response as a function of time for all parallels.

Table C.2.2: Results from potentiostatic polarization at -1050 mV when samples have been tested for 72-96 hours for increasing AC densities. Experiments for samples tested at 0 A/cm² AC lasted 96 hours to ensure stabilization of values.

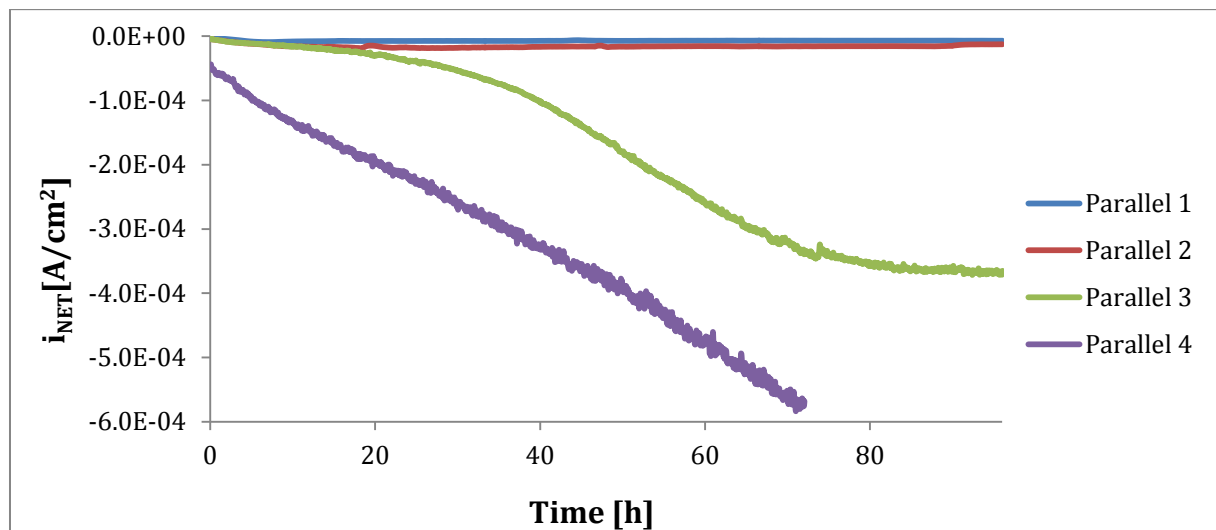| i_{AC} [A/m²]	$i_{NET}\left[A/cm^2\right]$	$\bar{i}_{NET}\left[A/cm^2\right]$	$\lvert i_{red}\rvert\left[A/cm^2\right]$	$\lvert\bar{i}_{red}\rvert\left[A/cm^2\right]$
0	-1.57E-05		1.70E-05	
0	-7.20E-06		8.07E-06	
0	-1.80E-03		1.80E-03	
0	-3.08E-04	-5.32E-04	3.09E-04	5.32E-04
100	-1.03E-03		1.03E-03	
100	-6.74E-04		6.75E-04	
100	-7.48E-04		7.49E-04	
100	-7.34E-04	-7.96E-04	7.35E-04	7.96E-04
500	-1.57E-03		1.57E-03	
500	-1.54E-03	-1.55E-03	1.54E-03	1.55E-03
1000	-3.43E-03		3.43E-03	
1000	-3.27E-03	-3.35E-03	3.27E-03	3.35E-03

Figure 74: Recorded current density responses for experiments on 316L under cathodic potentiostatic polarization at -1050 mV for samples tested 96 hours at 0 A/m² AC.
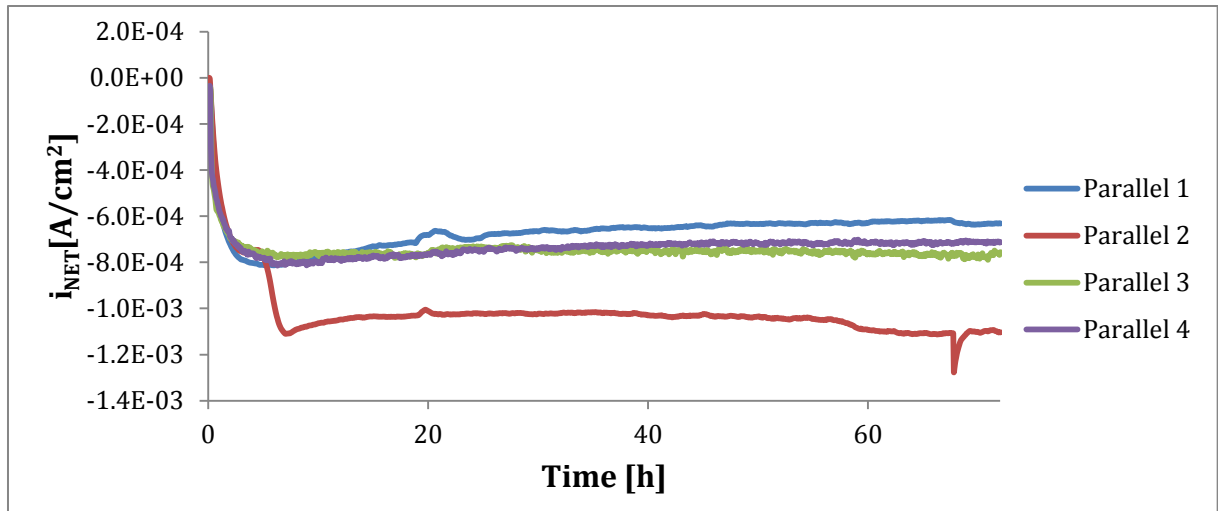
Figure 75: Recorded current density responses for experiments on 316L under cathodic potentiostatic polarization at -1050 mV for samples tested 72 hours at 100 A/m^2 AC.
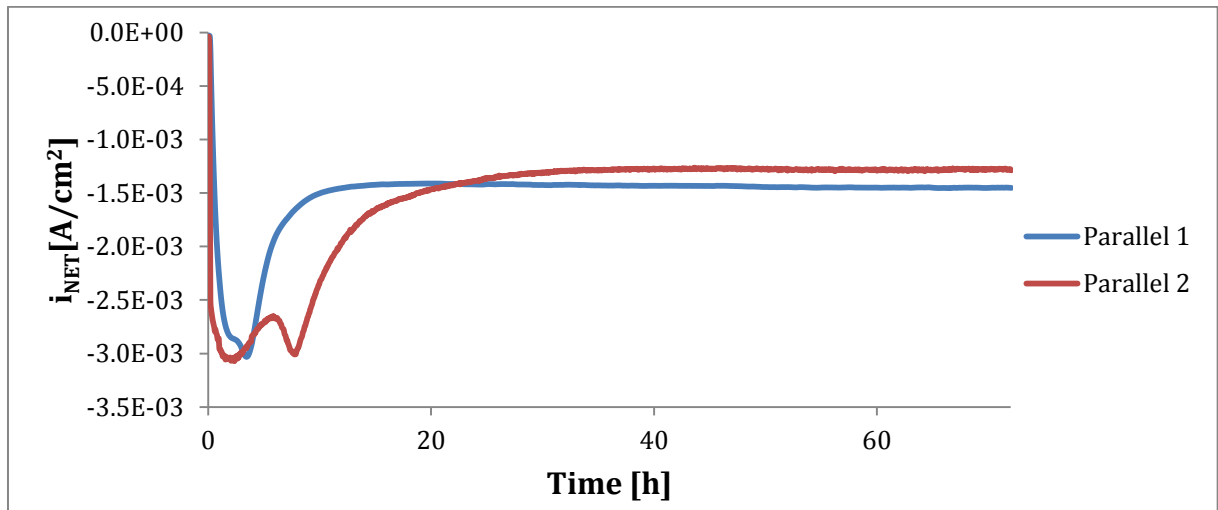

Figure 76: Recorded current density responses for experiments on 316L under cathodic potentiostatic polarization at -1050 mV for samples tested 72 hours at 500 A/m^2 AC.
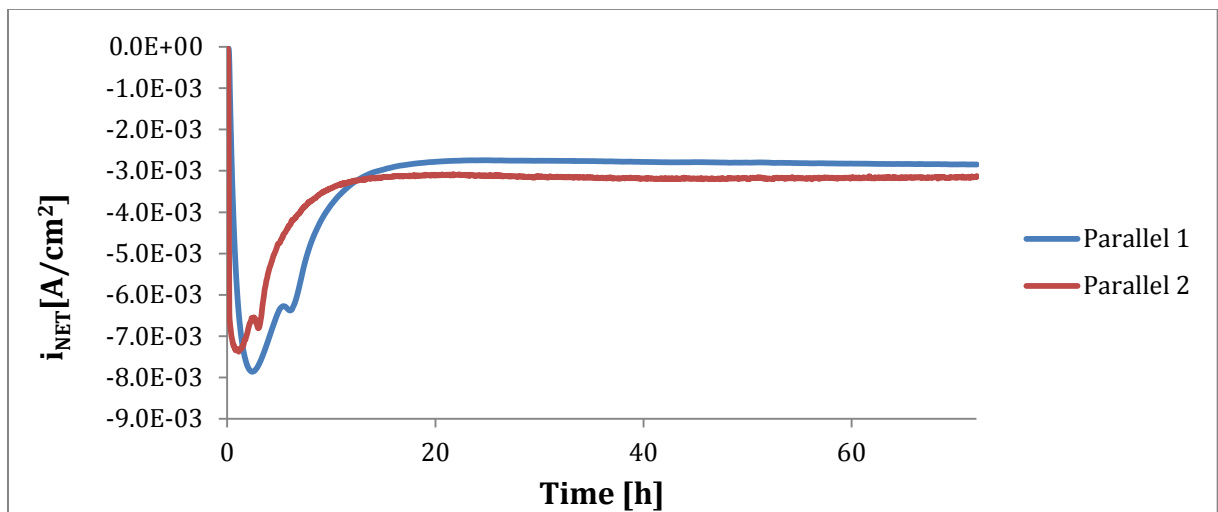

Figure 77: Recorded current density responses for experiments on 316L under cathodic potentiostatic polarization at -1050 mV for samples tested 72 hours at 1000 A/m^2 AC.

C.3 Surface morphology

In the following chapter SEM micrographs recorded at 500X magnification are presented together with results from an EDS analysis for samples tested with applied AC.

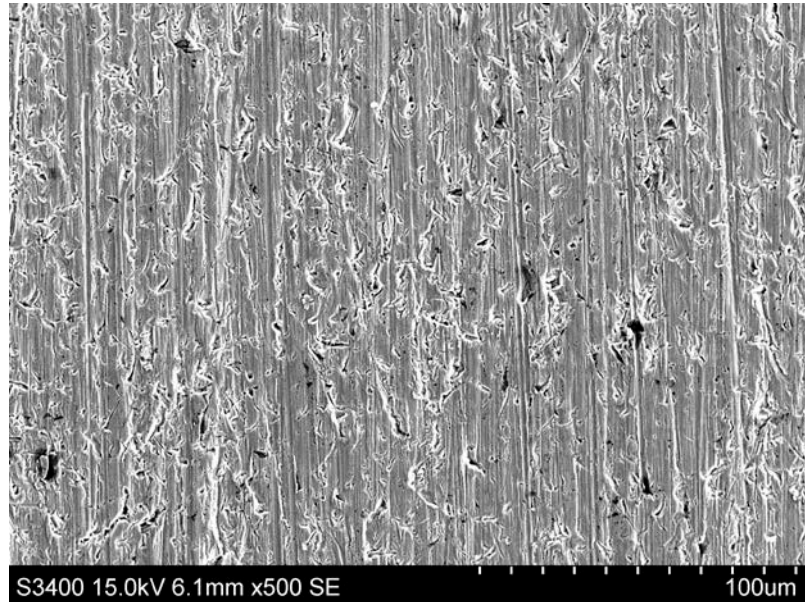### *C.3.1 SEM analysis for samples polarized potentiostatically at -800 mV*

Figure 78: SEM micrograph of surface on 316L sample tested at -800 mV DC and 0 A/m^{2}AC. Seen at 500X magnification.
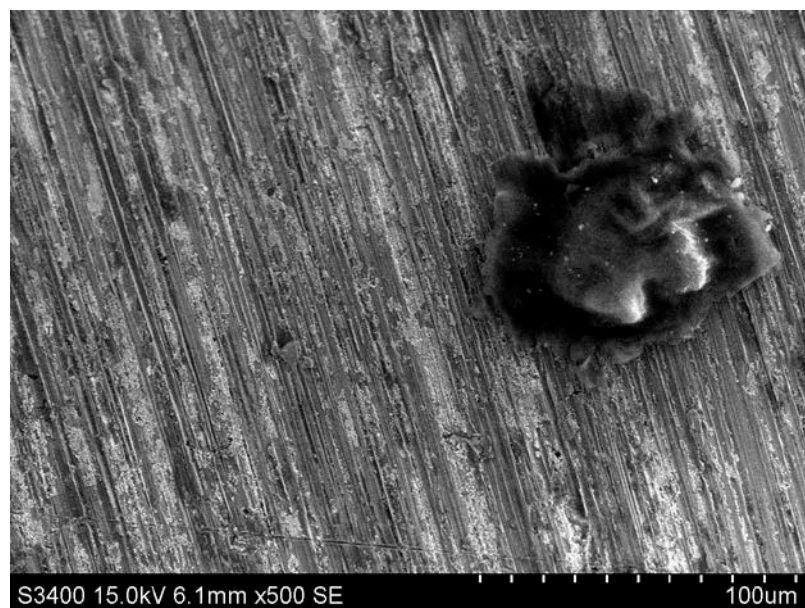

Figure 79: SEM micrograph of surface on 316L sample tested at -800 mV and 100 A/m^{2}A . Seen at 500X magnification.
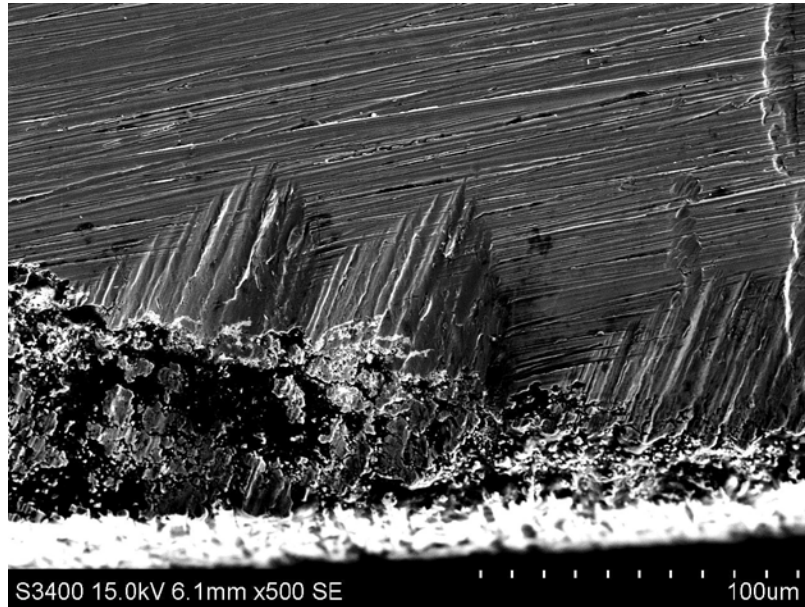
Figure 80: SEM micrograph of surface on 316L sample tested at -800 mV and 500 A/m²AC. Seen at 500X magnification.
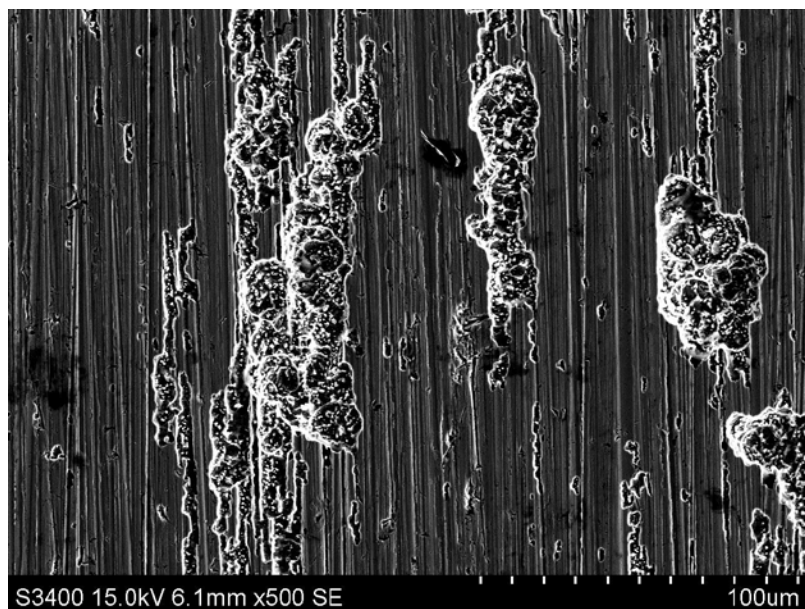

Figure 81: SEM micrograph of surface on 316L sample tested at -800 mV DC and 1000 A/m²AC. Seen at 500X magnification.

C.3.2 SEM analysis for samples polarized potentiostatically at -1050 mV
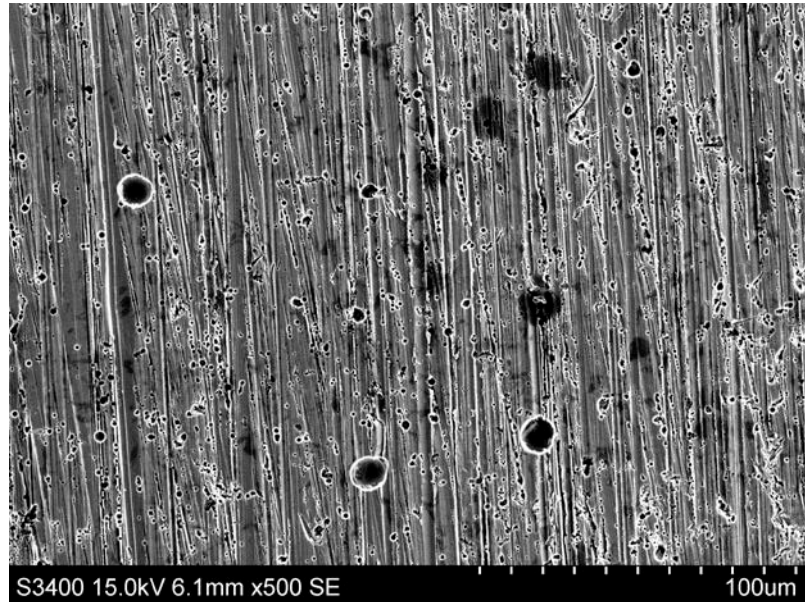

Figure 82: SEM micrograph of surface on 316L sample tested at -1050 mV and 0 A/m^{2}AC. Seen at 500X magnification.
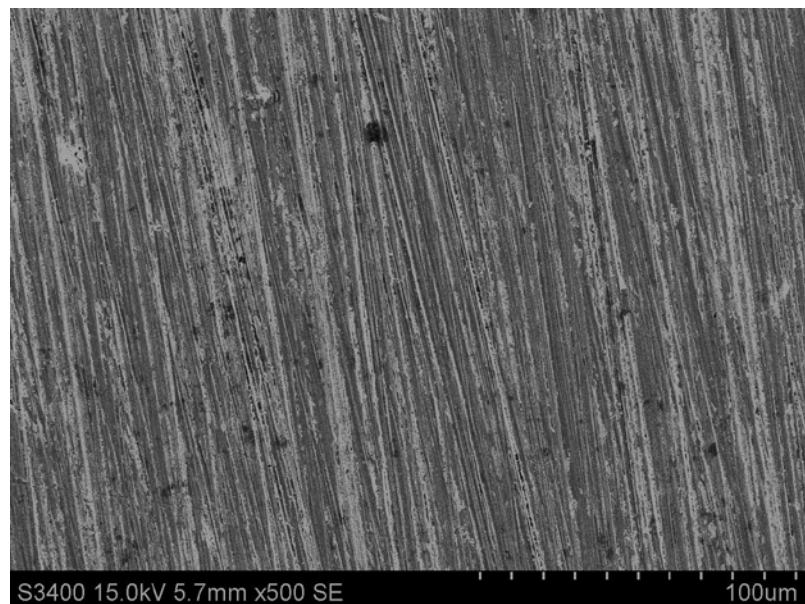

Figure 83: SEM micrograph of surface on 316L sample tested at -1050 mV and 100 A/m^{2}AC. Seen at 500X magnification.
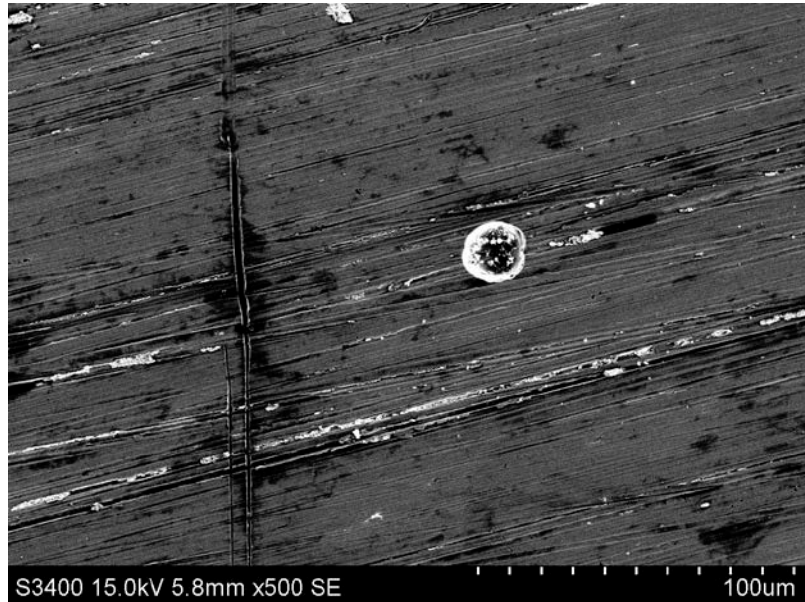
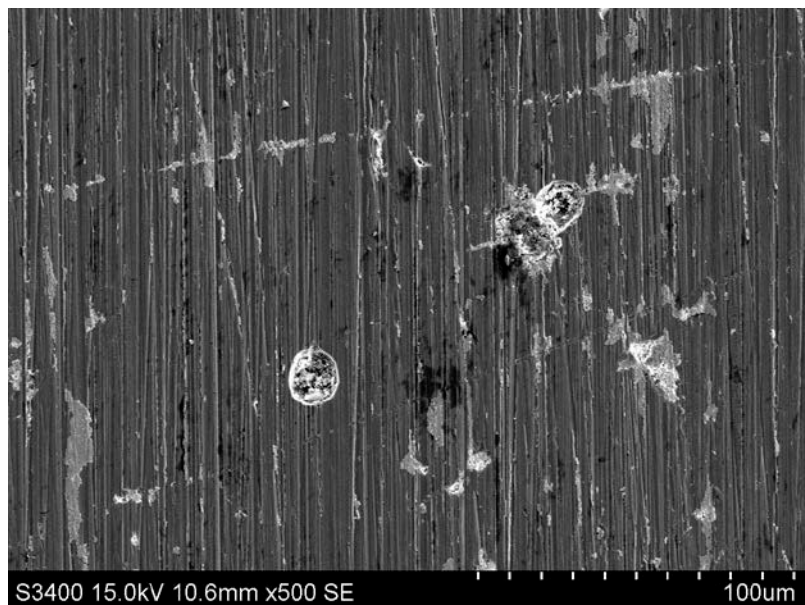**Figure 84: SEM micrograph of surface on 316L sample tested at -1050 mV and 500 A/m^{2}AC. Seen at 500X magnification.**

Figure 85: SEM micrograph of surface on 316L sample tested at -1050 mV and 1000 A/m^{2}AC. Seen at 500X magnification.

C.3.3 EDS analysis for samples polarized potentiostatically at -800 mV
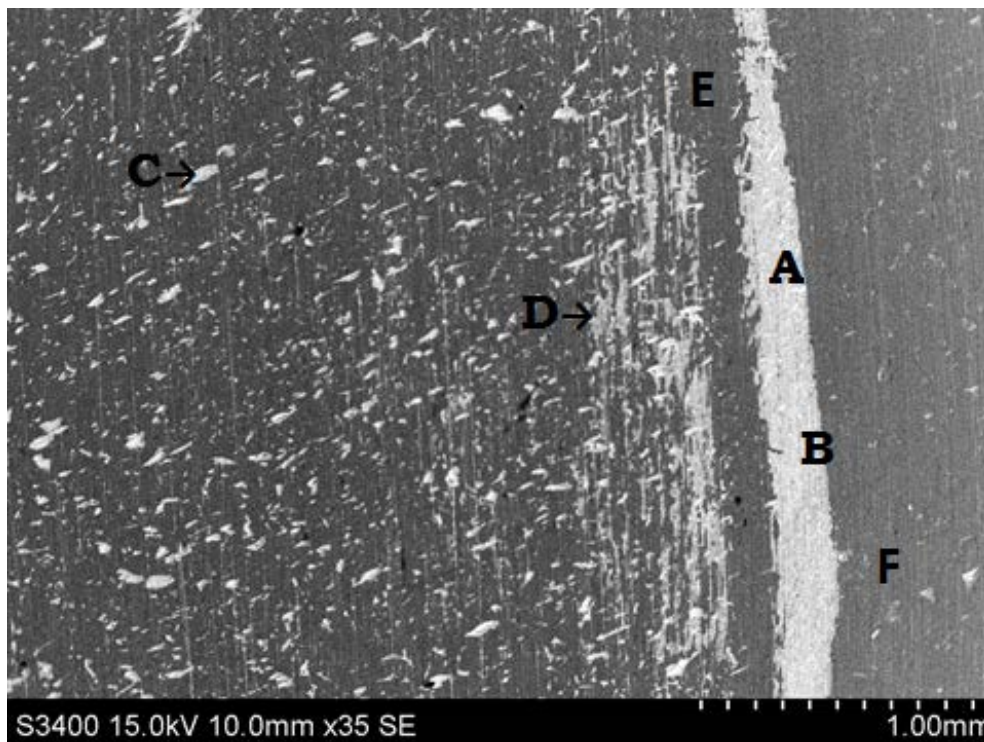
Figure 86: SEM micrograph of non-soluble products on sample tested at -800 mV and an applied AC density of 100 A/m^2. The regions studied in the EDS analysis are marked with letters.

Table C.3.3.1: EDS study of non-soluble products identified on sample tested at -800 mV and an applied AC density of 100 A/m^2. The chemical composition of the surface free of products has also been analyzed.

|	O	Si	Cr	Mn	Fe	Ni	Mo	Pt
Spectrum A	0	0	3.97	0	15.72	1.89	0	78.42
Spectrum B	0	0	3.29	0	12.21	1.71	0	82.79
Spectrum C	0	0	8.26	0.85	30.11	4.04	0	56.74
Spectrum D	0	0	5.86	0	23.37	3.48	0	67.3
Average	0	0	5.34	0.21	20.35	2.78	0	71.31
Standard Deviation	0	0	2.22	0.42	8	1.16	0	11.7
Spectrum E	0	0.2	16.82	1.37	68.36	10.21	2.21	0
Spectrum F	5.42	0.34	16.08	1.32	64.45	9.98	2.42	5.42
Average	2.71	0.27	16.45	1.35	66.4	10.09	2.32	2.71
Standard Deviation	3.84	0.1	0.53	0.04	2.77	0.16	0.15	3.84
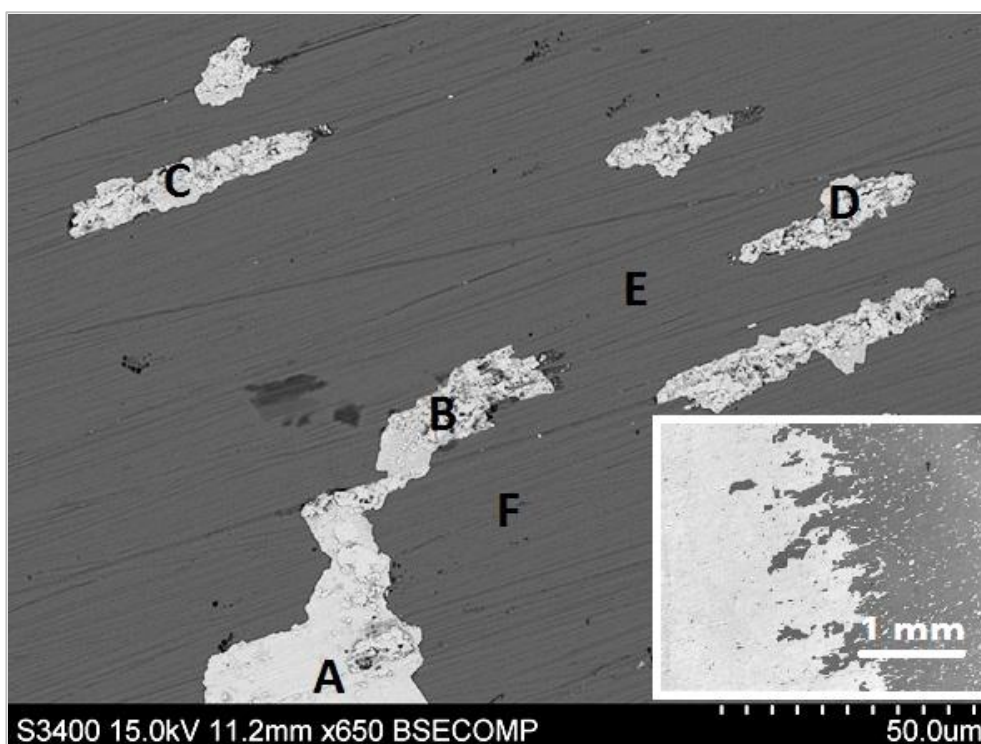
Figure 87: SEM micrograph of non-soluble products on sample tested at -800 mV and an applied AC density of 500 A/m². The regions studied in the EDS analysis are marked with letters.

Table C.3.3.2: EDS study of non-soluble products identified on sample tested at -800 mV and an applied AC density of 500 A/m². The chemical composition of the surface free of products has also been analyzed.

|	O	Si	Cr	Mn	Fe	Ni	Mo	Pt
Spectrum A	0	0	3.78	0	13.45	1.65	0	76.24
Spectrum B	0.65	0	4.57	0	15.14	2.2	0	67.58
Spectrum C	0.33	0	5.62	0.65	20.1	3	0	64.84
Spectrum D	1.37	0	1.4	0	4.26	0	0	76.38
Average	0.59	0	3.84	0.16	13.24	1.71	0	71.26
Standard Deviation	0.59	0	1.80	0.33	6.62	1.27	0	5.94
Spectrum E	0.56	0.31	16.78	1.29	66.45	9.94	1.95	0
Spectrum F	0.55	0.32	16.77	1.37	66.62	10.01	1.64	0
Average	0.56	0.32	16.77	1.33	66.54	9.97	1.79	0
Standard Deviation	0.01	0.01	0.01	0.05	0.12	0.05	0.22	0
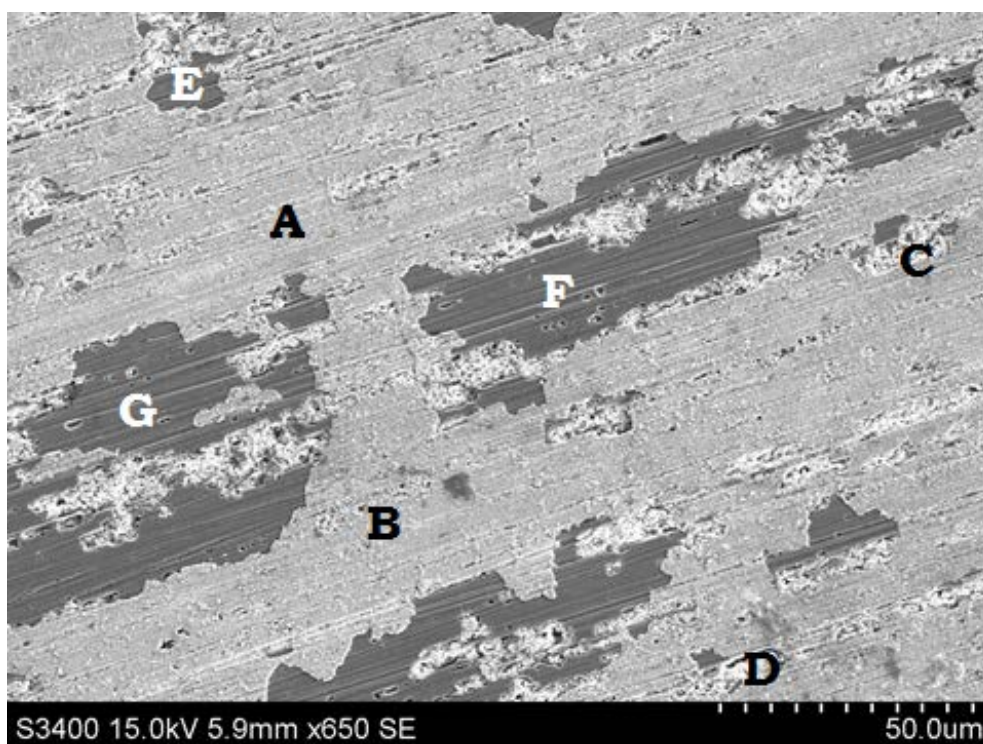
Figure 88: SEM micrograph of non-soluble products on sample tested at -800 mV and an applied AC density of 1000 A/m². The regions studied in the EDS analysis are marked with letters.

Table C.3.3.3: EDS study of non-soluble products identified on sample tested at -800 mV and an applied AC density of 1000 A/m². The chemical composition of the surface free of products has also been analyzed.

	O	Si	Cr	Mn	Fe	Ni	Mo	Pt
Spectrum A	1.41	0	8.61	0.66	28.74	4.1	0	56.48
Spectrum B	0.76	0	5.56	0	18.03	2.62	0	73.02
Spectrum C	2.04	0	8.81	0.69	32.68	4.5	0	51.27
Spectrum D	1.34	0	1.32	0	5.85	1.05	0	90.44
Average	1.39	0	6.08	0.34	21.33	3.07	0	67.8
Standard Deviation	0.52	0	3.5	0.39	12.03	1.57	0	17.71
Spectrum E	1.15	0.36	16.84	1.38	68.29	10.32	1.65	0
Sprectrum F	0.94	0.35	17.25	1.35	68.29	10.43	1.4	0
Spectrum G	0.89	0.3	17.19	1.76	68.01	9.92	1.93	0
Average	0.99	0.34	17.09	1.5	68.2	10.22	1.66	0
Standard Deviation	0.14	0.03	0.22	0.23	0.16	0.27	0.26	0

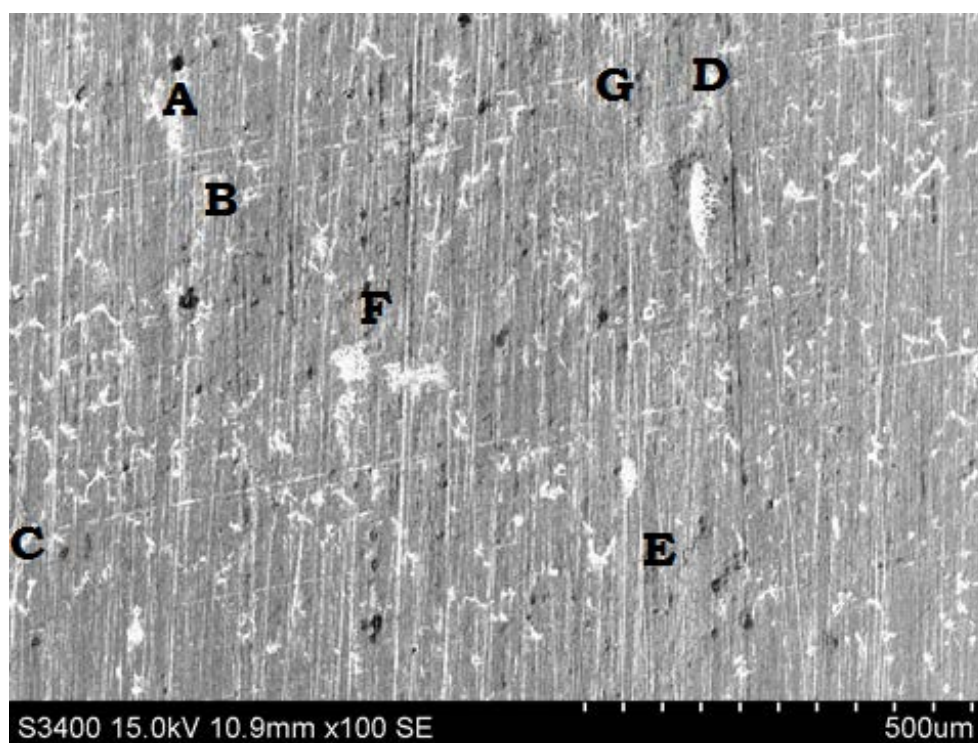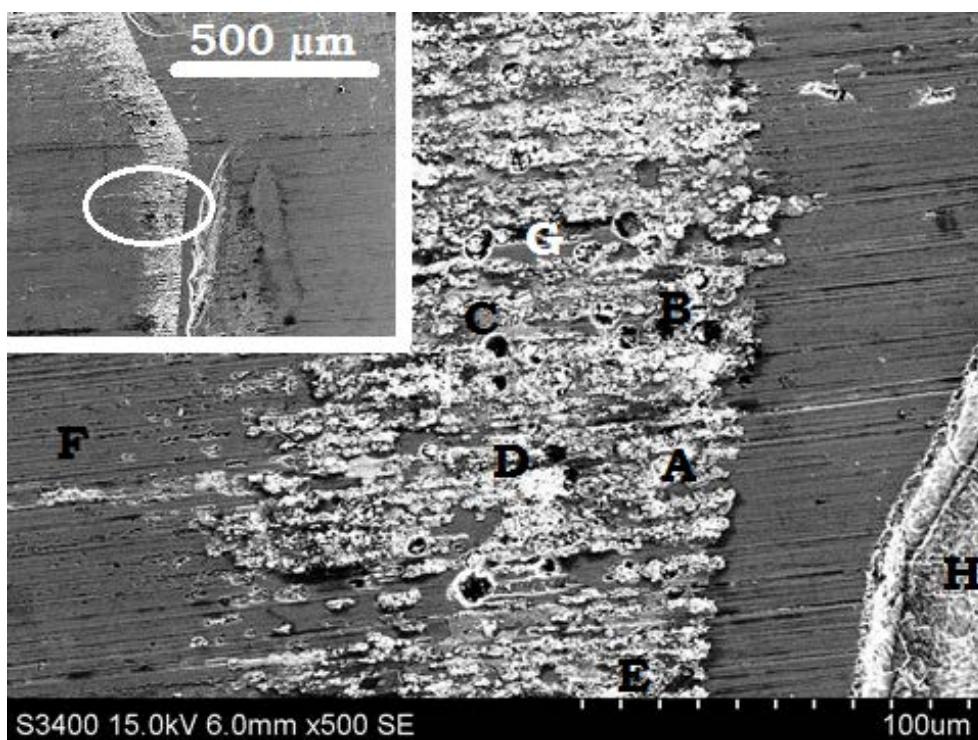## C.3.4 EDS analysis for samples polarized potentiostatically at -1050 mV

Figure 89: SEM micrograph of non-soluble products on sample tested at -1050 mV and an applied AC density of 100 A/m². The regions studied in the EDS analysis are marked with letters.

Table C.3.4.1: EDS study of non-soluble products identified on sample tested at -1050 mV and an applied AC density of 100 A/m². The chemical composition of the surface free of products has also been analyzed.

|	O	Si	Cr	Mn	Fe	Ni	Mo	Pt
Spectrum A	1.14	0.19	12.79	1.14	53.4	7.48	1.19	15.86
Spectrum B	0	0	14.95	1.16	69.67	10.43	0	0
Spectrum C	0.97	0.23	11.67	1.06	47.33	7.08	0	24.83
Spectrum D	0.64	0.22	14.84	1.17	62.85	9.45	2.3	4.21
Average	0.69	0.16	13.56	1.13	58.31	8.61	0.87	11.22
Standard Deviation	0.5	0.11	1.61	0.05	9.9	1.59	1.11	11.28
Spectrum E	1.17	0	13.81	0.76	68.75	10.07	2.32	0
Sprectrum F	0.49	0.23	16.2	1.27	66.1	9.8	1.4	1.23
Spectrum G	0.61	0.27	16.29	1.01	66.48	9.86	1.62	0
Average	0.76	0.17	15.43	1.02	67.11	9.91	1.78	0.41
Standard Deviation	0.36	0.14	1.4	0.26	1.44	0.14	0.48	1.23

Figure 90: SEM micrograph of non-soluble products on sample tested at -1050 mV and an applied AC density of 500 A/m². The regions studied in the EDS analysis are marked with letters.

Table C.3.4.2: EDS study of non-soluble products identified on sample tested at -1050 mV and an applied AC density of 500 A/m². The chemical composition of the surface free of products has also been analyzed.

	O	Si	Cr	Mn	Fe	Ni	Mo	Pt
Spectrum A	1.93	0	2.29	0	10.33	0.94	0	84.52
Spectrum B	1.17	0	0.83	0	5.9	0	0	90.95
Spectrum C	0.95	0	0.85	0	5.44	0	0	92.77
Spectrum D	1	0	0.7	0	5.29	0	0	92.09
Spectrum E	0.93	0	0.71	0	5.31	0	0	92.07
Average	1.2	0	1.07	0	6.45	0.19	0	90.48
Standard Deviation	0.42	0	0.68	0	2.18	0.42	0	3.39
Sprectrum F	0.84	0.35	17.18	1.41	67.88	10.35	2	0
Spectrum G	0.92	0.3	17	1.32	67.89	10.39	2.19	0
Spectrum H	0.79	0.32	17.4	1.41	68.16	9.9	2.01	0
Average	0.85	0.32	17.19	1.38	67.98	10.21	2.07	0
Standard Deviation	0.06	0.03	0.2	0.05	0.16	0.27	0.11	0
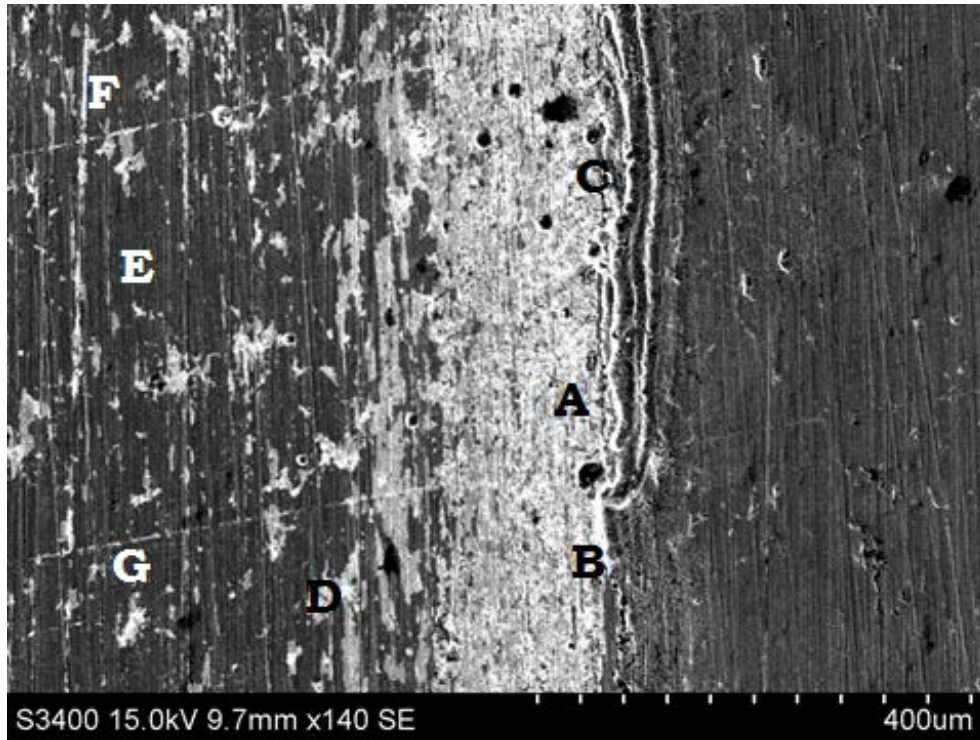
Figure 91: SEM micrograph of non-soluble products on sample tested at -1050 mV and an applied AC density of 1000 A/m². The regions studied in the EDS analysis are marked with letters.

Table C.3.4.3: EDS study of non-soluble products identified on sample tested at -1050 mV and an applied AC density of 1000 A/m². The chemical composition of the surface free of products has also been analyzed.

	O	Si	Cr	Mn	Fe	Ni	Mo	Pt
Spectrum A	1.64	0	5.04	0.58	20.3	2.73	0	69.71
Spectrum B	1.21	0	4.47	0	17.75	2.48	0	74.1
Spectrum C	3.49	0	2.34	0	9.12	1.12	0	83.93
Spectrum D	0.96	0	6.3	0	23.94	3.37	0	65.43
Average	1.83	0	4.54		17.77	2.42	0	73.29
Standard Deviation	1.15	0	1.65		6.31	0.94	0	7.92
Spectrum E	2.52	0.33	15.96	1.07	67.88	10.3	1.94	2.52
Sprectrum F	2.62	0.34	16.34	1.31	67.39	9.82	2.17	2.62
Sprectrum G	2.48	0.33	16.23	1.05	67.55	10.34	2.02	2.48
Average	2.54	0.33	16.18	1.15	67.61	10.15	2.04	2.54
Standard Deviation	0.08	0.01	0.2	0.14	0.25	0.29	0.12	0.08

Appendix D X65 CS

D.1 Weight loss

To correct for additional weight losses related to the removal of corrosion products, un-corroded samples were tested as described in ASTM G1-03[70].

Figure 92 shows graphically the additional loss from a repetitive number of cycles for carbon steel and the value of weight that had to be subtracted from the recorded weight loss values. One cycle was set to last for 30 seconds and it was found experimentally that a maximum number of three cycles were required for removal of corrosion products at all used AC densities.
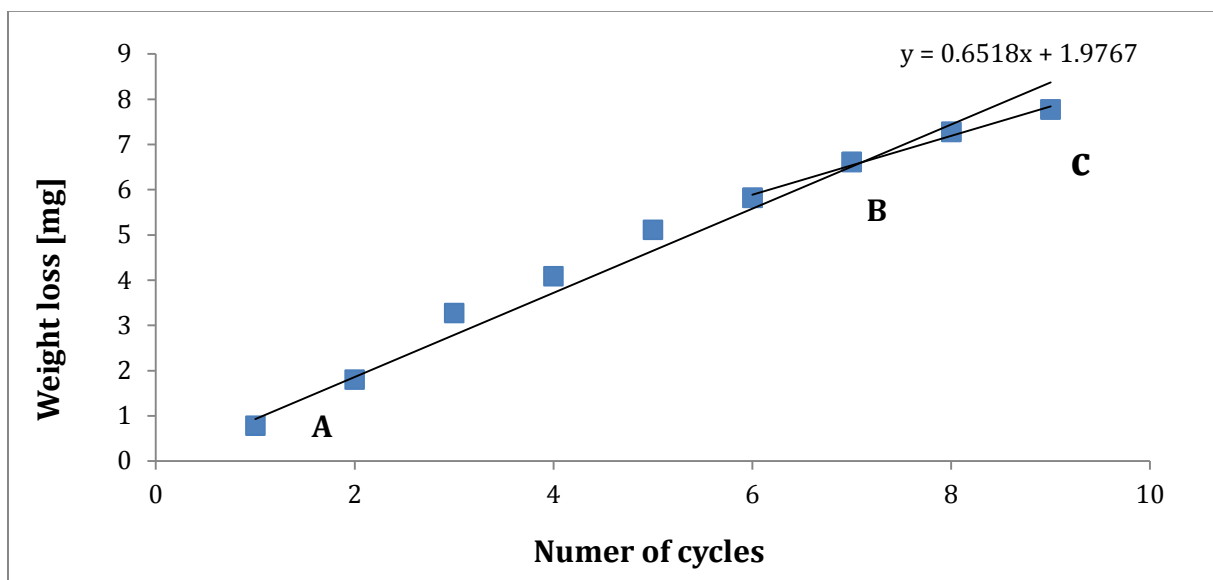
Figure 92: Mass loss of X65 samples resulting from repetitive cleaning cycles. One cycle corresponds to 30 seconds of immersion. Removal of corrosion products happens along line AB, while pure removal of metal takes places along BC. For the actual experiments no more than a total of three cycles were needed to remove the present corrosion products.

All reported mass losses are corrected for the additional mass loss encountered due to the chemical cleaning procedure.

Table D.1.1 shows the results from weight loss measurements for samples tested at -800 mV while Table D.1.2 shows results for similar tests at -1050 mV.

Table D.1.1: Results from weight loss measurements at -800 mV when samples have been tested for 48 hours for increasing AC densities.

i_{AC} [A/m^2]	Δm_{corr} [mg]	$\triangle \overline{m}_{corr}$ [mg]	i_{corr}^{WL} [A/cm^2]	$\overline{i}_{corr}^{WL}$ [A/cm^2]	CR^{WL} [mmy]	$\overline{CR}^{WL}$ [mmy]
0	0.88	0.72	2.69E-06		0.031	0.025
0	0.56		1.70E-06	2.20E-06	0.020	
100	4.24	3.26	1.29E-05		0.150	0.115
100	2.28		6.93E-06	9.93E-06	0.081	
500	6.11	5.79	1.86E-05		0.216	0.205
500	5.47		1.67E-05	1.76E-05	0.194	
700	2.28	2.23	1.76E-05		0.204	0.199
700	2.17		1.67E-05	1.71E-05	0.194	

Table D.1.2: Results from weight loss measurements at -1050 mV when samples have been tested for 48 hours for increasing AC densities.

i_{AC} [A/m^2]	Δm_{corr} [mg]	$\triangle \overline{m}_{corr}$ [mg]	i_{corr}^{WL} [A/cm^2]	$\overline{i}_{corr}^{WL}$ [A/cm^2]	CR^{WL} [mmy]	$\overline{CR}^{WL}$ [mmy]
0	0.33	1.27	1.02E-06		0.012	0.045
0	2.21		6.73E-06	3.87E-06	0.078	
100	1.44	1.91	4.39E-06		0.051	0.068
100	2.38		7.24E-06	5.82E-06	0.084	
500	6.73	6.65	2.05E-05		0.239	0.236
500	6.57		2.00E-05	2.03E-05	0.233	
700	0.03	0.78	2.56E-07		0.003	0.070
700	1.89		1.45E-05		0.169	
700	0.43		3.33E-06	6.03E-06	0.039	

Figure 93 shows the calculated corrosion current densities for all parallels.
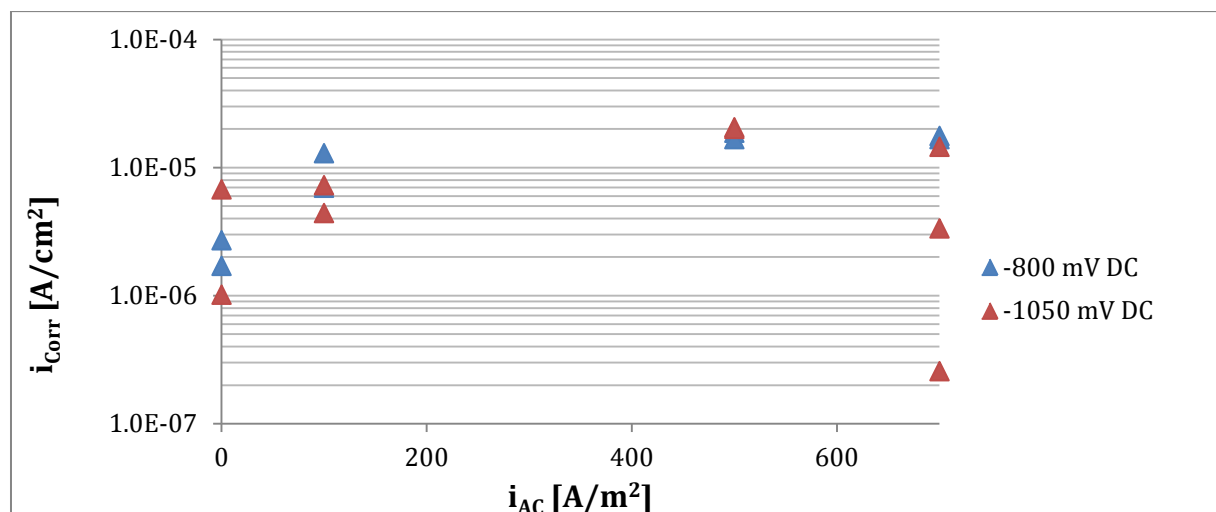
Figure 93: Corrosion rates for all parallels of X65 as calculated from weight losses when increasing AC densities are applied.

D.2 Polarization behavior

Polarization curves recorded during the autumn project [48] were not found to be satisfactory. New cathodic curves were therefore recorded at 500 A/m^2 and 700 A/m^2 AC, see Figure 94.
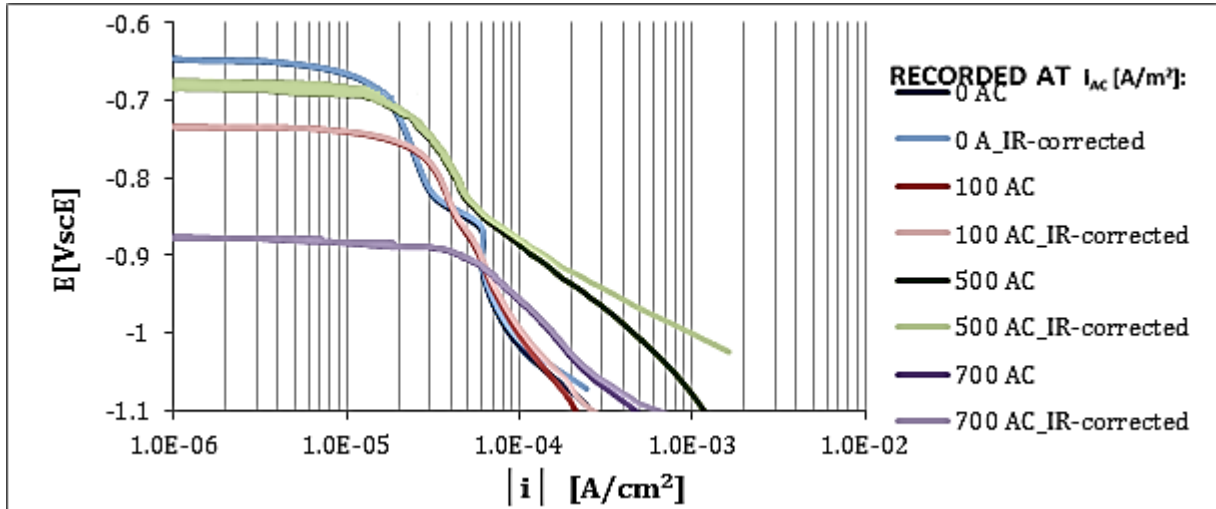
Figure 94: Polarization curves recorded for AC densities from 0 to 700 A/m^2 on stagnant electrodes of X65 type of steel immersed in 3.5 wt % NaCl for 47 hours. Sweep rate was 0.167 mV/sec.

The curves, when plotted, were corrected for the potential drop due to resistance in the electrolyte, R_s . Information about the resistances determined by the method explained in Appendix A, are to be found in Table D.2.

Table D.2: Data about the electrolyte resistance, Rs ,determined graphically and used to correct curves for IR-drop.

i_{AC} [A/m^2]	R_S [Ω]
0	13[*]
100	20[*]
500	12[*]
700	10[*]

* *Correction for cathodic curves*

Figure 95 shows calculated values for $|i_{red}|$ based on obtained values for i_{NET} during the cathodic polarization of 316L, for all parallels.
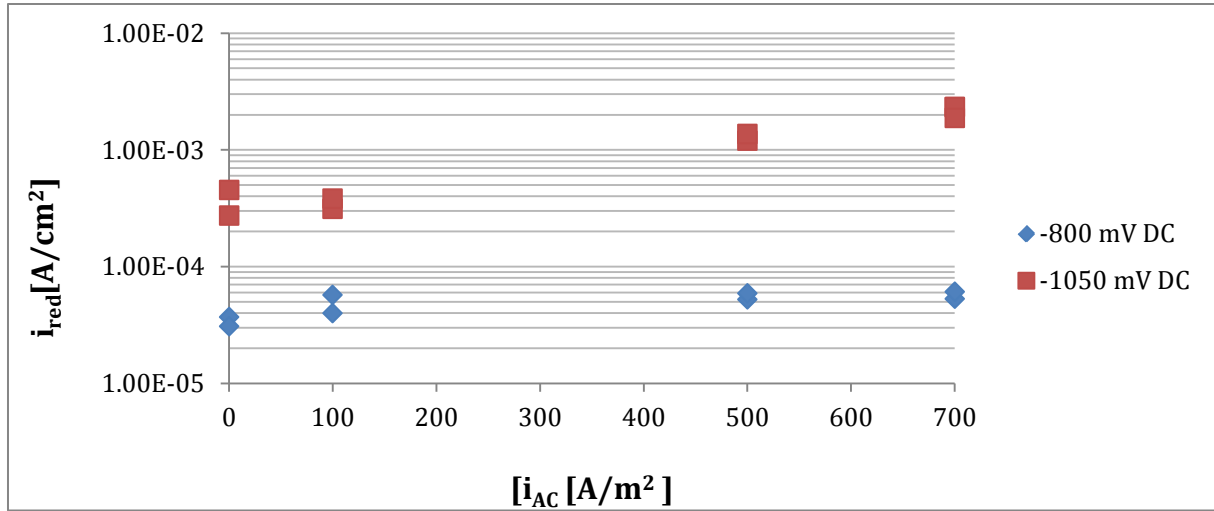
Figure 95: Calculated values for cathodic partial current densities for densities for all parallels of X65 during 48 hours of testing when increasing AC densities are applied under cathodic DC potentials

D.2.1 Results for samples polarized potentiostatically at -800 mV

Table D.2.1 shows averaged current response values for all parallels and averaged values for the experiments at -800 mV. In addition all calculated $|i_{red}|$ values for the parallels and average values for the experiments are given. Figure 96-Figure 99 depict the current response as a function of time for all parallels.

Table D.2.1: Results from potentiostatic polarization at -800 mV when samples have been tested for 48 hours for increasing AC densities.

i_{AC} [A/m²]	i_{NET} $\left[A/cm^2 \right]$	$\bar{i}_{NET}$ $\left[A/cm^2 \right]$	$\mid i_{red} \mid$ $\left[A/cm^2 \right]$	$\mid\bar{i}_{red}\mid$ $\left[A/cm^2 \right]$
0	-3.42E-05		3.69E-05	
0	-2.92E-05	-3.17E-05	3.09E-05	3.39E-05
100	-4.44E-05		5.73E-05	
100	-3.31E-05	-3.87E-05	4.00E-05	4.87E-05
500	-3.46E-05		5.22E-05	
500	-4.25E-05	-3.86E-05	5.92E-05	5.57E-05
700	-3.54E-05		5.30E-05	
700	-4.41E-05	-4.00E-05	6.08E-05	5.69E-05

Figure 96: Recorded current density responses for experiments on X65 under cathodic potentiostatic polarization at -800 mV for samples tested 48 hours at 0 A/m² AC.
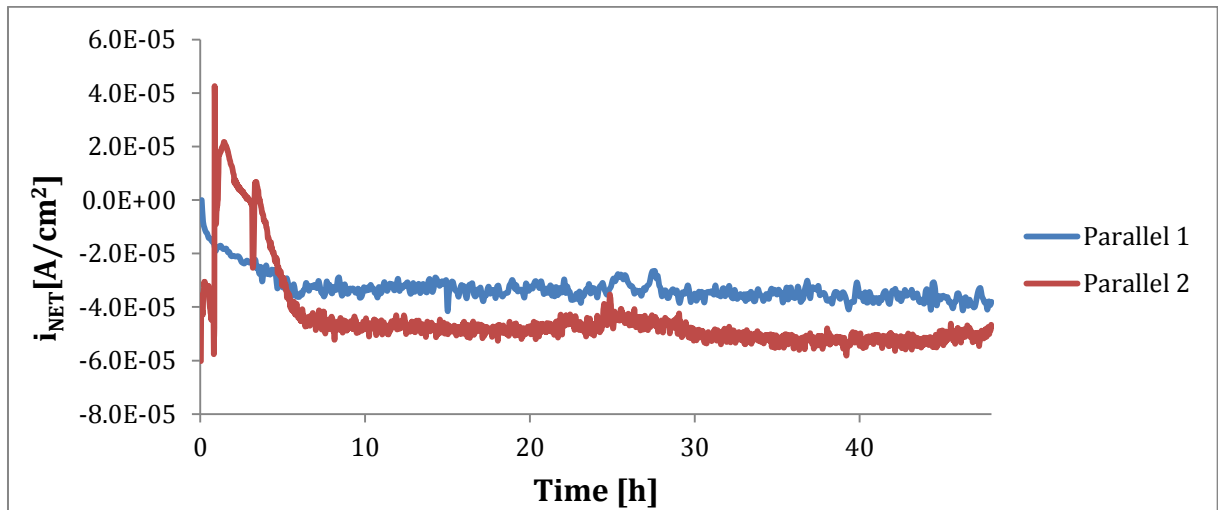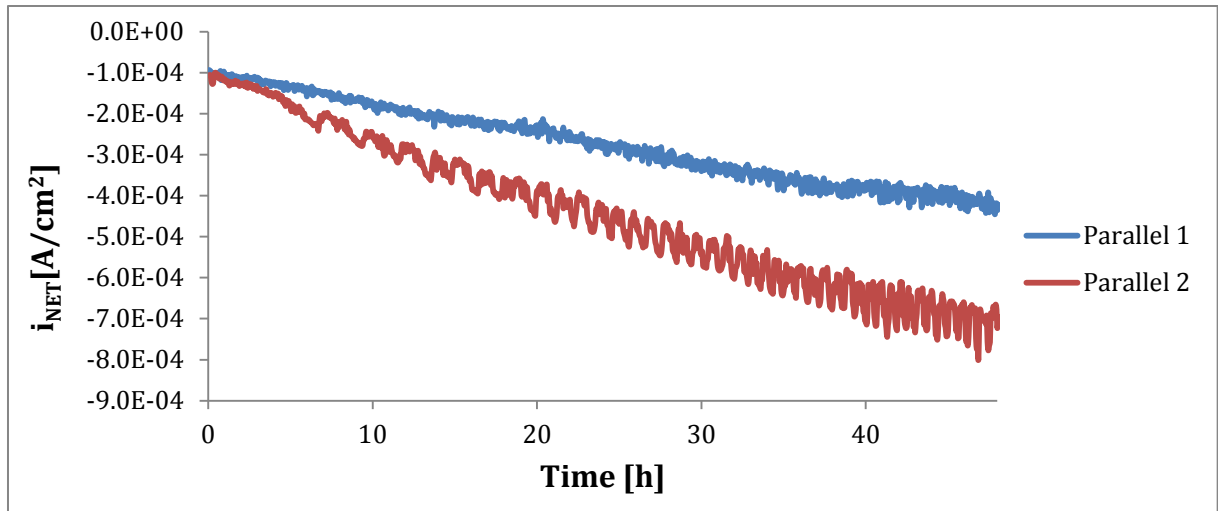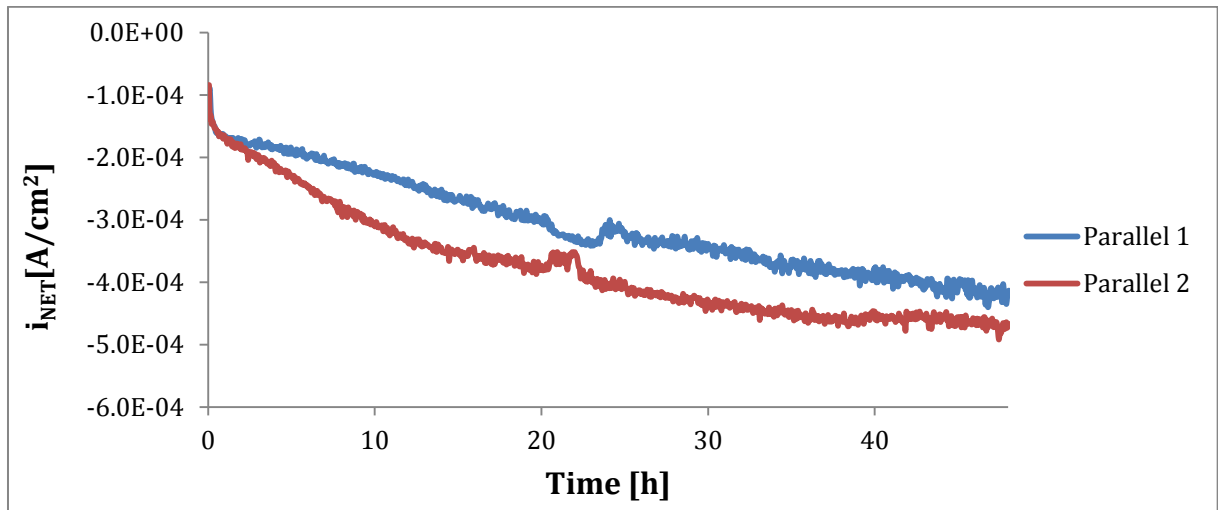

Figure 97: Recorded current density responses for experiments on X65 under cathodic potentiostatic polarization at -800 mV for samples tested 48 hours at 100 A/m² AC.
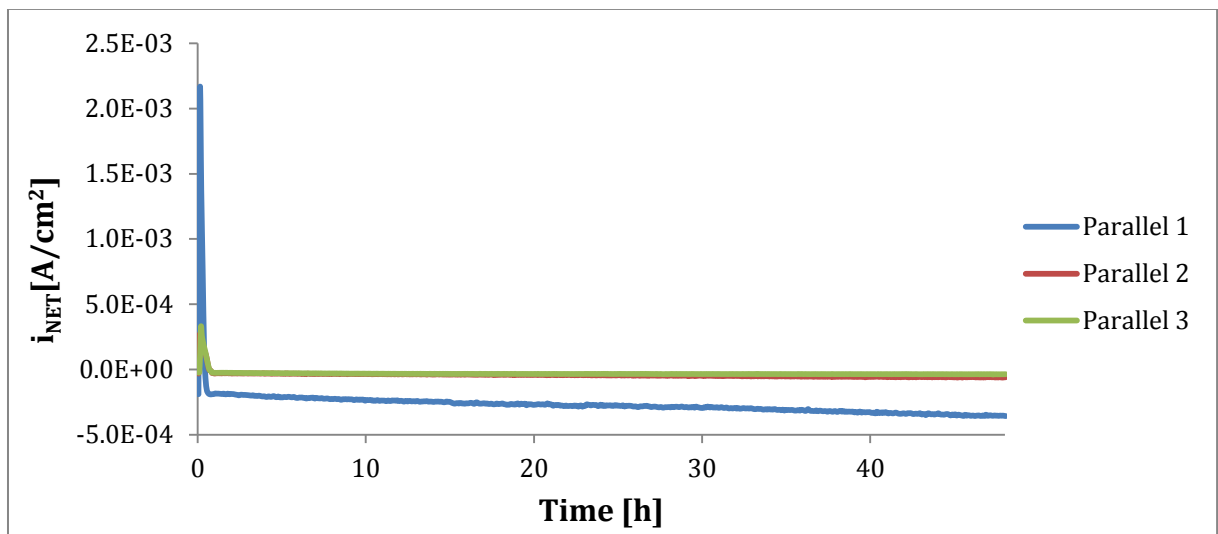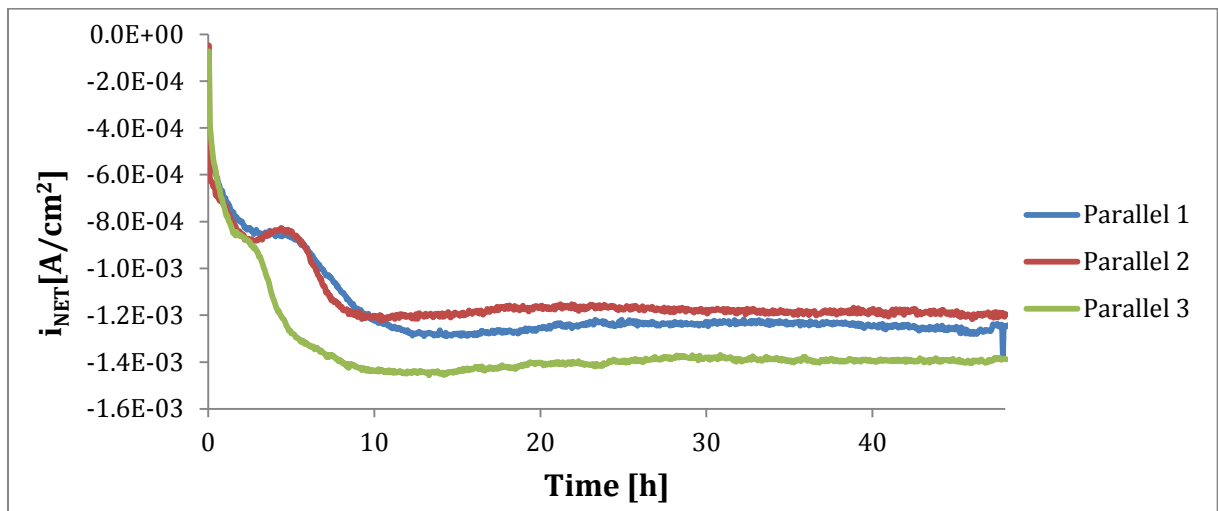

Figure 98: Recorded current density responses for experiments on X65 under cathodic potentiostatic polarization at -800 mV for samples tested 48 hours at 500 A/m² AC.
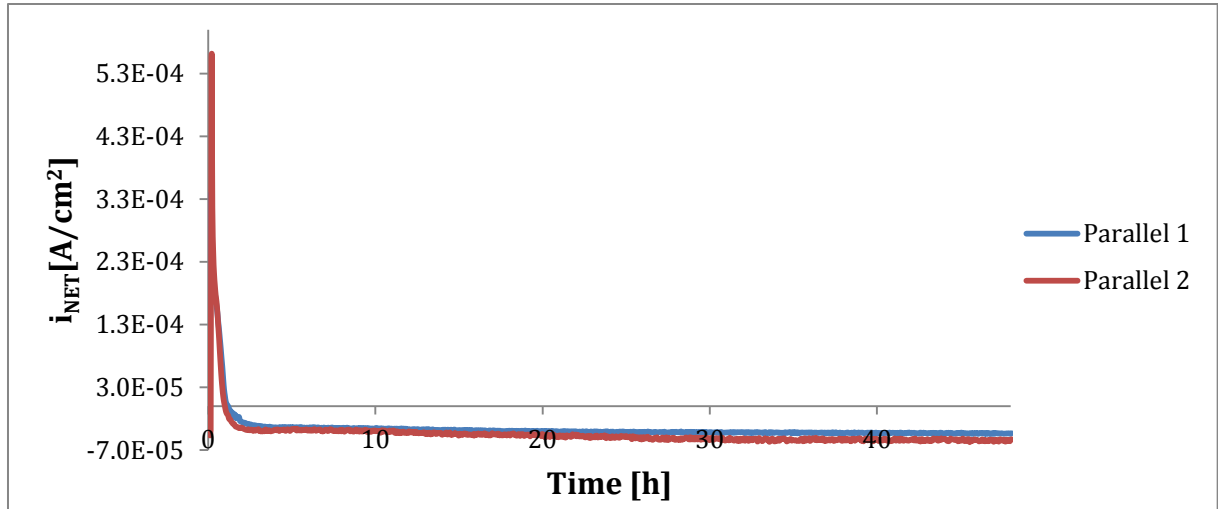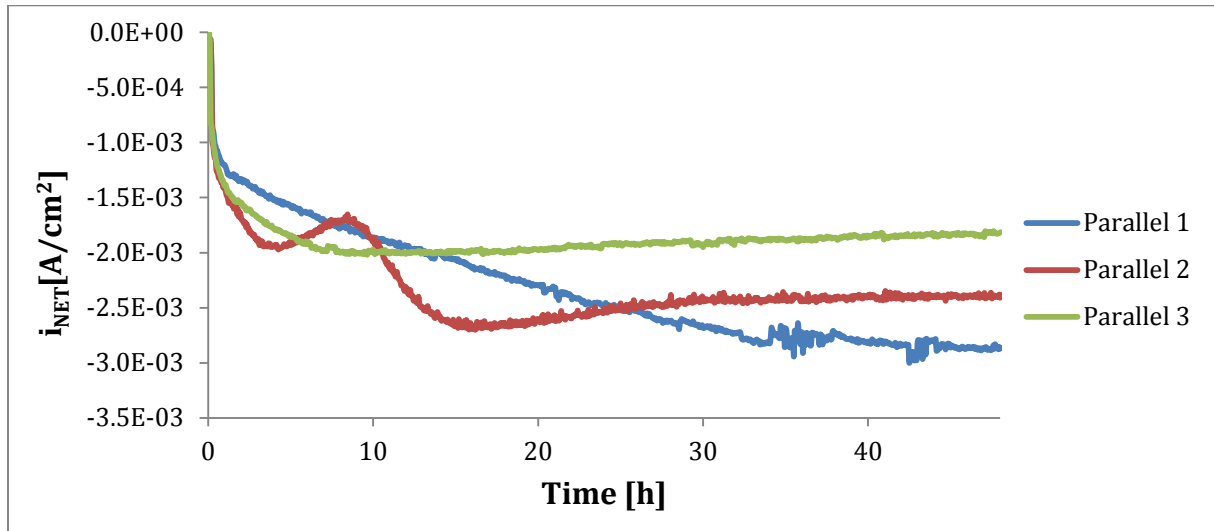
Figure 99: Recorded current density responses for experiments on X65 under cathodic potentiostatic polarization at -800 mV for samples tested 48 hours at 700 A/m² AC.

D.2.2 Results for samples polarized potentiostatically at -1050 mV

Table D.2.2 shows averaged current response values for all parallels and averaged values for the experiments at -1050 mV. In addition all calculated $|i_{red}|$ values for the parallels and average values for the experiments are given. Figure 100-Figure 103 depict the current response as a function of time for all parallels.

Table D.2.2: Results from potentiostatic polarization at -1050 mV when samples have been tested for 48 hours for increasing AC densities.

i_{AC} [A/m²]	$i_{NET} \left[A / cm^2 \right]$	$\bar{i}_{NET} \left[A / cm^2 \right]$	$\mid i_{red} \mid \left[A / cm^2 \right]$	$\mid \bar{i}_{red} \mid \left[A / cm^2 \right]$
0	-2.73E-04		2.74E-04	
0	-4.46E-04	-3.59E-04	4.52E-04	3.63E-04
100	-3.09E-04		3.13E-04	
100	-3.75E-04	-3.42E-04	3.83E-04	3.48E-04
500	-1.18E-03		1.20E-03	
500	-1.35E-03	-1.26E-03	1.37E-03	1.28E-03
700	-2.32E-03		2.32E-03	
700	-2.31E-03	-2.17E-03	2.32E-03	
700	-1.88E-03		1.88E-03	2.18E-03

Figure 100: Recorded current density responses for experiments on X65 under cathodic potentiostatic polarization at -1050 mV for samples tested 48 hours at 0 A/m² AC.

Figure 101: Recorded current density responses for experiments on X65 under cathodic potentiostatic polarization at -1050 mV for samples tested 48 hours at 100 A/m² AC.

Figure 102: Recorded current density responses for experiments on X65 under cathodic potentiostatic polarization at -1050 mV for samples tested 48 hours at 500 A/m² AC.

Figure 103: Recorded current density responses for experiments on X65 under cathodic potentiostatic polarization at -1050 mV for samples tested 48 hours at 700 A/m^2 AC.

D.3 Surface morphology

In the following chapter SEM micrographs recorded at 500X magnification are presented.

D.3.1 SEM analysis for samples polarized potentiostatically at -800 mV
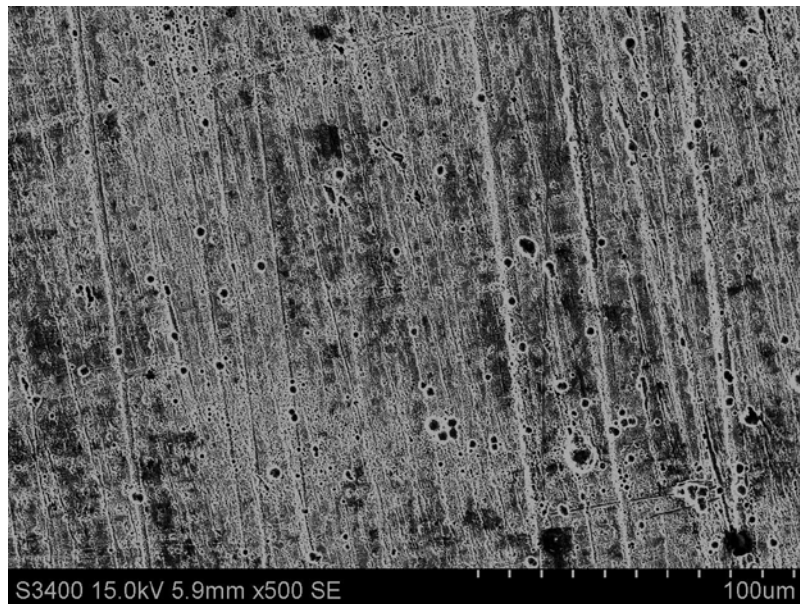
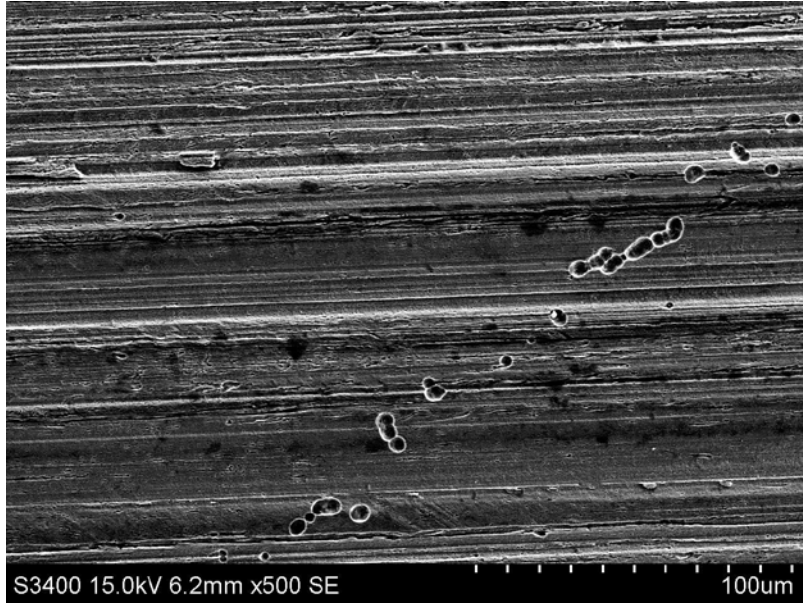**Figure 104: SEM micrograph of surface on X65 sample tested at -800 mV and 0 A/m^{2}AC. Seen at 500X magnification.**
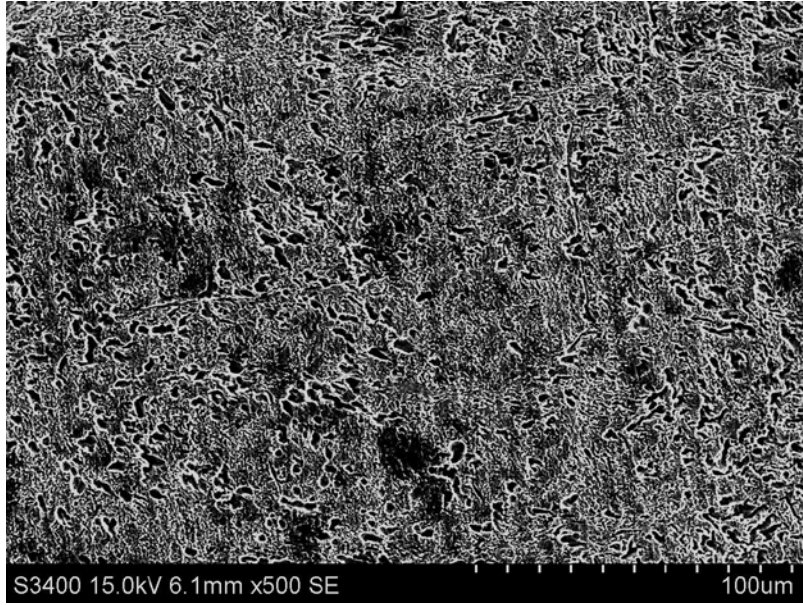
Figure 105: SEM micrograph of surface on X65 sample tested at -800 mV and 100 A/m²AC. Seen at 500X magnification.
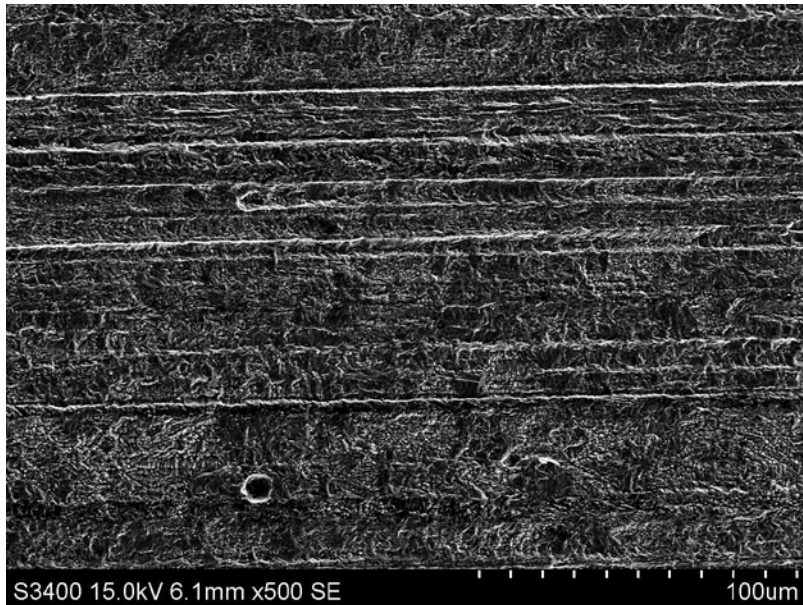
Figure 106: SEM micrograph of surface on X65 sample tested at -800 mV and 500 A/m²AC. Seen at 500X magnification.
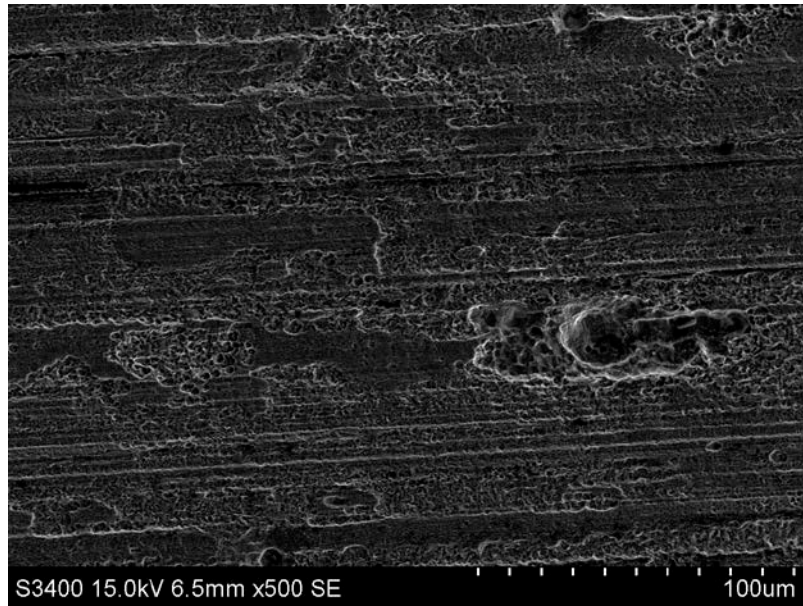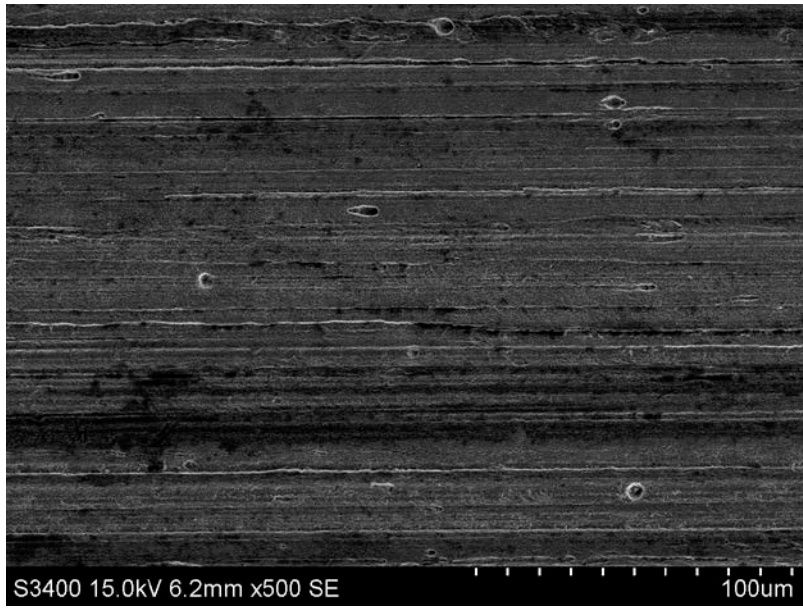
Figure 107: SEM micrograph of surface on X65 sample tested at -800 mV and 700 A/m^{2}AC. Seen at 500X magnification.

D.3.2 SEM analysis for samples polarized potentiostatically at -1050 mV
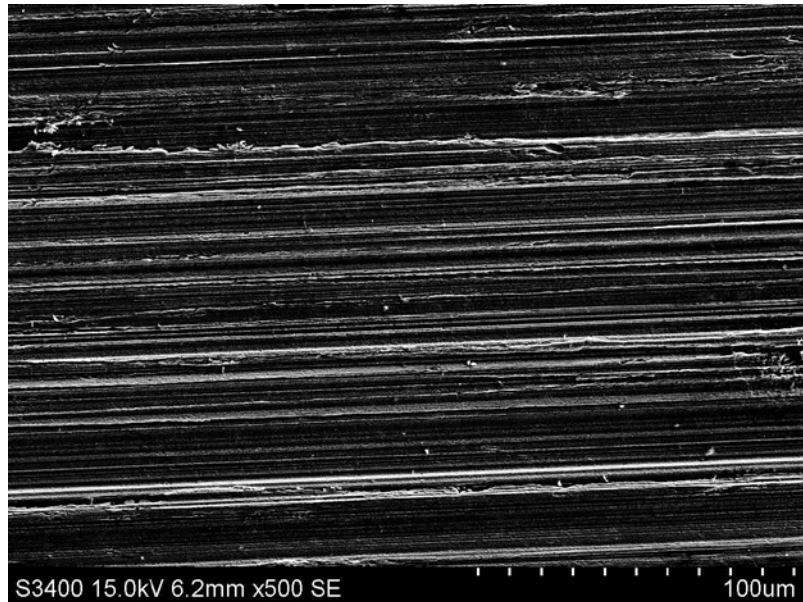
Figure 108: SEM micrograph of surface on X65 sample tested at -1050 mV and 0 A/m^{2}AC. Seen at 500X magnification.

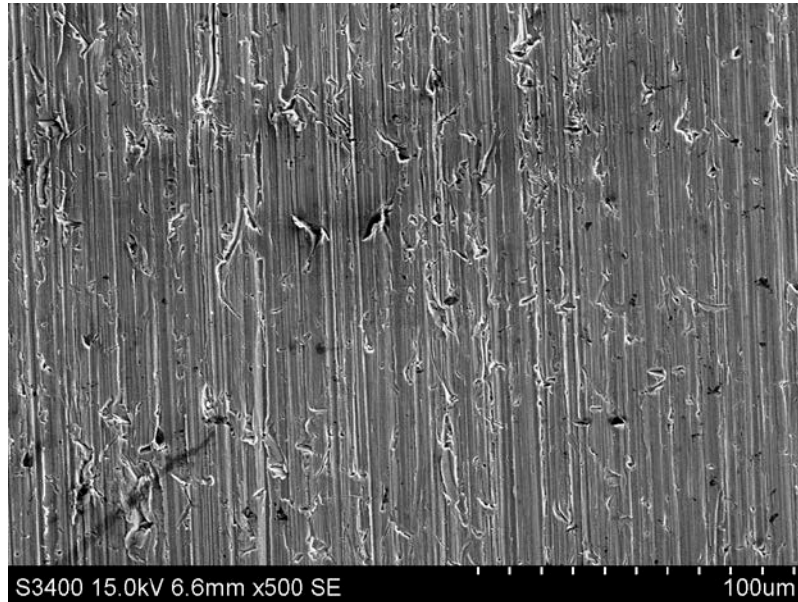**Figure 109: SEM micrograph of surface on X65 sample tested at -1050 mV and 100 A/m^{2}AC. Seen at 500X magnification.**
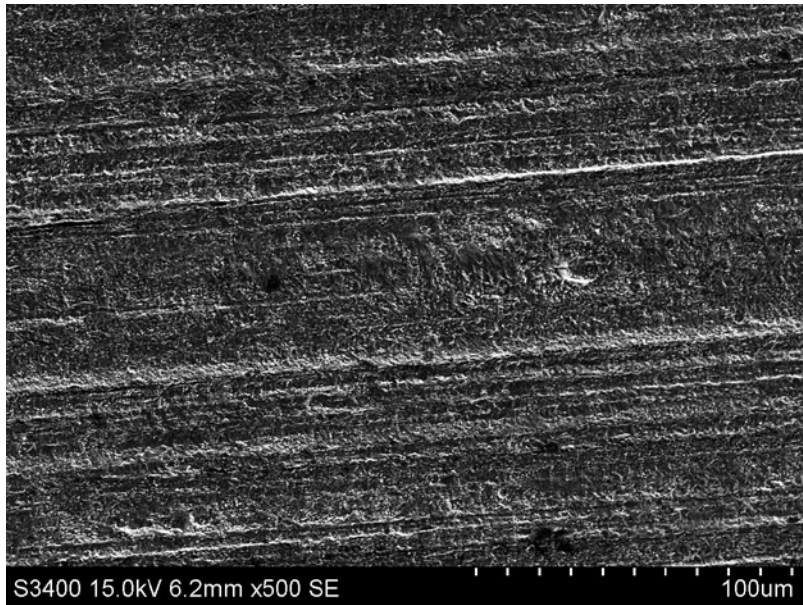
Figure 110: SEM micrograph of surface on X65 sample tested at -1050 mV and 500 A/m^{2}AC. Seen at 500X magnification.

Figure 111: SEM micrograph of surface on X65 sample tested at -1050 mV and 700 A/m²AC. Seen at 500X magnification.

Appendix E 25Cr SSDS

E.1 E_{OC} measurements

The 25Cr samples were let to stabilize during 96 hours (3 days) at the open circuit potential, before the corrosion potential was determined from the last measurement, see Table E.1 for information.

Table E.1: Open circuit potential measurements as a function of time during 72 hours.

i_{AC} [A/m^2]	E_{corr} [V$_{SCE}$]
0	-4.57E-02
100	-4.52E-02
500	-3.48E-01
1000	-2.52E-01

E.2 Polarization behavior

Information about the resistances determined by the method explained in Appendix A.3, are to be found in Table E.2.1. Corrosion parameters as E_{corr} and i_{corr} have also been determined and reported. Table E.2.2 shows averaged current response values and calculated values for cathodic current densities for all parallels.

Table E.2.1: Key results determined graphically from polarization curves.

i_{AC} [A/m^2]	R_S [Ω]	E_{corr}^{Δ} [V$_{SCE}$]	i_{corr}^{Δ} [A/cm^2]	CR [mmy]	$i_{passive}$ [A/cm^2]	$E_{pitting}$ [V$_{SCE}$]
0	14*					>1
	14+	-0.200	2.50E-7	2.91E-03	3.40E-7	
100	16*					0.600
	8+	-0.200	1.30E-6	1.51E-02	3.00E-5	
100_new parallel	10*					0.600
	8+	-0.200	2.00E-5	2.33E-01	2.00E-9	
500	12*					
	12+	-0.600	4.00E-5	4.65E-01	2.00E-9	-
1000						
	15*				1.00E-4	
	14+	-0.200	5.00E-5	5.81E-01		-

* Correction for cathodic curves

+ Correction for anodic curves

Δ Found from cathodic polarization curves.

Table E.2.2: Results from potentiostatic polarization at +100 mV.

i_{AC} [A/m^2]	$i_{NET}\left[\text{A}/\text{cm}^2\right]$	$\left|i_{red}\right|\left[\text{A}/\text{cm}^2\right]$
0	1.02E-08	4.07E-07
100+	-3.07E-07	2.17E-06
100+	-7.83E-07	2.66E-06
100*	-4.39E-06	5.28E-06

[+] V_{AC} applied after 17 hours.

[*] V_{AC} applied from the start.

E.3 Surface morphology

In the following chapter SEM micrographs recorded at 500X magnification are presented.

Figure 112: SEM micrograph of surface on 25Cr sample tested for 72 hours at +100 mV and 0 A/m^2 AC. Seen at 500X magnification.
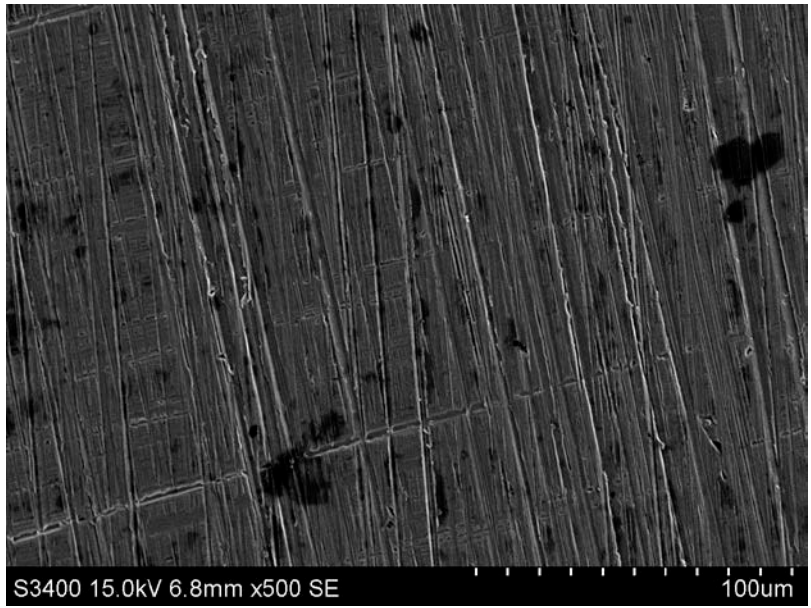
Figure 113: SEM micrograph of surface on 25Cr sample tested for 72 hours at +100 mV and 100 A/m^2 AC (applied after 17 hours of testing) . Seen at 500X magnification.
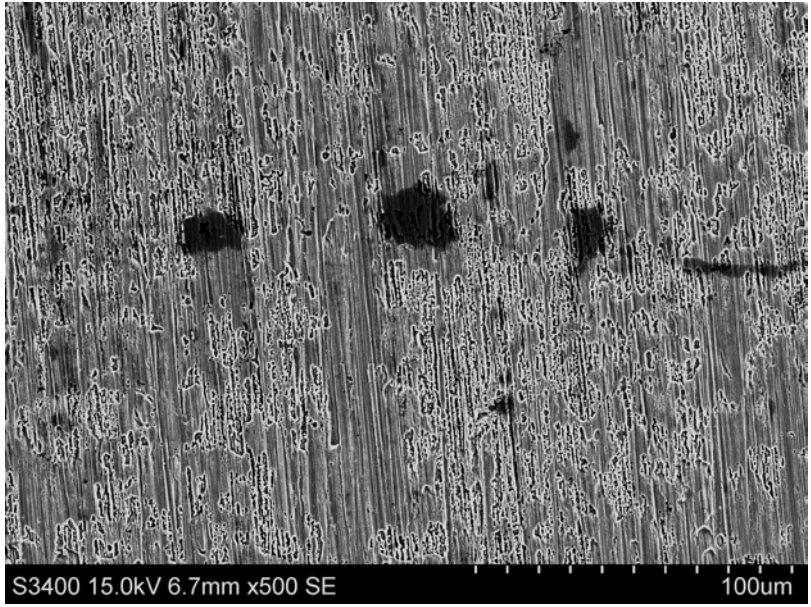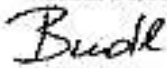

Figure 114: SEM micrograph of surface on 25Cr sample tested for 72 hours at +200 mV and 100 A/m^2 AC (applied after 17 hours of testing) . Seen at 500X magnification.
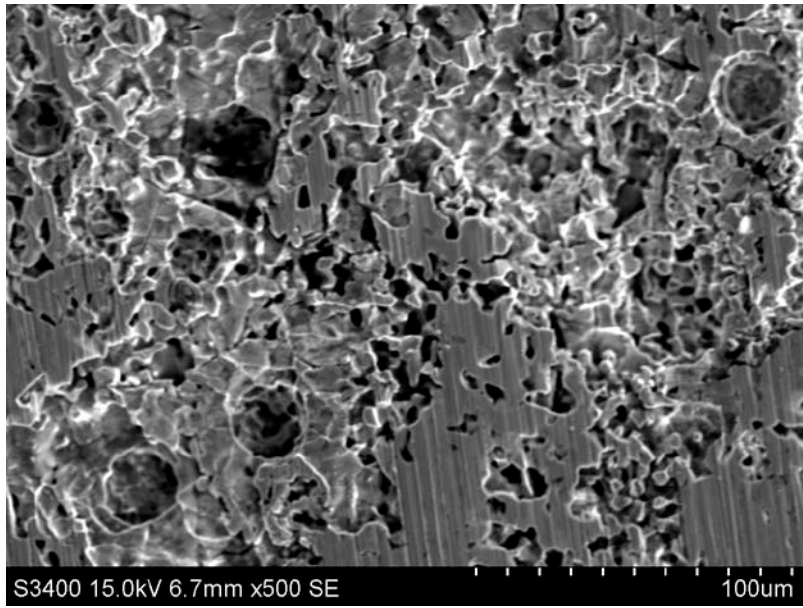
Figure 115: SEM micrograph of surface on 25Cr sample tested for 72 hours at +100 mV and 100 A/m^2 AC (applied from the start) . Seen at 500X magnification.

E.4 Material certificate

ABNAHMEPRÜFZEUGNIS 3.1
INSPECTION CERTIFICATE 3.1

- nach/according to EN 10204 -

BÖHLER BLECHE
www.Bohler-Bleche.com

Attest Nr./Certificate No: 316102-000 dtd: 29.06.2012   Seite/Sheet 1 von/of 1

Besteller / Purchaser	Bestell-Nr. / Purchaser's Order No.
Castle Metals UK Limited	1963 vom 20120118
Unit 10/11	
Walker Industrial Park	
Guide	
BLACKBURN, LANCASHIRE BB51 2QE	
GROSSBRITANNIEN	

Auftrags-Nr. / Works Order No.	Lieferschein / Dispatch note
50745? dtd. 19.01.2012	80147103 von 28.06.2012

Erzeugnis / Product
Sheets
"BÖHLER Antink A 913", UNS S32750 to ASTM A240/ASME SA240-2011a,
Norsok MDS D55 Rev. 4, NACE MR 0175-2003, ISO 15156-3 2003, PED 97/23/EC
in similar to Shell ES247 Rev. 1, 1998 and DEP 30.10.02.35 EPE, incl. X500 Micrograph,
Finish No. 1 to ASTM A480M-2009, hot rolled, solution annealed, pickled

Lieferung / Delivery

Pos Item	Umfang der Lieferung Description Pos	Stück Pcs	Gewicht kg Weight kg	Schmelze Heat No.	Prüf-Nr Test No.
10	3000 x 1500 x 1.50 mm sheet no. 1-11	11	605	U72963	291250
10	3000 x 1500 x 1.50 mm sheet no. 12-16	5	282	U72963	280251

Chemische Zusammensetzung / Chemical Composition (%)

Schmelze (vom Vormateriallieferanten / from pre-material supplier)

Heat No.	C	SI	MN	P	S	CR	MO	NI	CU	N	PREN
U72963	0.017	0.29	0.58	0.021	0.0004	25.75	3.77	6.88	0.17	0.2730	42.64

Erschmelzungsart / Steelmaking Process: EAF + AOD

Mechanische Eigenschaften / Mechanical Properties

ZVF: ASTM E 8/E 8M-09

Prüf-Nr	RP0,2 N/mm2	RM N/mm2	A50 %	Temp. °C	Probenform Sample
Min	550	795	15.0		
Max		930			
280251/1	544	910	25.1	RT	FZ8
291250/1	614	895	27.0	RT	FZ8

Verified True Copy
Castle Metals UK certify that this is a true copy of
the original test certificate.

Signed: _____   Date: _____

BÖHLER BLECHE GMBH & Co KG
Böhler-Gasse 1, 8680 Mürzzuschlag

Monika Budl
(AUSSTELLER)
(ORIGINATOR)

Budl
(ABNAHMEBEAUFTRAGTE)
(INSPECTION REPRESENTATIVE)

Certified Copy of Original Document
Special Metal Solutions (SMS) Ltd

Signed.................

Dated.................

ABNAHMEPRÜFZEUGNIS 3.1
INSPECTION CERTIFICATE 3.1
- nach/according to EN 10204 -

Attest Nr./Certificate No: 316182 - 009 dtd. 29.08.2012

BÖHLER
BLECHE
www.Bohler-Bleche.com

Seite/Sheet: 2 von/of 3

ZVF: DIN EN ISO 6892-1-2009

Prüf-Nr	RP0,2	RM	A80	Temp.	Probenform
	N/mm2	N/mm2	%	°C	Sample
Min	530	730	20,0		
Max		930			
286251/1	629	902	23,5	RT	FZ2
291250/1	651	882	27,2	RT	FZ2

HRC: ASTM E 18-08b

Prüf-Nr	HRC	Temp.
	Rockwell	°C
Max	32,0	
286251/1	23,4	RT
291250/1	22,2	RT

PCT:(*)
Pitting corrosion test ASTM G48 Methode A; 50°C /24 h acc. to Norsok MDS D55 Rev.4:
no pitting visible / no weight loss detectable

Ferrite content acc. to ASTM E 562-11:
Lot no. 291250: 54,8 %
Lot no. 286251: 54,9 %

Microstructure at magnification 500x: Free from harmful intermetallic phases and precipitates: see enclosure

Not included in the scope of ISO 17025 accreditation:

Positive material identification: satisfactory

Ultra-sonic edge-zone-test was made: satisfactory

Heat treatment: solution annealed at 1090°C / 13,5 min / water

Material is capable to fulfil DIN 1.4410 to EN 10088-2/09.2005 and EN 10028-7/2008.

Prüfzeitraum zerstörende Prüfungen / Test period destructive testing:

Prüf-Nr	
286251	11.05.2012 - 18.05.2012
291250	11.05.2012 - 15.06.2012

(*)   Erprobung im Unterauftrag in einem akkreditierten Labor.
         Subcontracted testing in an accredited laboratory.

BÖHLER BLECHE GMBH & Co KG
Böhler-Gasse 1, 8680 Mürzzuschlag

Monika Budl

(AUSSTELLER)
(ORIGINATOR)

Budl

(ABNAHMEBEAUFTRAGTE)
(INSPECTION REPRESENTATIVE)

XXXVII